

**Real-time monitoring of neuronal cells through electrohydrodynamic patterning of flexible graphene microelectrodes**

by

**Amir Ehsan Niaraki Asli**

A dissertation submitted to the graduate faculty  
in partial fulfillment of the requirements for the degree of

**DOCTOR OF PHILOSOPHY**

Major: Mechanical Engineering

Program of Study Committee:

Nicole N. Hashemi, Major Professor

Reza Montazami

Travis Sippel

Xinwei Wang

Long Que

The student author, whose presentation of the scholarship herein was approved by the program of study committee, is solely responsible for the content of this dissertation. The Graduate College will ensure this dissertation is globally accessible and will not permit alterations after a degree is conferred.

Iowa State University

Ames, Iowa

2021

Copyright © Amir Ehsan Niaraki Asli, 2021. All rights reserved.

**DEDICATION**

This dissertation is dedicated to my beloved parents,

Mahshid Ansarnia and Ata Niaraki

for their relentless support and love.

## TABLE OF CONTENTS

	Page
LIST OF FIGURES .....	v
LIST OF TABLES .....	xi
NOMENCLATURE .....	xii
ACKNOWLEDGMENTS .....	xiii
ABSTRACT .....	xiv
CHAPTER 1. INTRODUCTION: LIQUID-PHASE EXFOLIATION OF GRAPHENE, ELECTROHYDRODYNAMIC PRINTING AND NEURONAL INTERFACING .....	1
CHAPTER 2. HIGH-YIELD PRODUCTION OF AQUEOUS GRAPHENE FOR ELECTROHYDRODYNAMIC DROP-ON-DEMAND PRINTING OF BIOCOMPATIBLE CONDUCTIVE PATTERNS .....	8
Abstract .....	8
2.1 Introduction .....	8
2.2 Materials and Methods .....	12
2.3 Results and Discussion .....	15
2.3.1 Graphene Characterization .....	15
2.3.2 Scale-up Study .....	18
2.3.3 Ink Formulation and Printing .....	19
2.3.4 Post Processing and Electrical Conductivity .....	20
2.4 Conclusion .....	23
References .....	24
CHAPTER 3. VIABILITY OF NEURAL CELLS ON 3D PRINTED GRAPHENE BIOELECTRONICS .....	30
Abstract .....	30
3.1 Introduction .....	30
3.2 Materials and Experimental Section .....	32
3.2.1 Preparation of Graphene .....	33
3.2.2 Substrate Preparation .....	35
3.2.3 Inkjet Printing Procedure .....	36
3.2.4 Post-Processing and Conductivity Testing .....	36
3.2.5 Raman Spectroscopy .....	37
3.2.6 Scanning Electron Microscopy and Atomic Force Microscopy .....	38
3.2.7 Chip Biocompatibility Tests .....	38
3.2.8 Live–Dead Cell Assay .....	39
3.3 Results and Discussion .....	40
3.3.1 Chip Design .....	40
3.3.2 Printing Processes and Microscopy Studies .....	40

3.3.3 Post-Treatment of Graphene Prints .....	42
3.3.4 Biocompatibility Testing with N27 Cells.....	43
3.4 Conclusions .....	45
References .....	45
CHAPTER 4. ELECTROJET PRINTED GRAPHENE MICROELECTRODES FOR REAL-TIME IMPEDANCE SPECTROSCOPY OF DOPAMINERGIC NEURONAL CELLS .....	52
Abstract.....	52
4.1 Introduction .....	53
4.2 Materials and Methods .....	55
4.2.1 Graphene Synthesis .....	55
4.2.2 Device Fabrication .....	56
4.2.3 Electrochemical Characterization.....	58
4.2.4 Cell Culture and Biocompatibility Analysis. ....	58
4.3 Results and Discussion .....	60
4.4 Conclusion .....	73
References .....	73
CHAPTER 5. MINUTE-SENSITIVE EXTRA-CELLULAR DETECTION OF NEURONAL CELLS THROUGH FLEXIBLE ELECTROJET PRINTED GRAPHENE .....	78
5.1 Introduction .....	78
5.2 Materials and Methods .....	80
5.3 Results and Discussion .....	81
CHAPTER 6. FUTURE WORK: MACHINE LEARNING-GUIDED INKJET PRINTING OF HIGHLY CONDUCTIVE GRAPHENE PATTERNS.....	87

## LIST OF FIGURES

	Page
<i>Figure 1.1 Schematic representation of graphene production through wet ball milling for fabrication of inkjet-printed patterns. ....</i>	1
<i>Figure 1.2 The lateral size of graphene platelets produced by wet ball milling was calculated to be <math>L &gt; 0.3 \mu\text{m}</math> regardless of batch size. Subsequent to determining defect source in shear exfoliated graphene, Raman spectra can statistically be analyzed to give mean lateral size of graphene platelets (<math>\langle L \rangle</math>). ....</i>	2
<i>Figure 1.3 Oxidation, Vacancy and edge defects in various graphene batch sizes. ....</i>	3
<i>Figure 1.4 TEM imaging of shear exfoliated graphene demonstrates a distribution of graphene flake sizes. While, thinner and laterally larger flakes are more desirable, the graphene sheets tend to stack up after exfoliation; Scale bar: 100 nm. ....</i>	3
<i>Figure 1.5 Surface modification of polyimide film enhances the hydrophilicity of the substrate for inkjet printing process with the change in the contact angle of graphene ink from (a) <math>64^\circ</math> on untreated PI tape to (b) <math>24^\circ</math> on treated PI. ....</i>	4
<i>Figure 1.6 Live–dead cell assays were performed using a <math>70 \mu\text{M}</math> CellTracker™ CMFDA solution combined with an <math>8 \mu\text{M}</math> propidium iodide (PI) solution in FBS-free RPMI medium. N27 cells in vitro after 72h at <math>37^\circ\text{C}</math> in a 5% <math>\text{CO}_2</math> environment deposited on graphene prints. Live cells are shown in green, and dead cells are in red; scale-bars: <math>200 \mu\text{m}</math>. For further details on cell imaging and deposition process refer to reference 45. ....</i>	4
<i>Figure 1.7 Cross-section of graphene lines captured by SEM. Homogeneous normal height of graphene along the line is demonstrated. The majority of the graphene ink is deposited along the centreline, which resulted in dome-like profile. Left image scale bar: <math>100 \mu\text{m}</math>; Right image scale bar: <math>20 \mu\text{m}</math>. ....</i>	5
<i>Figure 1.8 The electrojet printed graphene microelectrodes under flexure with radius of curvature of <math>6.3 \text{ mm}</math>. ....</i>	5
<i>Figure 1.9 The annotated components for real-time optical and electrical monitoring of neuronal cells. ....</i>	6

- Figure 1.10 Electrode characterization test in standard ionic solution. (left) Cyclic voltammetry of inkjet-printed graphene electrodes in 1 M KCL solution. The data for 5 repeattative cycles are reported with scan rate of 100 mV/s. (Right) Electrical impedance spectroscopy of the electrodes reported in Ohms and scanned between 0.1 Hz and 10 kHz in PBS solution. .... 6*
- Figure 2.1 Shear exfoliation of graphene from Graphite in water. A) Schematics of shear exfoliation of graphite using steel balls with presence of BSA proteins B) Printed graphene ink on flexible substrate C) Graphite powder in water before exfoliation D) Graphene ink with concentration of 5.1 mg/ml – 1 after remaining still for one month. E) Stability of graphene patterns after 7 days of submergence in water. .... 11*
- Figure 2.2 Characterization of shear exfoliated graphene from graphite particles in water. A) Single graphene flake, which is semi-transparent; scale bar: 50 nm. B) TEM image of single FLG which is folded due to its large aspect ratio; scale bar: 100 nm. C) Multiple graphene flakes with crumbled and folded morphology; scale bar: 100 nm. D) TEM imaging demonstrates a distribution of flake sizes that tend to stack up; Scale bar: 200 nm. E) Raman spectra of Graphene sample in 5 different laser spots. F) AFM image and corresponding height profile of graphene. G) SEM Image of Single Graphite particle; scale bar: 10  $\mu$ m ..... 16*
- Figure 2.3 Graphene concentration measured given by UV absorption. A) Absorption coefficient obtained from UV-vis spectroscopy at  $\lambda=660$  nm. B) Change of graphene concentration with respect to batch sizes varying from 20 ml to 1000 ml. The resultant concentration of wet ball milled graphene remain constant (5.1 mg/ml – 1) for batches larger than 400 ml. .... 18*
- Figure 2.4 A) Drop-on-demand printer setup for inkjet printing of graphene B) SEM for cross-sectional view of printed patterns with magnifications which show a normal height of  $\approx 4$   $\mu$ m C) Height contour of full printed graphene and sample line through which average height is reported. D) The 20x magnified section of the sample print. E) In distance 0 and 1200 on the sample line (c), the height is measured over the substrate. the maximum measured height is the peak of the printed material. The difference between these two indicates the height of the print ( $\approx 4$   $\mu$ m) at maximum which is compatible with SEM imaging. F) SEM for top view of printed graphene after annealing at 280°C for 30 minutes; scale bar: 20  $\mu$ m. .... 20*

- Figure 2.5 A) Change of sheet resistance  $RS$  of printed graphene with respect to annealing time in  $280^{\circ}\text{C}$  oven. B) Change of sheet resistance of printed graphene with respect to changes in annealing temperature. C) Linear I-V response of the lines with length of 100 mm measured by a potentiostat. D) Comparison of the yield and resultant sheet resistance of produced graphene with other published approaches. In the studies that sheet resistance was not reported directly, their values were estimated by equation 7 using the reported resistivity/conductivity values. .... 23
- Figure 3.1 Schematic of the drop-on-demand graphene printing method. (A) An abridged general view of the printer setup. (B) A graphene solution was mixed using a Vibro-Energy mill (shaker mill) for 90 h at 300 rpm. (C) Schematic of chip setup. (D) Equipment setup during printing. A syringe pump was used along with an inkjet printer to deposit ink at a rate of  $7\ \mu\text{L/s}$  to ensure a constant flow rate throughout the syringe. (E) Needle and substrate setup. A 3 kV potential difference was introduced between the substrate and needle for the purpose of affixing ink onto the substrate. A cover glass was placed on a regular microscope slide for stability and support. (F). Printed chip end result of 3D printed graphene. .... 34
- Figure 3.2 Graphene wet-ball milling container setup. (A) Twenty steel balls with a diameter of 8.7 mm (11/32") and 10 steel balls with a diameter of 4.5 mm (3/16") were added. (B,C) Container assembly for shaker mill. .... 35
- Figure 3.3 Conductivity measurements of printed graphene prints after treatment. (A) Conductivity changes dependent on the temperature, checked every 30 min. (B) Conductivity changes dependent on time at the same temperature of  $280^{\circ}\text{C}$ . .... 37
- Figure 3.4 Raman spectra plot of both ball milling and blundered graphene under 532 nm laser. (A) Raman results for both ball milling and blender graphene samples on a Si/SiO<sub>2</sub> substrate. (B) Raman results for after annealed prints and non-annealed prints on Kapton tape. .... 38
- Figure 3.5 Microscope image of printing results. (A) An area of prints under the microscope. The red, blue, and green arrows indicate graphene, copper tape, and polyimide (PI), respectively, after the annealing process. (B,C) SEM images of printed graphene on PI using 2–5 kV accelerated voltage. (B) is a top-view image taken using SEM after annealing the prints with an average width of  $\approx 868\ \mu\text{m}$ . (C) shows an image of a cross section with an average depth of  $5.20\ \mu\text{m}$ . .... 41
- Figure 3.6 Atomic force microscopy (AFM) of graphene. (A) Graphene flake, (B) Spectral RMS amplitude was 5.33 nm. (C) AFM tapping frequency. .... 42

- Figure 3.7 Cells cultured on graphene chips after 72 h of incubation. (A) Control well of N27 cells after 72 h at 37 °C in a 5% CO<sub>2</sub> atmosphere. (B–D) After 72 h of incubation, the cells expanded across a gap with a length of 290 μm. .... 44*
- Figure 3.8 Percentage of live cells indicating that cell viability was approximately 85%. .... 44*
- Figure 4.1 Fabrication of graphene biosensors for real time monitoring of neuronal cells. (a) Transferring to glass coverslip. (b) Addition of silver and copper for connection to the potentiostat. (c) Stabilizing the interconnectors with PI tape. (d) Mounting the cell container (e) Creating the growth channel gap by micro-positioning a glass slide (f) Glass coverslip removal after PDMS hardening. (g) The flexible inkjet-printed Graphene pattern prior to biosensor fabrication. (h) Proliferation of neuronal cells in the growth gap 5 days after interfacing with graphene microelectrodes. .... 56*
- Figure 4.2 Characterization of aqueous graphene ink before and after patterning. (a) Raman spectra of aqueous graphene and treated graphene electrodes acquired at  $\lambda = 532$  nm. (b) TEM imaging of graphene platelets in water. The graphene nanosheets are shown with white arrows and BSA nano particles are shown with blue arrows. Scale bar: 20 nm (c) SEM imaging of annealed graphene electrodes. Scale bar: 50 microns. (d) Reduction in sheet resistance of the shear exfoliated graphene after 30 minutes of annealing in temperatures varying from 50°C to 300°C. (e) The change in the sheet resistance of 10 mm long graphene lines after attachment to glass cover slips with respect to 90° and 180° folding angles (f) The relative change in resistance of 20 mm long graphene lines with respect to various radii of curvature. .... 61*
- Figure 4.3 Cell adaptability on the biosensor. (a) The N27 cells immediately after passage to the growth channel. (b) Cell viability after 5 days in-vitro. (c) Live-dead cell assay after the cell growth in conjunction with the bending of the electrodes with folding angle of 90°. (d) Live-dead cell assay after the removal of the PI substrate with the microchannel from the glass substrate. The electrodes in the growth channel were washed up with media and are turned upside down for 5 minutes. The N27 cells surprisingly remained attached to the graphene lines but left the rest of the substrate area during the wash up. (e) A thorough cell viability test for the biochip, the control and the a bent electrode array with folding angle of 90, reported as mean  $\pm$  standard deviation over one control, four independent chips (n=15). One-way ANOVA  $p < 0.005$ . .... 64*

- Figure 4.4 Equivalent circuit model of N27 cell electrical spectroscopy. (a) Overview. The equivalent circuit in (b) low and (c) high frequency regimes. (d) A sample impedance measurement in low frequency regime that constitutes the resistance of the cell network from seeding (0 DIV) to 3 DIV and after UV exposure scanned with 10 mV/s. The equation for the linear regression fitting line is also shown on the graph with the slope as the resistance value given by the Ohm law and  $R^2$  goodness-of-fit measure for the regression fitting. .... 66*
- Figure 4.5 The resistance of the graphene electrodes, during the cell network maturity ( $> 1500$  cells/mm<sup>2</sup>) and Post UV exposure were normalized with respect to the resistance of the electrodes right after cell passage to give the resistance index. The growth rate of the cell network and their resultant confluence determines the resistance index across the electrodes deposited in the growth channels. The rapid growth of the index decelerates upon the network's maturity. Upon exposure to UV the cell impedance of samples 1-3 respectively drops to 1.44, 1.32 and 1.55 of the initial electrode impedance which represents cell shrinkage and lift-off due to cytotoxicity. The cell density on each electrode determines the value of the index on the particular electrode-cell interface. .... 68*
- Figure 4.6 The optical microscopy images of the N27 cell network (left) along with the normalized cell index the corresponding density at each measurement instance (right). (a) The freshly passaged cells. Sample image of the cell network after (a) 1 DIV (b) 2 DIV (c) 3DIV (4) 4 DIV and (f) after 20 second exposure to UV light; scale bar 100 micron. Upon normalizing the resistance index with respect to the cell density the NRI can enable real-time monitoring of the cell network prior to UV exposure. The graph is presented in terms of mean  $\pm$  standard deviation of NRI across 5 independent chips monitored 1-5 times per day for 4 DIV followed by UV exposure ( $n = 60$ ). Upon the network maturity (by 3DIV), the cell density across all experiment can be given as  $1890 \pm 230$  cells/mm<sup>2</sup>. .... 72*
- Figure 5.1 Schematics and dimensions of the interdigitated electrode setup..... 80*
- Figure 5.2 Schematic of the designed pattern and the transfer method ..... 80*
- Figure 5.3 Microscale characteristics and surface morphology of patterned graphene microelectrodes (A-B) Microscopic images of the electrodes in  $\times 10$  magnification; Scale bar=100  $\mu$ m. (C) SEM imaging of the electrodes with  $\times 400$  magnification; scale bar =50  $\mu$ m. .... 81*

<i>Figure 5.4 Live-dead cell assay of the cell density on the chip. Each row demonstrates the initial seeding concentration of low, medium high (top to bottom) while left column demonstrates the first day in vitro and the right column shows the 3 DIV. Low concentration (66500 cells) are seeded which adhered with the concentration shown in (A) for 1 DIV and proliferated to (B) for 4 DIV. Medium concentration (133000 cells) are seeded which adhered with the concentration shown in (C) for 1 DIV and proliferated to (D) for 4 DIV. High concentration (266000 cells) are seeded which adhered with the concentration shown in (E) for 1 DIV and proliferated to (F) for 4 DIV.....</i>	82
<i>Figure 5.5 Cell density for various seeding cell concentrations in the first 4 days of cell growth.....</i>	83
<i>Figure 5.6 Electrical impedance measurement over the confluent N27 cells from 0.1 Hz to 100 kHz.....</i>	84
<i>Figure 5.7 Magnified EIS measurement of confluent N27 cells under UV exposure in 1 minute intervals. The x axis is given in logarithmic scale for frequencies ranging from 10 Hz to 10 kHz.....</i>	85
<i>Figure 5.8 The change in impedance of a single electrode upon damage exposure in 0.1, 1, 1.5 and 10 kHz frequency resulted by cell shrinkage and lift-off.....</i>	86
<i>Figure 5.9 Minute-sensitive extra-cellular detection of neuronal cells through normalized impedance index.....</i>	86
<i>Figure 6.1 Proliferation of N27 rat dopaminergic neuronal cells in (left) 2 days in vitro compared to (Right) 3 days in vitro.....</i>	87
<i>Figure 6.2 A schematic representation of an ensemble learning model for predicting the quality of inkjet-printed graphene patterns based on experimental parameters. ....</i>	89
<i>Figure 6.3 Performance of Random Forest, Adaboost and Linear regression Models for Conductivity prediction on test dataset (n=11).....</i>	90
<i>Figure 6.4 Feature importance assessment by Random Forest and Adaboost classifiers for conductivity prediction of inkjet-printed graphene patterns.....</i>	90

**LIST OF TABLES**

	Page
Table 4.1. Raman analysis of shear-exfoliated graphene before and after inkjet printing and thermal processing. Results are presented as mean $\pm$ SD, across 5 independently fabricated electrodes and drop casted aqueous graphene for 5 laser spots each (n=30). .....	62
Table 6.1 A sample subset of the created dataset. ....	88

**NOMENCLATURE**

BSA	Bovine serum albumin
DIV	Days in Vitro
PDMS	Polydimethylsiloxane
PSS	Poly 4-styrenesulfonic acid sodium salt
PEI	Poly ethyleneimine

## ACKNOWLEDGMENTS

I would like to thank my major professor, Dr. Nicole Hashemi, and my committee members, Dr. Reza Montazami, Dr. Travis Sippel, Dr. Xinwei Wang, and Dr. Long Que, for their guidance through the duration of this research.

In addition, I would also like to thank my friends, colleagues, the department faculty and staff for making my time at Iowa State University a wonderful experience. Thank you to Marilyn McNamara, Saurabh Aykar, Kelli Williams, Mehran Shirsavar and Mehrnoosh Taghavimehr, Mohammed Al-Hinai, Faisal Al-Masri, Jingshuai Guo, Alex Knapp, Sean Ulrich and Kyle Finck who excelled beyond their duties to help me throughout my research work with their brilliant minds. I also want to offer my appreciation to Wyman Martinek for his help with profilometry, Craig Severson for the assistance with the manufacturing processes and special thanks to Grace Reynolds whose art work served as a beacon of elegance for this academic endeavor.

This work was partially supported by the Office of Naval Research Grant N000141712620, National Science Foundation Award 2014346 and Iowa State University.

**ABSTRACT**

Investigation of the change in the electrochemical properties of neuronal cells upon exposure to stress factors imparts vital information about the stages prior to their death. This study presents a graphene-based biosensor for real-time monitoring of N27 rat dopaminergic cells which characterizes cell adhesion and cytotoxicity factors through impedance spectroscopy. The aim was to monitor the growth of the entire cell network via a non-metallic flexible electrode with a temporal resolution of a minute. Therefore, a water-based graphene solution was formulated as a conductive ink, 3D printed into a flexible substrate through a novel electrohydrodynamic approach, resulting in electrodes with a conductivity of  $6750 \text{ s/m}$ .

A scalable and aqueous phase exfoliation of graphite to high yield and quality of few layer graphene was achieved through (FLG) using Bovine Serum Albumine (BSA) and wet ball milling. The produced graphene ink is tailored for printable and flexible electronics, having shown promising results in terms of electrical conductivity and temporal stability. Shear force generated by steel balls resulted in 2-3 layer defect-free graphene platelets with an average size of hundreds of nm and with concentration of about  $5.1 \text{ mg/ml}$  characterized by Raman spectroscopy, atomic force microscopy (AFM), transmittance electron microscopy (TEM) and UV-vis spectroscopy. Further, a conductive ink was prepared and printed on flexible substrate (Polyimide) with controlled resolution. Scanning electron microscopy (SEM) and Profilometry revealed the effect of thermal annealing on the prints to concede consistent morphological characteristics. The resulted sheet resistance was measured to be  $R_s = 36.75 \text{ } \Omega/\text{sqr}$  for prints as long as 100 mm. Printable inks were produced in volumes ranging from 20 ml to 1 L with potential to facilitate large scale production of graphene for applications in biosensors as well as flexible and printable electronics.

The presented high-throughput method enabled micro-scale monitoring of the entire cell network via the design of a PDMS-based growth channels. The electrical resistance of the cell network was measured continually along with their network density, constituting a mean density of  $1890 \text{ cell/mm}^2$  at full cell confluency. The results demonstrate the applicability of the impedance-based sensing of the cell network for rapid screening of the cytotoxic elements, and the real-time effect of UV exposure on dopaminergic neurons was reported as an immediate application of the device.

Most notably, we are interested in creating a layered microstructure through inkjet printing the water-dispersed graphene to enhance the sensitivity to damage detection in neuronal cells. The microfluidic deposition of graphene electrodes could provide texture cues that are favored by the cells while the patterns are consolidated through the electrostatic field to maintain the stability of the microelectrodes upon flexure. Thus, the detection of detachment can be studied with higher precision through impedance spectroscopy technique, where the cell body is treated as a physical particle which impedes the electrical current passing through the electrode array. Accordingly, inflicting cellular damage leads to alteration in membrane morphology, cellular shrinkage, detachment, and lift-off which will affect the cellular impedance.

## CHAPTER 1. INTRODUCTION: LIQUID-PHASE EXFOLIATION OF GRAPHENE, ELECTROHYDRODYNAMIC PRINTING AND NEURONAL INTERFACING

Graphene is a one-atom-thick, two-dimensional honey-combed arrangement of  $sp^2$  hybridized carbons, which has attracted considerable interest in the scientific community since 2004 due to its unique electrical, mechanical, optical, and thermal properties. There has been extensive research on the bio-interfacing of graphene among other carbon-based materials. Thus, the fabrication of graphene microelectrode arrays is desirable for electrochemical sensing of neuronal cells. The idea that is presented here, involves stabilization of large graphene sheets in water and inkjet printing of the prepared conductive ink on flexible substrates for bio-interfacing (Figure 1.1). Since most of the cellular growth media are water-based, production of high concentration of aqueous graphene is desirable. In order to achieve this, wet ball milling of graphite in water with Bovin serum albumin can be proposed as detailed in chapter 2. This chapter provides a high-level introduction to this process with the technical details left for chapters 2,3 and 4.



*Figure 0.1 Schematic representation of graphene production through wet ball milling for fabrication of inkjet-printed patterns.*

Various methods are reported for mechanical exfoliation of graphene in water via edible proteins. However, scalability of these methods is still a topic that is under investigations. In chapter 2,

details on Raman spectroscopy of ball milled graphene is demonstrated while Figure 1.2 along with equation 1.1 demonstrate the variability in lateral size of graphene platelets with respect to production batch size.

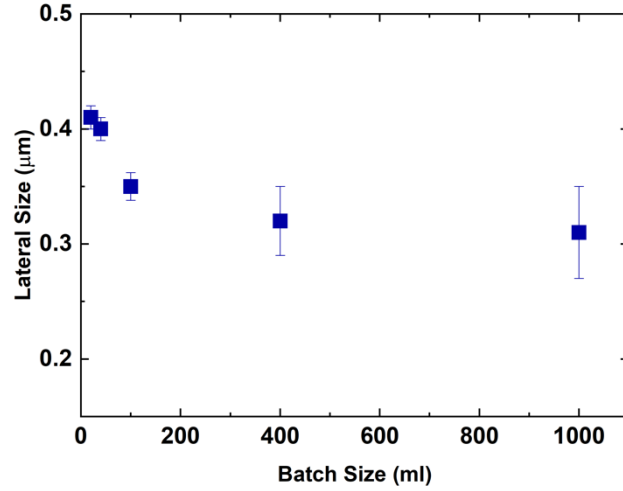


*Figure 0.2 The lateral size of graphene platelets produced by wet ball milling was calculated to be  $\langle L \rangle > 0.3 \mu\text{m}$  regardless of batch size. Subsequent to determining defect source in shear exfoliated graphene, Raman spectra can statistically be analyzed to give mean lateral size of graphene platelets ( $\langle L \rangle$ ).*

The lateral size of graphene platelets were calculated using Equation 1.1. While,  $k$  is the experimentally measured value set equal to 0.17 and  $(I_D/I_G)_{\text{Graphite}}$  has been measured equal to 0.02 from the Raman spectra of raw graphite powder.

$$\langle L \rangle = \frac{k}{\left(\frac{I_D}{I_G}\right)_{\text{Graphene}} - \left(\frac{I_D}{I_G}\right)_{\text{Graphite}}} \quad (1.1)$$

It is worth noting that such production method can result in a broad distribution of particle sizes.

Therefore it is essential to characterize the type of defects that may be introduced during the sheer exfoliation process as demonstrated in Figure 1.3.

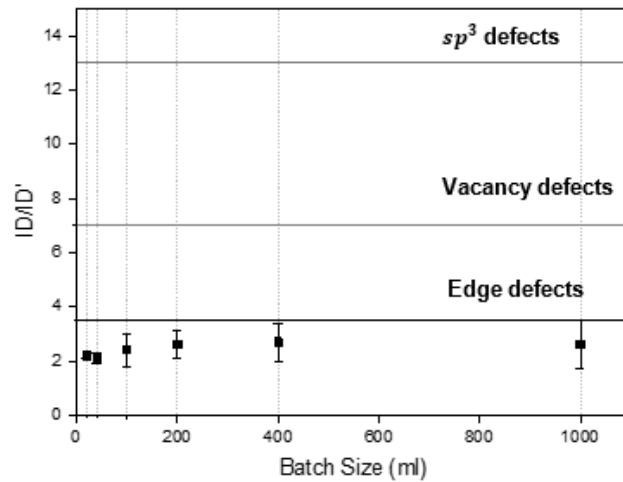


*Figure 0.3 Oxidation, Vacancy and edge defects in various graphene batch sizes.*

Figure 1.4 presents transmittance electron microscopy (TEM) images of graphene sheets which are accumulated in water.

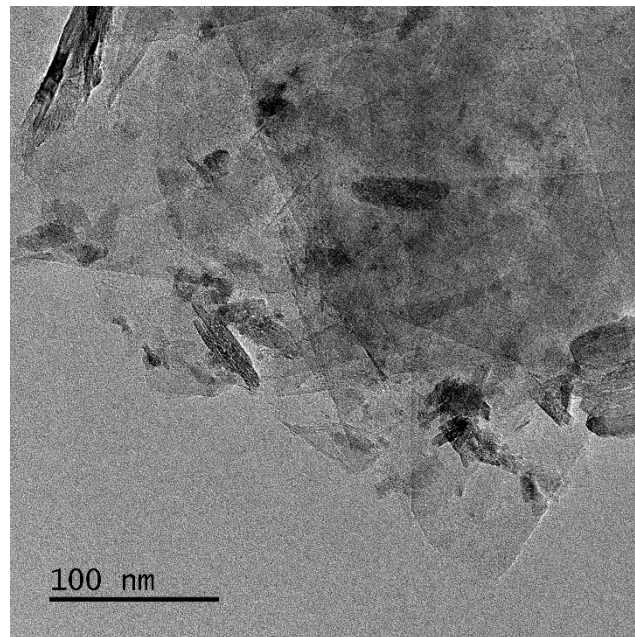


*Figure 0.4 TEM imaging of shear exfoliated graphene demonstrates a distribution of graphene flake sizes. While, thinner and laterally larger flakes are more desirable, the graphene sheets tend to stack up after exfoliation; Scale bar: 100 nm.*

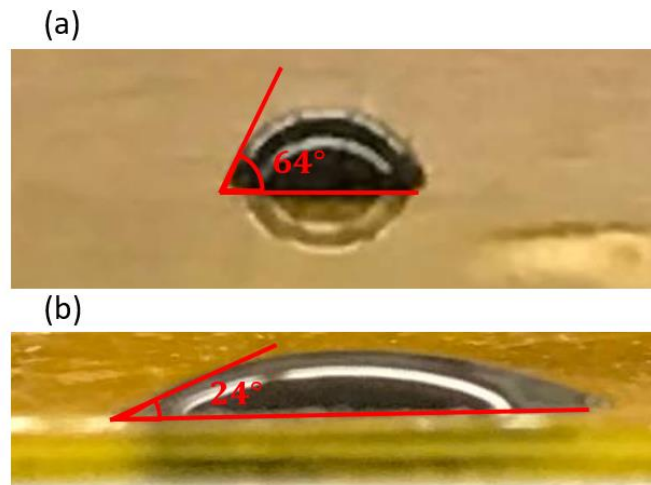


*Figure 0.5 Surface modification of polyimide film enhances the hydrophilicity of the substrate for inkjet printing process with the change in the contact angle of graphene ink from (a) 64° on untreated PI tape to (b) 24° on treated PI.*

After tailoring the graphene solution for inkjet printing process, it is vital to enhance the surface wettability of the flexible substrate (Kapton Polyimide here) to ensure consolidation of graphene patterns. As detailed in the following chapters and Figure 1.5, surface modification of polyimide film leads to a significant increase in the contact angle of the ink droplets.

Chapter 3 details the seeding of N27 rat dopaminergic neuronal cells as depicted in Figure 1.6.

The goal is to ensure high viability of neuronal cells at the time of interfacing by graphene.

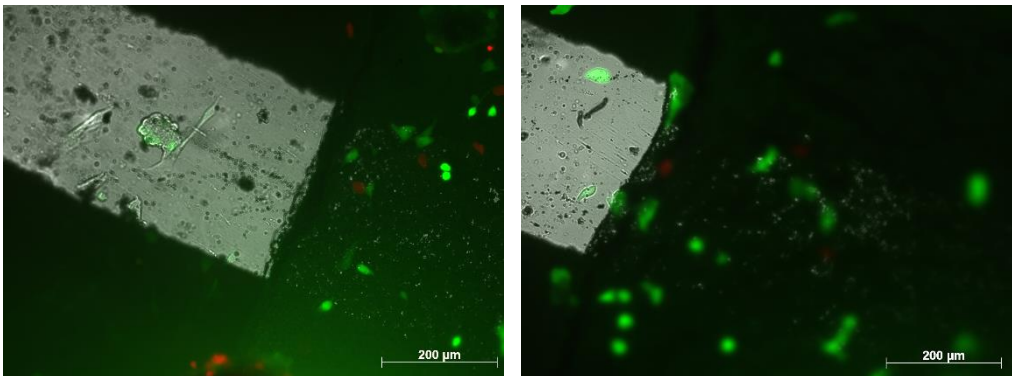


*Figure 0.6 Live–dead cell assays were performed using a 70 μM CellTracker™ CMFDA solution combined with an 8 μM propidium iodide (PI) solution in FBS-free RPMI medium. N27 cells in vitro after 72h at 37 °C in a 5% CO2 environment deposited on graphene prints. Live cells are shown in green, and dead cells are in red; scale-bars: 200 μm. For further details on cell imaging and deposition process refer to reference 45.*

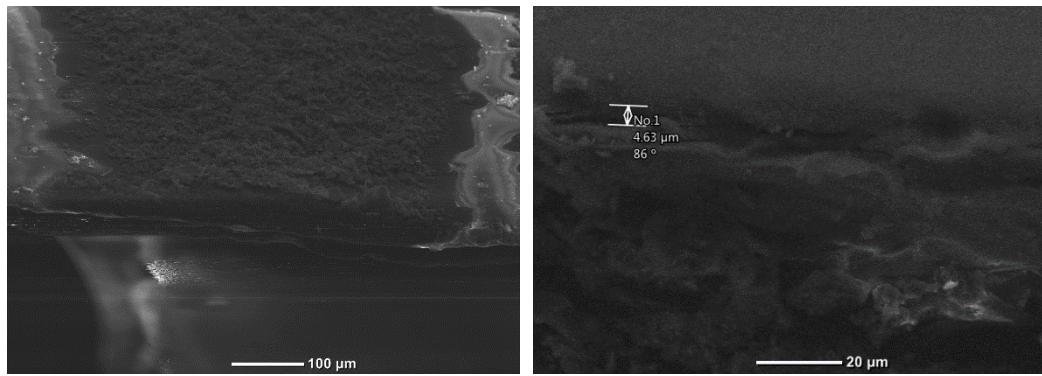


*Figure 0.7 Cross-section of graphene lines captured by SEM. Homogeneous normal height of graphene along the line is demonstrated. The majority of the graphene ink is deposited along the centreline, which resulted in dome-like profile. Left image scale bar: 100  $\mu\text{m}$ ; Right image scale bar: 20  $\mu\text{m}$ .*

The microscale pattern structure of printed graphene is also required to facilitate adhesion of the cell network upon bending and flexure. Figure 1.7 demonstrates the scanning electron microscopy images of patterned graphene in microscale. The dome-shaped cross section of the printed lines, enables stability of the structure upon flexure. The results of extensive experiments on the effect of flexure, bending and folding on electrical characteristics of graphene patterns are presented in chapter 4. As an example Figure 1.8 demonstrates flexure of such patterns under the radius of curvature of 6.3 mm.

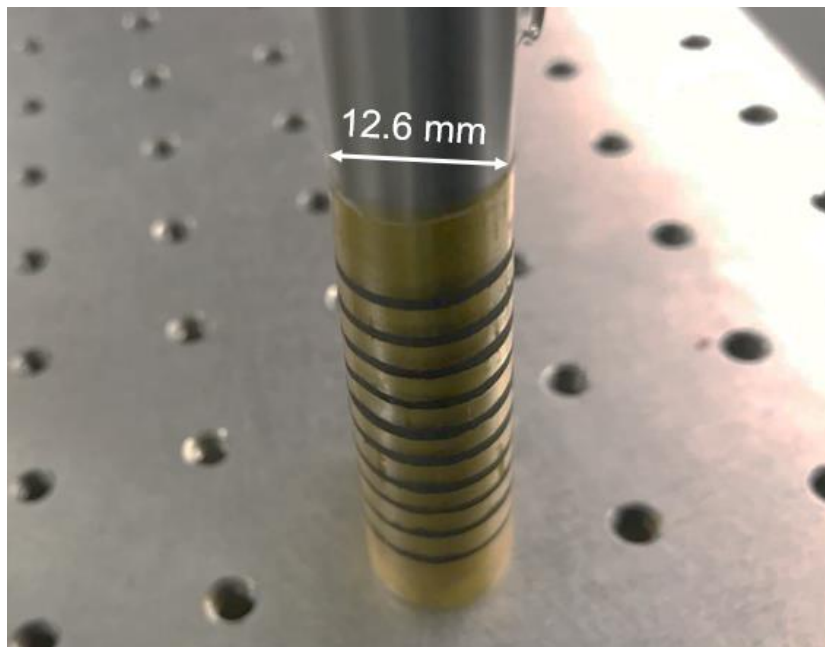


*Figure 0.8 The electrojet printed graphene microelectrodes under flexure with radius of curvature of 6.3 mm.*

When the microelectrode array is in hand, the data acquisition system from Figure 1.9 can be utilized to capture electrochemical behavior of the neurons in real time.

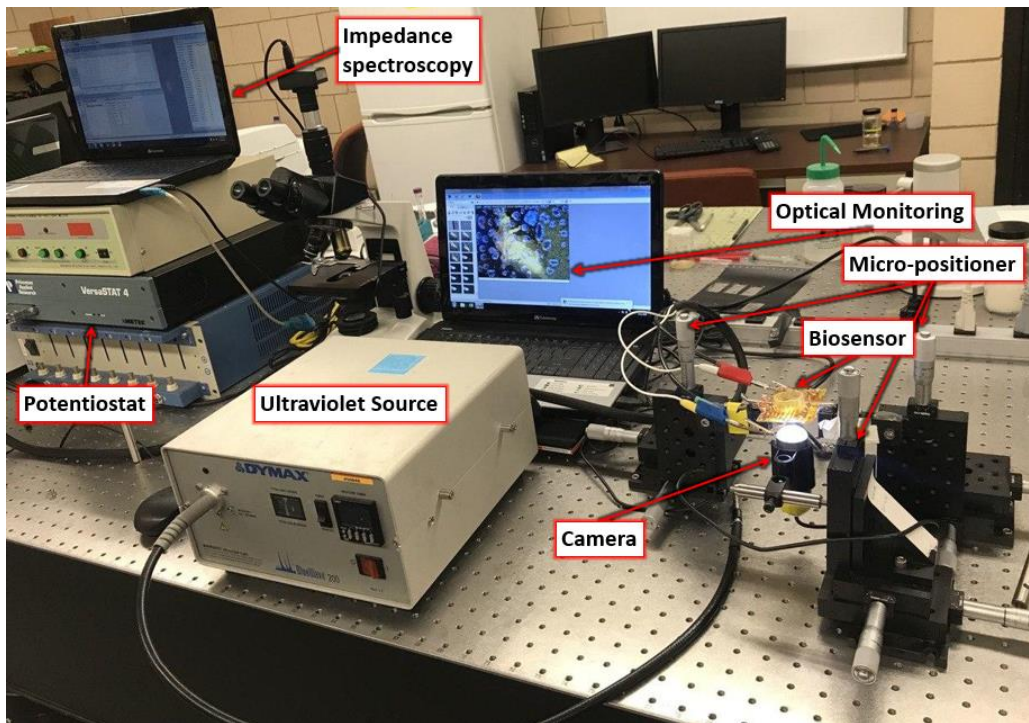


Figure 0.9 The annotated components for real-time optical and electrical monitoring of neuronal cells.

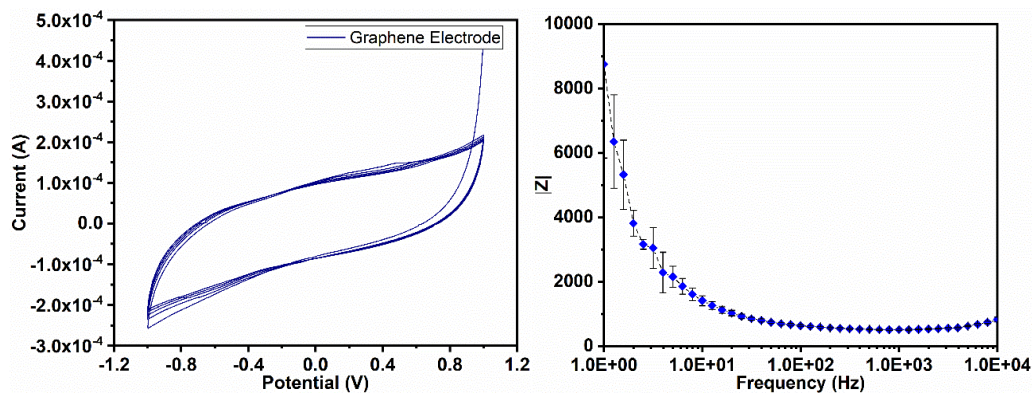


Figure 0.10 Electrode characterization test in standard ionic solution. (left) Cyclic voltammetry of inkjet-printed graphene electrodes in 1 M KCL solution. The data for 5 repetitive cycles are reported with scan rate of 100 mV/s. (Right) Electrical impedance spectroscopy of the electrodes reported in Ohms and scanned between 0.1 Hz and 10 kHz in PBS solution.

Finally, the created microelectrode array is characterized through cyclic voltammetry and electrical impedance spectroscopy (Figure 1.10) to set the truth ground for the cell measurements with the details provided in the chapter 4. The next chapters are structured as follows: Chapter 2 provides a detailed explanation on direct liquid-phase exfoliation of the graphene from graphite via wet ball

milling. Both the production technique and the prepared ink are studied in terms of quality, scalability along with nano-scale and micro-scale characterizations. Furthermore, insights on electrohydrodynamic patterning of the formulated ink on flexible substrates are presented to ensure reproducibility of methodology. In Chapter 3, details on cell interfacing and various viability tests are provided. Chapter 4, dives deeper to the applicability of the biosensor under flexure. Moreover, the method for impedance-based cell viability sensing is presented along with damage exposure to conclude the work. Ultra violet pulses are utilized as source of damage exposure to provide a proof of principle for the applicability of the biosensor for real-time monitoring of cell network without conventional staining techniques. Finally, in chapter 5 suggested future work based on this study is presented.

## CHAPTER 2. HIGH-YIELD PRODUCTION OF AQUEOUS GRAPHENE FOR ELECTROHYDRODYNAMIC DROP-ON-DEMAND PRINTING OF BIOCOMPATIBLE CONDUCTIVE PATTERNS

Modified from a manuscript with the same name published in Biosensors.

*Amir Ehsan Niaraki Asli<sup>1</sup>, Jingshuai Guo<sup>1</sup>, Pei Lun Lai<sup>1</sup>, Reza Montazami<sup>1</sup>, Nicole N. Hashemi<sup>1,2,\*</sup>*

1 Department of Mechanical Engineering, Iowa State University, Ames, IA 50011, USA;

2 Department of Biomedical Sciences, Iowa State University, Ames, IA 50011, USA;

### Abstract

Presented here is a scalable and aqueous phase exfoliation of graphite to high yield and quality of few layer graphene (FLG) using Bovine Serum Albumine (BSA) and wet ball milling. The produced graphene ink is tailored for printable and flexible electronics, having shown promising results in terms of electrical conductivity and temporal stability. Shear force generated by steel balls resulted in 2-3 layer defect-free graphene platelets with an average size of hundreds of nm and with concentration of about 5.1 mg/ml characterized by Raman spectroscopy, atomic force microscopy (AFM), transmittance electron microscopy (TEM) and UV-vis spectroscopy. Further, a conductive ink was prepared and printed on flexible substrate (Polyimide) with controlled resolution. Scanning electron microscopy (SEM) and Profilometry revealed the effect of thermal annealing on the prints to concede consistent morphological characteristics. The resulted sheet resistance was measured to be  $R_s=36.75 \Omega/\text{sqr}$  for prints as long as 100 mm. Printable inks were produced in volumes ranging from 20 ml to 1 L with potential to facilitate large scale production of graphene for applications in biosensors as well as flexible and printable electronics.

### 2.1 Introduction

Printable electronics have received increasing attention due to their broad applications such as roll-to-roll (R2R) printed solar cells,[1] micro electrode array (MEA),[2] biomedical/chemical sensors,[3] and manufacturing of various flexible electronics.[4–6] As the printable inks are core components in this field of research, several studies have been conducted on increasing the conductivity

and printability of these materials. Metal nanoparticles[7] and nanowires,[8] conductive polymers,[9] and Indium Tin Oxide (ITO) are the most common conductive inks. However, natural brittleness of these materials (e.g. ITO) hinders their applicability to the flexible substrate.[10] In biological sensing applications, utilizing these materials alters cell shape, organization and function of the cell culture and therefore establishing a reliable communication remains a challenge due to this mechanical mismatch.[2]

Graphene-based inks have shown promise in fulfilling the aforementioned needs.[11,12] Graphene is an one-atom-thick, two-dimensional, honey-combed arrangement of hybridized carbon atoms, the large scale production of which has remained a challenge since 2004.[15] Researchers have synthesized graphene by oxidation of graphite through modified Hummer's method, chemical vapor deposition (CVD) from hydrocarbon gas and liquid-phase exfoliation.[14] At this time, it is evident that, the Hummer's method causes single carbon atom defects and nano-sized holes, due to over-oxidization of carbon framework.[19] As graphene oxide is insulating, oxidation is commonly unwanted in electronic applications. Although there has been notable improvements on its processability, electronic characteristics of these graphene-based inks are not equal to those of pristine graphene even after chemical reduction.[20] On the other hand, large continuous graphene films can be created by CVD, however, this method has shown limited success due to the presence of numerous surface voids and defects.[21] Additionally, one of the issues with transferring CVD graphene into the desired substrate is the unwanted residues of the etching agents.[22]

Direct Liquid Phase Exfoliation (LPE) of graphite into graphene has been broadly reported to be desirable for inkjet printing, particularly so for electrophysiology and cell-based studies.[25–28] To this date, there are several reported LPE methods, all of which vary in resultant quality and yield.[21,28,29] Popular graphene solvents such as dimethylformamide (DMF) and N-methylpyrrolidone (NMP)[30] often result in low graphene concentration in the conductive ink ( $\sim 0.01 \text{ mg ml}^{-1}$ ),[28] and possess very low viscosity ( $< 2 \text{ cP}$ ) placing them far from practical applications.[31] Furthermore, DMF and

NMP are toxic and in consequence, detrimental to cell cultures.[32] Since, most biological media and cell cultures are aqueous, stable and processable dispersion of aqueous graphene is essential to facilitate the use of this material in biomedical applications.[13,16-18,23-27, 33] Fortunately, in numerous electrochemical studies, it is shown that excitable cells grow compatibly with presence of graphene in the extra-cellular environment.[34,35] However, graphene platelets do not naturally remain suspended in water and aggregate due to the inter-planar Van der Waals interactions.[36]

In order to overcome this issue, Paton *et al.* successfully exhibited usage of an edible protein, bovine serum albumin (BSA) as a stabilizing agent in the LPE process.[46] Kumar *et al.* have shown that BSA among other proteins, facilitates graphite exfoliation with the highest throughput.[37] Khademhosseini *et al.* produced graphene using BSA and sonication to exfoliate graphite for biomedical purposes.[38] Nevertheless, it has become evident that continuous sonication is ineffective for providing a higher graphene yield, and excessive sonication can result in damage to graphene.[28,39]

It has been long known that other mechanical activation techniques, such as ball milling, can be considered as a promising process for modifying carbon nanostructures.[40] To the knowledge of the authors, thus far ball milling has been used to exfoliate graphite in solid condition with melamine in two separate studies, resulting in maximum concentration of  $0.13 \text{ mgml}^{-1}$ , [41] and  $0.37 \text{ mgml}^{-1}$ , [62] in DMF. Wet ball milling was utilized to produce FLG in NMP.[42] Edge-carboxylated graphene nanosheets can be produced via ball milling in dry ice which results in a very high conductivity but with the concentration of  $0.06 \text{ mgml}^{-1}$ . [63] In consequence, attaining higher concentrations of graphene as a conductive ink while suspending graphene sheets in water remains a desired task in hand.

In the course of printing, high concentration of graphene in solution serves threefold purpose. Firstly, the more concentrated the graphene solution, the more viscose the ink, which in practice should reach to approximately  $10 \text{ cP}$ . [32] Adversely, The low concentration of graphene demands several tens of print passes for obtaining functional films.[14,43] Finally, concentration of graphene is correlated

with the conductivity of the ink, which serves as a control factor in the electrostatic field induced by the drop-on-demand systems.[44]

Herein, we initially propose the combination of BSA as an exfoliating/stabling agent, with the shear force of continuous low speed wet ball milling for achieving scalable and stable water-dispersed graphene nanosheets with high yield. Next, through utilizing an electrostatic field, the inkjet printing of binder-free graphene solution on flexible substrate is demonstrated. To end with, the resultant conductivity of the printed circuit is characterized and its stability after submergence in water is exhibited. In another study by our group, the biofunctionalization of the biosensors produced via this process is exhibited.[45] It is shown that, rat neuronal cells can be cultured *in-vitro* on graphene biosensors and these sensors can enable sensing of electrical signals on cell membrane. This study aims to provide a practical guideline for production of highly concentrated graphene and patterning of circuits for use in biosensing and other applications in flexible electronics.

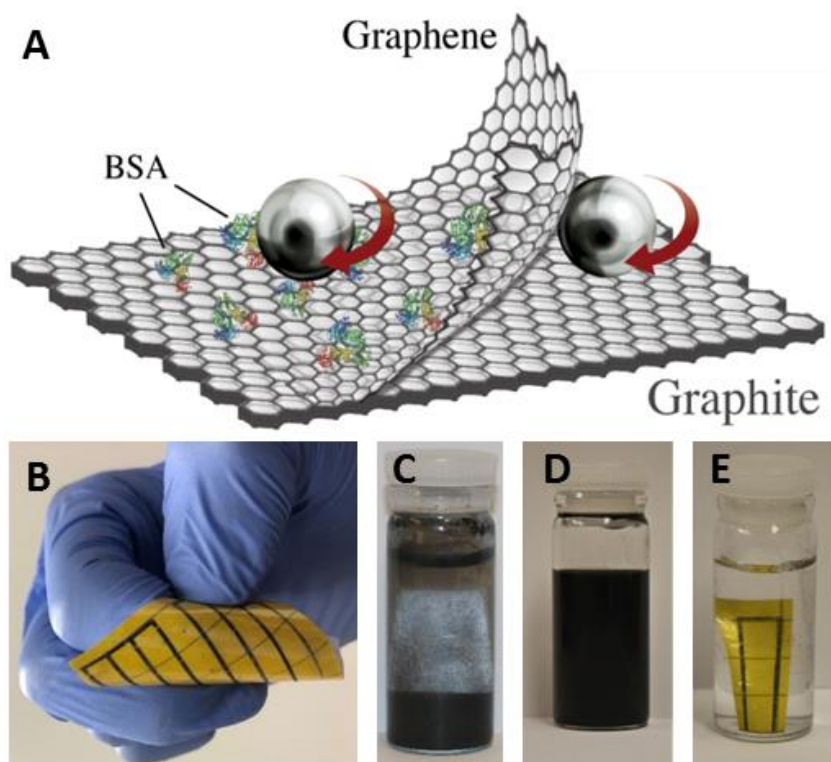


**Figure 0.1** Shear exfoliation of graphene from Graphite in water. A) Schematics of shear exfoliation of graphite using steel balls with presence of BSA proteins B) Printed graphene ink on flexible substrate C) Graphite powder in water before exfoliation D) Graphene ink with concentration of  $5.1 \text{ mgml}^{-1}$  after remaining still for one month. E) Stability of graphene patterns after 7 days of submergence in water.

## 2.2 Materials and Methods

Graphite crystallites ( $\approx 20 \mu m$ ) were exfoliated and broken down to FLG platelets via the shear tension created by abrasion of steel balls with the diameter of 11/32" (Figure 1A). Since turbulent energy dissipation is not necessary for exfoliation,[46] the rotational speed was fixed as low as 300 rpm for 90 h in all trials to prevent undesired temperature spikes. The proportion of Graphite ( $[Graphite]_0 = 20 mg mL^{-1}$ ), BSA ( $[BSA]_0 = 2 mg mL^{-1}$ ) and  $r_{bs} = 500 \pm 10 m^2/m^3$  were constant for all the results reported in this study, where  $r_{bs}$  is the ratio of overall surface area of the balls with respect to solution volume.

BSA is an inexpensive protein and most commonly found as a waste product in the meat industry,[47] which plays a key role in preventing aggregation of exfoliated platelets. While the large hydrophobic surface area of graphene nanosheet bonds with hydrophobic segment of BSA, the hydrophilic fragment of BSA interacts with water molecules. It is important to note that, through interactions with BSA, the structural and intrinsic properties of graphene nanosheets alters minimally, as it is believed that BSA enables stabilization of graphene through non-covalent bonding.[48]

The ball milled solution was allowed to rest for  $\sim 48 h$ , as is evident not all the graphite particles can be exfoliated to desired FLG. Therefore, the thicker graphene sheets, having failed to maintain their bond with BSA, aggregated with unbroken graphite particles and settled prior to separation of graphene solution from its sediment. The solution was further centrifuged at 1500 rpm for 45 min and 85% of the volume from the top was pipetted off. The purpose of this centrifugation is both to remove the remaining graphite particles from the solution and to ensure no Fe impurity from the steel balls can contaminate the samples. Finally, the concentration of the resultant graphene solution was investigated by UV-vis spectroscopy in different batch sizes to demonstrate the scalability of the method.

The quality of initial graphite crystallites plays a significant role in the quality of the resultant graphene solution,[37] and the further studies on the influence of graphite on the produced graphene is left to be addressed elsewhere. The quality of the produced graphene was examined by UV-Vis spectroscopy, Raman spectroscopy, TEM and AFM as given below.

Absorption spectra were recorded on a PerkinElmer UV-Vis spectrophotometer (Lambda 750) at  $\lambda = 660$  nm in room temperature. The value of the absorbance coefficient  $\alpha$  was obtained by measuring the absorption of the dispersion per length  $A/l$ , at various controlled dilutions:

0.05, 0.08, 0.11, 0.14, 0.17, 0.20  $\text{mg ml}^{-1}$ . The mass of the remaining film after evaporation of water in controlled concentrations was measured for 5 ml samples. The resultant absorption coefficient of  $\alpha = 3525 \text{ mlmg}^{-1}\text{m}^{-1}$  (Figure 3) was implemented in Beer-Lambert law to give resultant concentration measurements ( $C = \alpha A/l$ ).[46]

Raman spectra of the thin films on alumina membranes were acquired using a Raman spectrometer (Voyage, B&W Tek, Inc.), with a CW laser Excelsior-532-150-CDRH Spectra-Physics) as the energy source operating at wavelength of 532 nm. Graphene ink drops were dried on a Si/SiO<sub>2</sub> glass chips with diameter  $\approx 10$  mm. There were little variations in the spectra acquired in different laser spots, thus an average of 5 different points on each sample was reported here.

TEM images were recorded using a JEOL JSM2100 STEM (Japan Electron Optics Laboratories) at 200kV accelerating voltage. Graphene samples were diluted to 20  $\mu\text{g ml}^{-1}$  and were drop casted on a Cu-grid. The AFM images were captured on a Bruker dimension Icon AFM in contact mode and were analyzed by NanoScope Analysis software, version 1.50. Optical microscopy images were recorded by using a Zeiss Axio Observer Z1 Inverted Microscope. The waviness and roughness of graphene prints were monitored via a non-contact optical Profilometer, Zygo 7100. We reduced the effect of local roughness to find the cross sectional profile of prints by calculating average of the heights in circles with radii of 1  $\mu\text{m}$  and their centers are located in the line demonstrated in Figure S4. SEM Images of

printed graphene patterns on PI were captured via a JEOL FESM 6335 using 2-5kV accelerating voltage. The resistance measurements were conducted by a VersaSTAT 4 Potentiostat Galvanostat.

Physical properties of graphene ink itself are critically influential in controlling the resolution and consistency of the printed patterns. Hence, two nondimensional properties: Reynolds number and Weber number (Equation 1 and 2) were utilized to govern the printability of the ink.[59] Consequently, the flow rate and the intensity of the electrostatic field applied to the substrate were tuned in the experiments, resulting in average  $Re = 45.1$  and  $We = 33.7$  for the reported ink and setup. Reynolds and Weber numbers are related by Ohnesorge number ( $Oh$ ) which describes the jettability of an ink regardless of the velocity of ink drops . [60] Suggested by Derby et al. for proper jetting to occur,  $Z$ -value (inverse of  $Oh$ ) should be between 1 and 10 and the drop impact ( $K_c$ ) be below 100.[61]

$$Re = \frac{v\rho a}{\mu} \quad (1)$$

$$We = \frac{v^2\rho a}{\gamma} \quad (2)$$

$$Z = \frac{1}{Oh} = \frac{Re}{\sqrt{We}} = \frac{(\gamma\rho a)^{\frac{1}{2}}}{\mu}; 1 < Z < 10 \quad (3)$$

$$K_c = We^{0.5}Re^{0.25}; K_c < 100 \quad (4)$$

Where  $v$  is the impact velocity,  $\rho$  is the ink density,  $a$  is the diameter of jetting nozzle,  $\mu$  is the viscosity of the ink and  $\gamma$  is the surface tension. The conditions for the  $Z$ -value and the drop impact, given in Equation 3 and 4, were satisfied to obtain a printable ink. These equations confirm that, the ink is not too viscous to clog the needle or the junctions and not too diluted to splash while maintaining high flow rates. High flow rate is essential for achieving superior conductivity outcomes for single printing pass. The measured  $Re$  and  $We$  for the reported ink and setup was 25.1 and 33.7 respectively. These were measured at room temperature, resulting in  $Z$ -value of  $Z = 4.32$  and drop impact of  $K_c = 12.99$  which satisfies the suggested conditions.

Polyimide film has a hydrophobic surface which requires surface modification for inkjet printing. PI film was washed with water and acetone before plasma cleaning, then submerged in a solution of PSS in DI water ( $12 \text{ mg mL}^{-1}$ ) and NaCl ( $0.5 \text{ mol L}^{-1}$ ) for 20 minutes followed by submergence in a solution of PEI in DI water ( $30 \text{ mg mL}^{-1}$ ) and NaCl ( $0.5 \text{ mol L}^{-1}$ ) for another 20 minutes. The substrates were finally thoroughly washed with DI water and dried by pressurized nitrogen. In the course of printing, 5 ml Syringe filled with graphene ink was fixed in an syringe pump, to inject the ink with the rate of  $9 \mu\text{L s}^{-1}$  for needles with inner diameter of  $300 \mu\text{m}$ . Kapton PI tape was fixed on an aluminum film and a 3 kV potential difference was applied between the tip of the needle and aluminum film to adhere the ink onto the substrate. The position of the tip of the needle was controlled through a Computer Numerical Control and all the printed graphene are a result of one pass of the needle over the substrate for 120 mm with the movement speed of 10 mm/s.

Graphite powder ( $\approx 20 \mu\text{m}$ ), BSA, Poly 4-styrenesulfonic acid sodium salt (PSS), Poly ethyleneimine (PEI) 50% (w/v) in  $\text{H}_2\text{O}$ , graphene dispersion ( $\geq 0.2 \text{ mgml}^{-1}$  in DMF) with sheet resistance of  $24.2 \text{ k}\Omega/\text{sqr}$  (as made),  $7.9 \text{ k}\Omega/\text{sqr}$  (after 30 min,  $200 \text{ }^\circ\text{C}$ ); and graphene dispersion ( $1 \text{ mgml}^{-1}$  in DMF) with sheet resistance of  $16 \text{ k}\Omega/\text{sq}$  (as made),  $4.1 \text{ k}\Omega/\text{sq}$  (after 30 min,  $200 \text{ }^\circ\text{C}$ ), were purchased from Sigma-Aldrich (St. Louis, MO).

## 2.3 Results and Discussion

### 2.3.1 Graphene Characterization

Former studies have revealed that the physical properties of graphene-based materials are determined by their structure, number of hexagonal carbon layers which also represents thickness, the defects or contaminants present in the material.[22] Raman spectroscopy is the most widely accepted way to gain information on these physical characteristics.[49,58] In this study, Raman spectra of the graphene (**Figure 2E**) indicate that the most noticeable intensities belonged to D ( $\approx 1348 \text{ cm}^{-1}$ ), G ( $\approx 1569 \text{ cm}^{-1}$ ), D' ( $\approx 1620 \text{ cm}^{-1}$ ), and 2D ( $\approx 2695 \text{ cm}^{-1}$ ) bands which typically contain information regarding defects, lateral size, and number of layers of exfoliated graphene platelets. One of the most

prominent characteristics for Raman spectrum of graphene, compared to graphite, is the elimination of shoulder peak on the 2D band. This is most likely due to growth in the number of aromatic domains.[46]

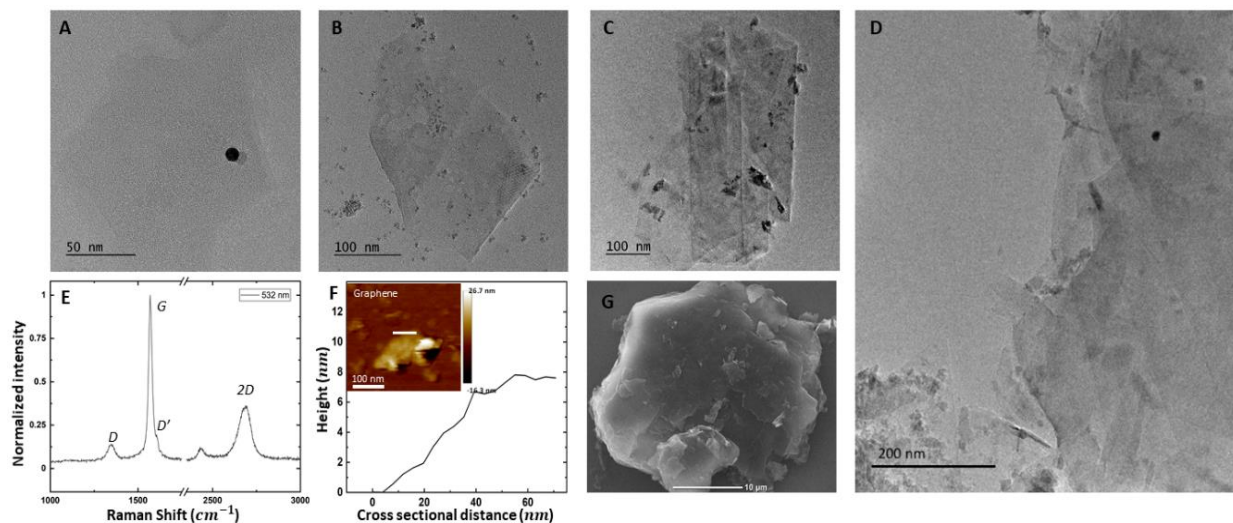


Figure 0.2 Characterization of shear exfoliated graphene from graphite particles in water. A) Single graphene flake, which is semi-transparent; scale bar: 50 nm. B) TEM image of single FLG which is folded due to its large aspect ratio; scale bar: 100 nm. C) Multiple graphene flakes with crumpled and folded morphology; scale bar: 100 nm. D) TEM imaging demonstrates a distribution of flake sizes that tend to stack up; Scale bar: 200 nm. E) Raman spectra of Graphene sample in 5 different laser spots. F) AFM image and corresponding height profile of graphene. G) SEM Image of Single Graphite particle; scale bar: 10  $\mu\text{m}$

Another significant sign of presence of graphene is the intensity of D band which is barely observable in graphite samples,  $(I_D/I_G)_{\text{Graphite}} = 0.02$ , and markedly increased to  $(I_D/I_G)_{\text{Graphene}} = 0.16$ . [38,50] In addition, although the G band remained unchanged, there appeared the D' band shoulder peak. D and D' bands are created due to the shear force produced by steel balls which effectively break the graphite crystals into FLG platelets. It was found by Eckmann et al. that the ratio of intensity values of the D band ( $I_D$ ) and the D' band ( $I_{D'}$ ) can quantitatively denote disorders, vacancy defects and possible oxidization,[49] which degrades electrical characteristics of FLG. By their very nature, graphene nanoplatelets contain edges which act as defects. The type of these defects must be identified, and it should be determined that whether the presence of D band is due to basal plane defects or nano sheet edges, before the graphene materials are to be used. It is known that the values of  $I_D/I_{D'} > 3.5, 7, 13$  respectively characterize boundary defects, vacancy basal plane point defects and  $sp^3$  defects.[46] The ratio of these peaks was measured to be  $I_D/I_{D'} < 3.5$  in all batch volumes, which can be interpreted as no

observed  $sp^3$  defects (oxidization) or vacancy defects during exfoliation process. Changes of  $I_D/I_D'$  in different batch volumes is given in **Figure S1**.

In order to further confirm the presence of defect-free graphene and degree of exfoliation, transmission electron microscopy (TEM) images were collected using dried, deposited graphene ( $20 \mu\text{g mL}^{-1}$ ) on a Cu-grid (Figure 2A-D). No basal defects, cracks or holes were observed in graphene nanosheets, supporting the Raman tests. In many instances, the sheets are found to exhibit a folded or crumbled morphology. This could explain the discrepancies for average lateral sizes measured by TEM when compared to Raman results (Figure 2E). Overall, TEM showed that most graphene sheets had a maximum lateral dimension on the scale of hundreds of nm and supported the successful exfoliation of graphite to defect-free FLG.

The number of layers in FLG platelets, can be quantitatively estimated based on the shape of the  $2D$  band of both shear exfoliated graphene and source graphite powder given in Equation 5.[46]  $M$  is a metric proposed by Paton et al.[46] (Equation 6), where  $\omega_p$  is the intensity of  $2D$  peak and  $\omega_s = \omega_p - 30 \text{ cm}^{-1}$  is the intensity of the left hand-side shoulder peak. In various batch sizes,  $N_G$  was resulted to be  $2.9 \pm 0.3$ . It is worth noting that the calculated  $N_G$  is highly sensitive to parent graphite and can vary in other experiments.

$$\langle N_G \rangle = 10^{0.84M + 0.45M^2} \quad (5)$$

$$M = \frac{I_{G'ene}(\omega = \omega_{p,G'ite})/I_{G'ene}(\omega = \omega_{s,G'ite})}{I_{G'ite}(\omega = \omega_{p,G'ite})/I_{G'ite}(\omega = \omega_{s,G'ite})} \quad (6)$$

We used atomic force microscopy (AFM) to analyse the thickness of the graphene nanosheets after stabilization with BSA. The height-profile images of the graphene sheets revealed that they had a thickness of  $7.6 \pm 2.3 \text{ nm}$ , suggesting the presence of few-layer graphene sheets in aqueous dispersion (Figure 2F). Note that the relatively high thickness of fabricated graphene is due to the absorption of BSA on its surface.[51]

### 2.3.2 Scale-up Study

A significant factor in the process of exfoliating graphene from pristine graphite is the scalability of the production method. The bio-graphene presented here preserves its qualities such as consistent yield, lateral size, conductive characteristics and devoid of defect. In order to increase the batch volume, the number of balls was chosen based on the ratio of the overall surface area of the balls to the volume of solvent ( $r_{bs}$ ). Graphene ink was produced in batch volumes varying from 20 – 1000 ml with  $r_{bs} = 500 \pm 01 \text{ mm}^2/\text{mm}^3$ . Measured conductivities remained unchanged and the printed graphene remained stable under flexing. **Figure 3** demonstrates graphene yield from the wet ball milling taken from various volumes as measured via UV-vis spectroscopy. It appears that more graphite particles left the mixture as sediment in larger batches. However, the production method can lead to graphene concentration of  $5.1 \text{ mg ml}^{-1}$  regardless of volume for batches greater than 200 ml. Concurrently, change of lateral size in different batch sizes can contribute to quality and scalability of the production method. Hence, Raman spectra of the samples in different batch volumes were used to statistically estimate the mean lateral size of the graphene platelets (**Figure 2D,S2**). This lateral size (approximation further confirms the TEM findings (Figure 2B, **S3**), as liquid phase exfoliation typically results in a distribution of flake sizes in each sample.

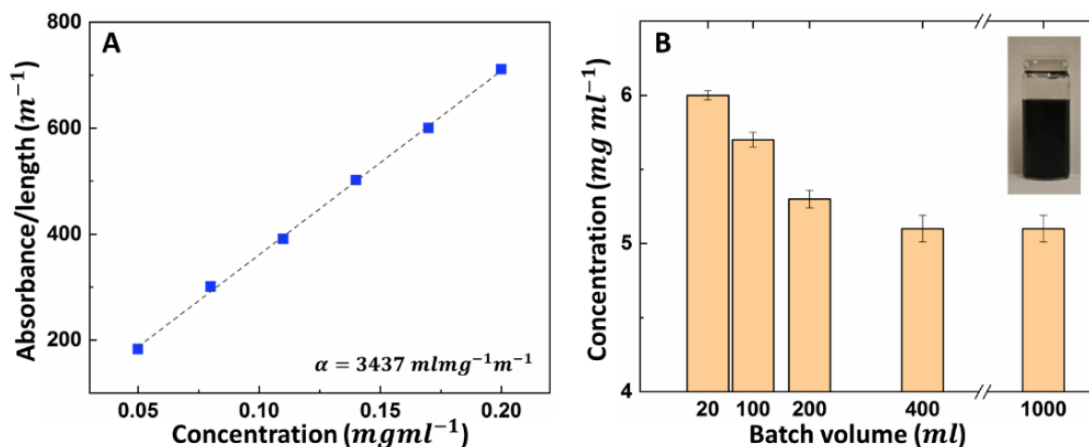
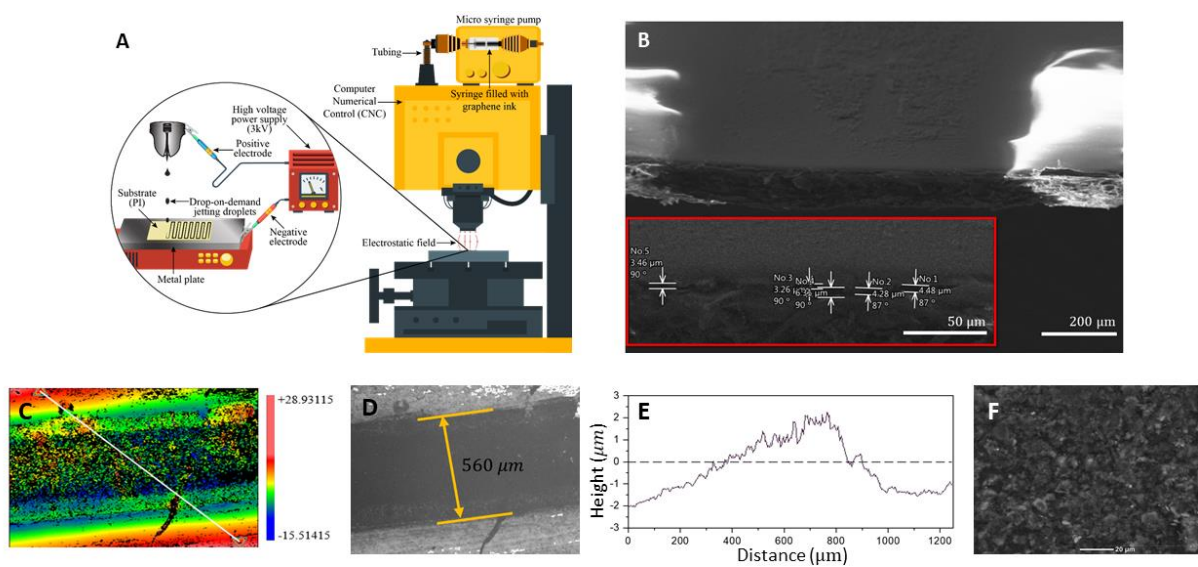


Figure 0.3 Graphene concentration measured given by UV absorption. A) Absorption coefficient obtained from UV-vis spectroscopy at  $\lambda=660 \text{ nm}$ . B) Change of graphene concentration with respect to batch sizes varying from 20 ml to 1000 ml. The resultant concentration of wet ball milled graphene remain constant ( $5.1 \text{ mg ml}^{-1}$ ) for batches larger than 400 ml.

### 2.3.3 Ink Formulation and Printing

Graphene ink was applied to Kapton Polyimide (PI) using a custom designed printing setup demonstrated schematically in **Figure 4**. As the produced FLG aqueous solution is negatively charged, surface modifications to PI were crucial for improving the hydrophilicity of the substrate prior to printing.[14] Traditionally, conductive inks are printed using commercial the ink out of the nozzle onto the substrate either mechanically or thermally.[46,47] It is commonly reported that microscale cracks appear within the printed lines rendering them susceptible to the deflection of the substrate. In many studies, polymer stabilizers such as ethyl cellulose are added to the ink with the purpose of crystallization at the time of annealing.[14,47] Such binders are often insulators and may not be the most effective post-processing method when it comes to the electronic applications of graphene.[10,52] In order to address the print instability issue and avoid numerous printing passes, we have utilized an electrostatic field to fix the conductive ink on the substrate producing graphene lines on bendable substrates without binders (Figure 1B). In one pass, graphene ink was laid on the substrate and was immediately fixed after, via thermal annealing in a preheated oven at the temperatures and durations given in Figure 5A. In order to consolidate graphene platelets on the substrate, a potential difference with a magnitude of  $3\text{ kV}$  was created between the needle and the aluminum film placed under the substrate. These served as positive and negative electrodes respectively. The chosen PI substrate was  $0.06\text{ mm}$  thick. The tip of the flat-ended needle was set to  $1.2 \pm 0.1\text{ mm}$  from the top surface of the metal plate and its perpendicularity was ensured by the CNC machine. The induced electrostatic force causes liquid meniscus at the interface to form a micro-droplet, which combines with gravity force to overcome the surface tension of the liquid, and is pushed towards the substrate.[44] Due to the surface tension of the graphene ink the positive pressure, caused by the syringe pump cannot result in a constant flow of the ink ( $9\ \mu\text{L/s}$  in the reported experiments). In the absence of electrostatic field, large millimeter-sized drops leave the tip of the needle only after accumulation of ink after several seconds.

Thus, the flow of the ink can be controlled by the presence of the potential difference between the electrodes. The advantage of the printing setup used in this study, as compared to common commercial inkjet printers can be observed in the SEM results. Figure 4F shows minimal disorientation of graphene platelets in post-baked printed patterns, which is advantageous in reducing micro-scale junctions.



*Figure 0.4 A) Drop-on-demand printer setup for inkjet printing of graphene B) SEM for cross-sectional view of printed patterns with magnifications which show a normal height of  $\approx 4 \mu\text{m}$  C) Height contour of full printed graphene and sample line through which average height is reported. D) The 20x magnified section of the sample print. E) In distance 0 and 1200 on the sample line (c), the height is measured over the substrate. the maximum measured height is the peak of the printed material. The difference between these two indicates the height of the print ( $\approx 4 \mu\text{m}$ ) at maximum which is compatible with SEM imaging. F) SEM for top view of printed graphene after annealing at  $280^\circ\text{C}$  for 30 minutes; scale bar:  $20 \mu\text{m}$ .*

The resolution of prints is controlled by: the inner diameter of the chosen needle, the positive pressure behind the ink filled syringe (represented by the flow rate injected by the syringe pump), needle speed along the printed lines and the electric potential difference between the needle's tip and the substrate (see supplementary information for more details). The width of the prints was measured to be  $550 \pm 50 \mu\text{m}$  in all the cases presented here.

### 2.3.4 Post Processing and Electrical Conductivity

The normal height of printed samples directly influences the overall conductivity of graphene lines and their quality. A thick print might collapse and crack after bending and coffee ring effect will

cause an unwanted inconsistency in the thickness of the side edges of the prints.[25,32] The Profilometry results (Figure 4C-E and Figure S5) show that the maximum thickness occurs in the center line of the prints, which indicates that the majority of graphene flakes are deposited in the middle, thereby proving that there was no observable coffee ring effect. This is a stable cross section under tangential stresses across the surface of substrates during flexing.

Post processing is essential for the improvement of the conductivity and stability of the printed FLG. On one hand, it leads to release of possible oxide compounds; and on the other hand, results in BSA burn-off which is essential for maintaining the stability of the patterns when in touch with water. During thermal decomposition, all amino acids emit volatile gases, mainly  $H_2O$  and  $NH_3$ . Nevertheless, the mass of the residues is heavily dependent on the temperature to which they were exposed. At  $280^\circ C$  the residue of some amino acids (i.e. Cysteine) can be reduced to 10% of their initial mass.[64] Thermal annealing reduces flake-to-flake and flake-to-substrate defects while improving the order of the surface morphology.[10,22,53] The prints made from FLG ink was once annealed in various durations ranging from 10 to 120 minutes in constant temperature of  $280^\circ C$  (**Figure 5A**) and once annealed for 30 minutes in temperatures varying from  $50^\circ C$  to  $280^\circ C$  (Figure 5B). As a thermally stable organic substrate, PI is popular among developers of flexible printed circuits due to its capability to maintain its stability across a wide range of temperatures (from  $-269^\circ C$  to  $+400^\circ C$ ).[54] Therefore, it is safe to assume that, the quality of the substrate is not compromised during the annealing process.

Graphene is naturally conductive, due to connection of each carbon atom forms three  $\mu$ -bonds, leaving one out-of-plane electron ( $\pi$  bond) free in the valence shell. The end to end resistance of the lines were measured via a potentiostat (Figure 5C) for lines with mean dimensions of  $100 \times .56 \times .004 \text{ mm}$ . Equation 7 can be used to give the conductivity of the processed graphene  $\sigma \approx 6800 \text{ S/m}$ , For which,  $l$  is the length of the lines,  $w$  and  $t$  are the width and height of the lines respectively, and  $R$  is the measured resistance. Both  $w$  and  $t$  were measured by the profilometer (Figure 4D) at 5 distinct points along the printed lines and the mean values were used for conductivity

measurement. The results show that, although depositing layers of wet ball milled graphene on substrate has a sheet resistance of  $133 \Omega/sqr$ , annealing the samples in a standard oven up to  $280^\circ\text{C}$  can reduce the sheet resistance to as low as  $36.75 \Omega/sqr$ .

$$\sigma = \frac{l}{wtR} \quad (7)$$

It should be noted that, without surface preservatives, the FLG prints reported in this study could be detached from the substrate if scratched or repeatedly folded. We observed that the printed lines could retain their conductivity under flexing (Figure 1B) and remained stable after being submerged under DI water with  $PH = 7$  for over 7 days as a result of BSA burn-off at high temperature (Figure 1E). While there are already commercial graphene inks available, they possess lower concentrations as well as dramatically higher sheet resistance. The concentration and sheet resistance for commercial ink1 and ink2 (supplementary information) are  $C = 0.2 \text{ mg ml}^{-1}$  and  $R_s = 2, 4.8 \text{ k}\Omega/sqr$  respectively (both after thermal processing). Figure 5D,[11,25,31,32,55–57] demonstrates a comparison of the production method in this study with other published records, both in terms of concentration ( $\text{mg/ml}$ ) and resultant sheet resistance.

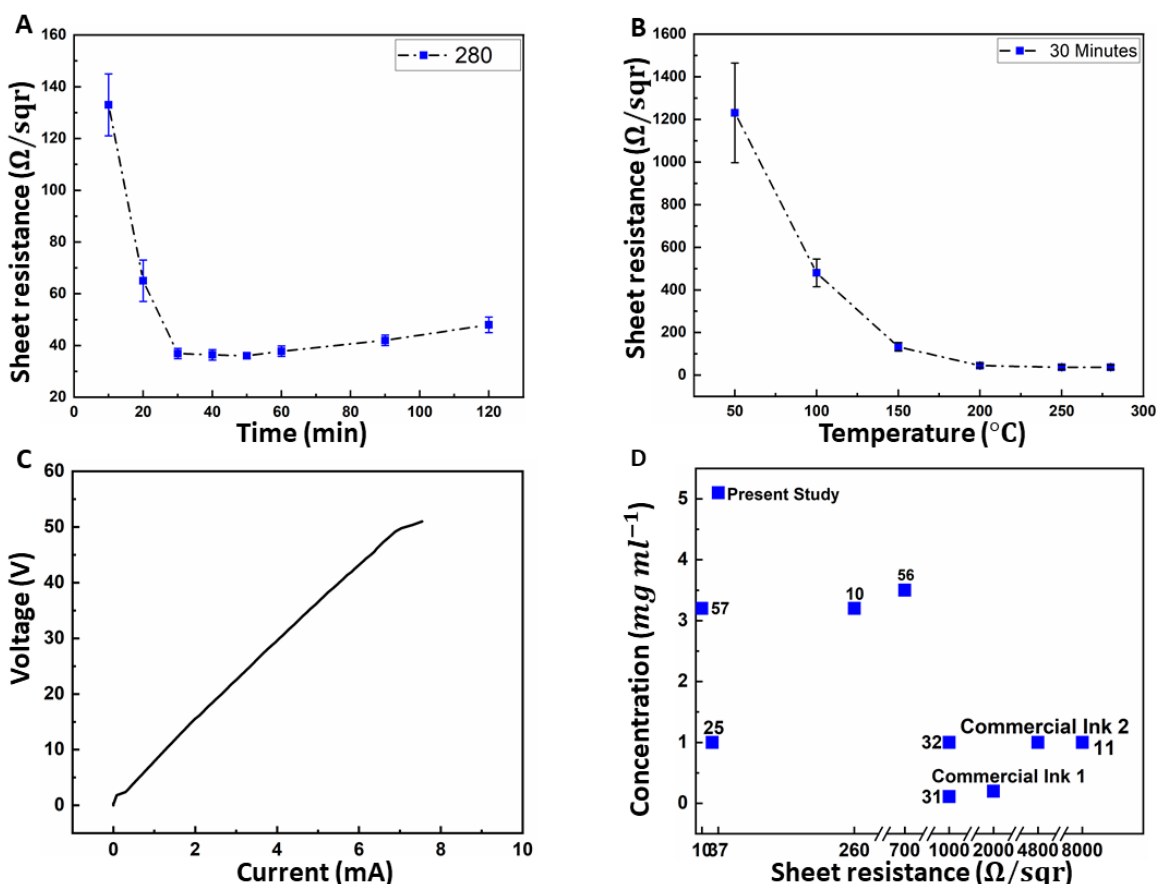


Figure 0.5 A) Change of sheet resistance  $R_S$  of printed graphene with respect to annealing time in  $280^{\circ}\text{C}$  oven. B) Change of sheet resistance of printed graphene with respect to changes in annealing temperature. C) Linear I-V response of the lines with length of 100 mm measured by a potentiostat. D) Comparison of the yield and resultant sheet resistance of produced graphene with other published approaches. In the studies that sheet resistance was not reported directly, their values were estimated by equation 7 using the reported resistivity/conductivity values.

## 2.4 Conclusion

The Production of defect-free and stable graphene dispersion in aqueous medium is vastly desired for biological applications. Particularly, applying conductive graphene patterns on flexible substrates can aid electrophysiological study on neuronal cells by resolving reported mechanical mismatch between biosensors and soft cell membrane. Here we demonstrated a facile graphene production method by combining BSA with wet ball milling for the first time, and further inkjet printed the prepared ink on a flexible polymer, PI. The exfoliation process, starts from graphite particles with the concentration of  $20 \text{ mg/ml}$ , and results in  $5.1 \text{ mg/ml}$  of stable graphene dispersion. The as prepared graphene sheets possess a lateral size on the order of hundreds of nm and are 2-3 layers on average. The

produced dispersion remained stable for weeks, which is advantageous during printing process, as it dramatically lessens the likelihood of clogging issues.

The utilized custom-designed inkjet printer, benefits from an electrostatic force to consolidate the conductive patterns on the substrate. Moreover, The effect of thermal annealing was explored in different durations and temperatures to reduce the sheet resistance of graphene patterns to  $36.75 \Omega/sqr$ , while enhancing their binding to the substrate. The resultant conductive lines did not lose their conductivity nor adhesion to PI when in touch with water, which is desirable as cell media are typically water-based.

In a recent study, our group observed that rat dopaminergic (N27) neuronal cells live compatibly and adhere to the graphene patterns (**Figure S4**) in the biosensing platforms that are made based on aforementioned methodology.[45] These cells are commonly used in vitro, as models for Parkinson disease. Thus, the reported methodology can set the ground for further investigations about electrical signals for cell communications and other applications regarding flexible/printable electronics.

### References

1. Arapov, K.; Rubingh, E.; Abbel, R.; Laven, J.; de With, G.; Friedrich, H. Conductive Screen Printing Inks by Gelation of Graphene Dispersions. *Adv. Funct. Mater.* **2016**, *26*, 586–593.
2. Adly, N.; Weidlich, S.; Seyock, S.; Brings, F.; Yakushenko, A.; Offenhäusser, A.; Wolfrum, B. Printed microelectrode arrays on soft materials: from PDMS to hydrogels. *npj Flex. Electron.* **2018**, *2*, 1–5.
3. Huang, J.; Du, J.; Cevher, Z.; Ren, Y.; Wu, X.; Chu, Y. Printable and Flexible Phototransistors Based on Blend of Organic Semiconductor and Biopolymer. *Adv. Funct. Mater.* **2017**, *27*, 1604163.
4. Jiang, J.; Bao, B.; Li, M.; Sun, J.; Zhang, C.; Li, Y.; Li, F.; Yao, X.; Song, Y. Fabrication of Transparent Multilayer Circuits by Inkjet Printing. *Adv. Mater.* **2016**, *28*, 1420–1426.
5. Wood, V.; Panzer, M.J.; Chen, J.; Bradley, M.S.; Halpert, J.E.; Bawendi, M.G.; Bulović, V. Inkjet-Printed Quantum Dot-Polymer Composites for Full-Color AC-Driven Displays. *Adv. Mater.* **2009**, *21*, 2151–2155.
6. Bao, B.; Jiang, J.; Li, F.; Zhang, P.; Chen, S.; Yang, Q.; Wang, S.; Su, B.; Jiang, L.; Song, Y. Fabrication of Patterned Concave Microstructures by Inkjet Imprinting. *Adv. Funct. Mater.* **2015**, *25*, 3286–3294.

7. Ren, L.; Zhuang, J.; Casillas, G.; Feng, H.; Liu, Y.; Xu, X.; Liu, Y.; Chen, J.; Du, Y.; Jiang, L.; et al. Nanodroplets for Stretchable Superconducting Circuits. *Adv. Funct. Mater.* **2016**, *26*, 8111–8118.
8. Lee, S.; Shin, S.; Lee, S.; Seo, J.; Lee, J.; Son, S.; Cho, H.J.; Algadi, H.; Al-Sayari, S.; Kim, D.E.; et al. Ag Nanowire Reinforced Highly Stretchable Conductive Fibers for Wearable Electronics. *Adv. Funct. Mater.* **2015**, *25*, 3114–3121.
9. Zhou, L.; Yu, M.; Chen, X.; Nie, S.; Lai, W.-Y.; Su, W.; Cui, Z.; Huang, W. Ito-Free Flexible Electronics: Screen-Printed Poly(3,4-Ethylenedioxythiophene):Poly(Styrenesulfonate) Grids as ITO-Free Anodes for Flexible Organic Light-Emitting Diodes (Adv. Funct. Mater. 11/2018). *Adv. Funct. Mater.* **2018**, *28*, 1870072.
10. Majee, S.; Song, M.; Zhang, S.; Zhang, Z. Scalable inkjet printing of shear-exfoliated graphene transparent conductive films. *Carbon N. Y.* **2016**, *102*, 51–57.
11. Liang, Y.T.; Hersam, M.C. Highly Concentrated Graphene Solutions via Polymer Enhanced Solvent Exfoliation and Iterative Solvent Exchange. *J. Am. Chem. Soc.* **2010**, *132*, 17661–17663.
12. Li, W.; Wu, W.; Li, Z. Controlling Interlayer Spacing of Graphene Oxide Membranes by External Pressure Regulation. *ACS Nano* **2018**, *12*, 9309–9317.
13. Sechi, D.; Greer, B.; Johnson, J.; Hashemi, N. Three-dimensional paper-based microfluidic device for assays of protein and glucose in urine. *Analytical chemistry.* **2013**, *85*(22), 10733–10737.
14. Huang, L.; Huang, Y.; Liang, J.; Wan, X.; Chen, Y. Graphene-based conducting inks for direct inkjet printing of flexible conductive patterns and their applications in electric circuits and chemical sensors. *Nano Res.* **2011**, *4*, 675–684.
15. Novoselov, K.S.; Jiang, D.; Schedin, F.; Booth, T.J.; Khotkevich, V. V; Morozov, S. V; Geim, A.K. Two-dimensional atomic crystals. *Proc. Natl. Acad. Sci. U. S. A.* **2005**, *102*, 10451–3.
16. Sharifi, F.; Patel, B.B.; Dzuilko, A.K.; Montazami, R.; Sakaguchi, D.S.; Hashemi, N.; Polycaprolactone microfibrillar scaffolds to navigate neural stem cells. *Biomacromolecules.* **2016** *17*(10), 3287–3297.
17. Sharifi, F.; Patel, B.B.; McNamara, M.C.; Meis, P.J.; Roghair, M.N.; Lu, M.; Montazami, R.; Sakaguchi, D.S.; Hashemi, N.N. Photo-cross-Linked Poly (ethylene glycol) Diacrylate Hydrogels: Spherical Microparticles to Bow Tie-shaped Microfibers. *ACS applied materials & interfaces.* **2019**.
18. Bai, Z.; Reyes, J.M.M.; Montazami, R.; Hashemi, N.N. On-chip development of hydrogel microfibers from round to square/ribbon shape. *Journal of Materials Chemistry A.* **2014**, *2*(14), 4878–4884.
19. Dimiev, A.; Kosynkin, D. V; Alemany, L.B.; Chaguine, P.; Tour, J.M. Pristine Graphite Oxide. **2012**.
20. Bagri, A.; Mattevi, C.; Acik, M.; Chabal, Y.J.; Chhowalla, M.; Shenoy, V.B. Structural evolution during the reduction of chemically derived graphene oxide. *Nat. Chem.* **2010**, *2*, 581–587.

21. Kauling, A.P.; Seefeldt, A.T.; Pisoni, D.P.; Pradeep, R.C.; Bentini, R.; Oliveira, R.V.B.; Novoselov, K.S.; Castro Neto, A.H. The Worldwide Graphene Flake Production. *Adv. Mater.* **2018**, *30*, 1–6.
22. Zhou, L.; Fox, L.; Włodek, M.; Islas, L.; Slastanova, A.; Robles, E.; Bikondoa, O.; Harniman, R.; Fox, N.; Cattelan, M.; et al. Surface structure of few layer graphene. *Carbon N. Y.* **2018**, *136*, 255–261.
23. Hashemi, N.; Lackore, J.M.; Sharifi, F.; Goodrich, P.J.; Winchell, M.L.; Hashemi, N. A paper-based microbial fuel cell operating under continuous flow condition. *Technology.* **2016**, *4*(02), 98-103.
24. Acar, H.; Çınar, S.; Thunga, M.; Kessler, M.R.; Hashemi, N.; Montazami, R. Study of physically transient insulating materials as a potential platform for transient electronics and bioelectronics. *Advanced Functional Materials.* **2014**, *24*(26), 4135-4143..
25. Gao, Y.; Shi, W.; Wang, W.; Leng, Y.; Zhao, Y. Inkjet printing patterns of highly conductive pristine graphene on flexible substrates. *Ind. Eng. Chem. Res.* **2014**, *53*, 16777–16784.
26. Pemathilaka, R.L.; Caplin, J.D.; Aykar, S.S.; Montazami, R.; Hashemi, N.N. Placenta-on-a-Chip: In Vitro Study of Caffeine Transport across Placental Barrier Using Liquid Chromatography Mass Spectrometry. *Global Challenges.* **2019**, *3*(3), 1800112.
27. Caplin, J.D.; Granados, N.G.; James, M.R.; Montazami, R.; Hashemi, N. Microfluidic organ-on-a-chip technology for advancement of drug development and toxicology. *Advanced healthcare materials.* **2015**, *4*(10), 1426-1450.
28. Hernandez, Y.; Nicolosi, V.; Lotya, M.; Blighe, F.M.; Sun, Z.; De, S.; McGovern, I.T.; Holland, B.; Byrne, M.; Gun'Ko, Y.K.; et al. High-yield production of graphene by liquid-phase exfoliation of graphite. *Nat. Nanotechnol.* **2008**, *3*, 563–568.
29. Lotya, M.; Hernandez, Y.; King, P.J.; Smith, R.J.; Nicolosi, V.; Karlsson, L.S.; Blighe, F.M.; De, S.; Wang, Z.; McGovern, I.T.; et al. Liquid Phase Production of Graphene by Exfoliation of Graphite in Surfactant/Water Solutions. *J. Am. Chem. Soc.* **2009**, *131*, 3611–3620.
30. Vallés, C.; Drummond, C.; Saadaoui, H.; Furtado, C.A.; He, M.; Roubeau, O.; Ortolani, L.; Monthieux, M.; Pénicaud, A. Solutions of Negatively Charged Graphene Sheets and Ribbons. *J. Am. Chem. Soc.* **2008**, *130*, 15802–15804.
31. Torrisi, F.; Hasan, T.; Wu, W.; Sun, Z.; Lombardo, A.; Kulmala, T.S.; Hsieh, G.W.; Jung, S.; Bonaccorso, F.; Paul, P.J.; et al. Inkjet-printed graphene electronics. *ACS Nano* **2012**, *6*, 2992–3006.
32. Li, J.; Ye, F.; Vaziri, S.; Muhammed, M.; Lemme, M.C.; Östling, M. Efficient inkjet printing of graphene. *Adv. Mater.* **2013**, *25*, 3985–3992.
33. Cha, C.; Shin, S.R.; Annabi, N.; Dokmeci, M.R.; Khademhosseini, A. Carbon-Based Nanomaterials: Multifunctional Materials for Biomedical Engineering. *ACS Nano* **2013**, *7*, 2891–2897.

34. Pampaloni, N.P.; Lottner, M.; Giugliano, M.; Matruglio, A.; D'Amico, F.; Prato, M.; Garrido, J.A.; Ballerini, L.; Scaini, D. Single-layer graphene modulates neuronal communication and augments membrane ion currents. *Nat. Nanotechnol.* **2018**, *13*, 755–764.
35. Rivnay, J.; Wang, H.; Fenno, L.; Deisseroth, K.; Malliaras, G.G. Next-generation probes, particles, and proteins for neural interfacing. *Sci. Adv.* **2017**, *3*, e1601649.
36. Li, D.; Kaner, R.B. Graphene-Based Materials Is Mars Geodynamically Dead ? **2008**, *320*, 1170–1172.
37. Pattammattel, A.; Kumar, C.V. Kitchen Chemistry 101: Multigram Production of High Quality Biographene in a Blender with Edible Proteins. *Adv. Funct. Mater.* **2015**, *25*, 7088–7098.
38. Ahadian, S.; Estili, M.; Surya, V.J.; Ramón-Azcón, J.; Liang, X.; Shiku, H.; Ramalingam, M.; Matsue, T.; Sakka, Y.; Bae, H.; et al. Facile and green production of aqueous graphene dispersions for biomedical applications. *Nanoscale* **2015**, *7*, 6436–6443.
39. Li, X.; Wang, X.; Zhang, L.; Lee, S.; Dai, H. Chemically derived, ultrasmooth graphene nanoribbon semiconductors. *Science* **2008**, *319*, 1229–32.
40. Rubio, N.; Fabbro, C.; Herrero, M.A.; De La Hoz, A.; Meneghetti, M.; Fierro, J.L.G.; Prato, M.; Vázquez, E. Ball-milling modification of single-walled carbon nanotubes: Purification, cutting, and functionalization. *Small* **2011**, *7*, 665–674.
41. León, V.; Quintana, M.; Herrero, M.A.; Fierro, J.L.G.; Hoz, A.D. La; Prato, M.; Vázquez, E. Few-layer graphenes from ball-milling of graphite with melamine. *Chem. Commun.* **2011**, *47*, 10936–10938.
42. Zhao, W.; Fang, M.; Wu, F.; Wu, H.; Wang, L.; Chen, G. Preparation of graphene by exfoliation of graphite using wet ball milling. *J. Mater. Chem.* **2010**, *20*, 5817.
43. Shin, K.-Y.; Hong, J.-Y.; Jang, J. Micropatterning of Graphene Sheets by Inkjet Printing and Its Wideband Dipole-Antenna Application. *Adv. Mater.* **2011**, *23*, 2113–2118.
44. Choi, J.; Kim, Y.J.; Lee, S.; Son, S.U.; Ko, H.S.; Nguyen, V.D.; Byun, D. Drop-on-demand printing of conductive ink by electrostatic field induced inkjet head. *Appl. Phys. Lett.* **2008**, *93*, 2006–2009.
45. Guo; Niaraki Asli; Williams; Lai; Wang; Montazami; Hashemi Viability of Neural Cells on 3D Printed Graphene Bioelectronics. *Biosensors* **2019**, *9*, 112.
46. Paton, K.R.; Varrla, E.; Backes, C.; Smith, R.J.; Khan, U.; O'Neill, A.; Boland, C.; Lotya, M.; Istrate, O.M.; King, P.; et al. Scalable production of large quantities of defect-free few-layer graphene by shear exfoliation in liquids. *Nat. Mater.* **2014**, *13*, 624–630.
47. Nollet, L.M.L.; Toldra, F.; Toldra, F. *Handbook of Analysis of Edible Animal By-Products*; Nollet, L.M.L., Toldra, F., Eds.; CRC Press, 2011; ISBN 9780429166051.
48. Sreeprasad, T.S.; Berry, V. How do the electrical properties of graphene change with its functionalization? *Small* **2013**, *9*, 341–350.

49. Eckmann, A.; Felten, A.; Mishchenko, A.; Britnell, L.; Krupke, R.; Novoselov, K.S.; Casiraghi, C. Probing the Nature of Defects in Graphene by Raman Spectroscopy. *Nano Lett.* **2012**, *12*, 3925–3930.
50. Childres, I.; Jauregui, L.A.; Park, W.; Cao, H.; Chen, Y.P. Raman Spectroscopy of Graphene and. *Dev. Phot. Mater. Res.* **2013**, *1*, 31–70.
51. Ahadian, S.; Estili, M.; Surya, V.J.; Ramón-Azcón, J.; Liang, X.; Shiku, H.; Ramalingam, M.; Matsue, T.; Sakka, Y.; Bae, H.; et al. Facile and green production of aqueous graphene dispersions for biomedical applications. *Nanoscale* **2015**, *7*, 6436–6443.
52. Secor, E.B.; Ahn, B.Y.; Gao, T.Z.; Lewis, J.A.; Hersam, M.C. Rapid and Versatile Photonic Annealing of Graphene Inks for Flexible Printed Electronics. *Adv. Mater.* **2015**, *27*, 6683–6688.
53. Wong, C.H.A.; Sofer, Z.; Kubešová, M.; Kučera, J.; Matějková, S.; Pumera, M. Synthetic routes contaminate graphene materials with a whole spectrum of unanticipated metallic elements. *Proc. Natl. Acad. Sci. U. S. A.* **2014**, *111*, 13774–9.
54. Huang, Z.; Chen, H.; Huang, Y.; Ge, Z.; Zhou, Y.; Yang, Y.; Xiao, P.; Liang, J.; Zhang, T.; Shi, Q.; et al. Ultra-Broadband Wide-Angle Terahertz Absorption Properties of 3D Graphene Foam. *Adv. Funct. Mater.* **2018**, *28*, 1704363.
55. Majee, S.; Song, M.; Zhang, S.-L.; Zhang, Z.-B. Scalable inkjet printing of shear-exfoliated graphene transparent conductive films. *Carbon N. Y.* **2016**, *102*, 51–57.
56. Das, S.R.; Nian, Q.; Cargill, A.A.; Hondred, J.A.; Ding, S.; Saei, M.; Cheng, G.J.; Claussen, J.C. 3D nanostructured inkjet printed graphene: Via UV-pulsed laser irradiation enables paper-based electronics and electrochemical devices. *Nanoscale* **2016**, *8*, 15870–15879.
57. Secor, E.B.; Prabhumirashi, P.L.; Puntambekar, K.; Geier, M.L.; Hersam, M.C. Inkjet Printing of High Conductivity, Flexible Graphene Patterns. *J. Phys. Chem. Lett.* **2013**, *4*, 1347–1351.
58. Zobeiri, H.; Wang, R.; Deng, C.; Zhang, Q.; Wang, X. Polarized Raman of Nanoscale Two-Dimensional Materials: Combined Optical and Structural Effects. *J. Phys. Chem. C* **2019**, *123*, 23236–23245.
59. Secor, E.B.; Ahn, B.Y.; Gao, T.Z.; Lewis, J.A.; Hersam, M.C. Rapid and Versatile Photonic Annealing of Graphene Inks for Flexible Printed Electronics. *Adv. Mater.* **2015**, *27*, 6683–6688.
60. Hondred, J.A.; Stromberg, L.R.; Mosher, C.L.; Claussen, J.C. High-Resolution Graphene Films for Electrochemical Sensing via Inkjet Maskless Lithography. *ACS Nano* **2017**, *11*, 9836–9845.
61. Derby, B.; Reis, N. Inkjet Printing of Highly Loaded Particulate Suspensions. *MRS Bull.* **2003**, *28*, 815–818.
62. Leon, V.; Rodriguez, A.M.; Prieto, P.; Prato, M.; Vazquez, E. Exfoliation of graphite with triazine derivatives under ball-milling conditions: preparation of few-layer graphene via selective noncovalent interactions. *ACS nano.* **2014**, *8*(1), 563–571.
63. Jeon, I.Y.; Shin, Y.R.; Sohn, G.J.; Choi, H.J.; Bae, S.Y.; Mahmood, J.; Jung, S.M.; Seo, J.M.; Kim, M.J.; Chang, D.W.; Dai, L.; Edge-carboxylated graphene nanosheets via ball milling. *Proceedings of the National Academy of Sciences.* **2012**, *109*(15), 5588–5593.

64. Weiss, I.M.; Muth, C.; Drumm, R; Kirchner, H.O.; Thermal decomposition of the amino acids glycine, cysteine, aspartic acid, asparagine, glutamic acid, glutamine, arginine and histidine. *BMC biophysics*. **2018**, 11(1), 2.

## CHAPTER 3. VIABILITY OF NEURAL CELLS ON 3D PRINTED GRAPHENE BIOELECTRONICS

Modified from a manuscript with the same name published in Biosensors.

*Jingshuai Guo*<sup>1,†</sup>, *Amir Ehsan Niaraki Asli*<sup>1,†</sup>, *Kelli R. Williams*<sup>1</sup>, *Pei Lun Lai*<sup>1</sup>, *Xinwei Wang*<sup>1</sup>, *Reza Montazami*<sup>1</sup> and *Nicole N. Hashemi*<sup>1,2,\*</sup>

<sup>1</sup> Department of Mechanical Engineering, Iowa State University, Ames, IA 50011, USA;

<sup>2</sup> Department of Biomedical Engineering, Iowa State University, Ames, IA 50011, USA

\* Correspondence: nastaran@iastate.edu

† These Authors contributed equally to this work.

### Abstract

Parkinson's disease (PD) is the second most common neurodegenerative disease in the United States after Alzheimer's disease (AD). To help understand the electrophysiology of these diseases, N27 neuronal cells have been used as an in vitro model. In this study, a flexible graphene-based biosensor design is presented. Biocompatible graphene was manufactured using a liquid-phase exfoliation method and bovine serum albumin (BSA) for further exfoliation. Raman spectroscopy results indicated that the graphene produced was indeed few-layer graphene (FLG) with  $(I_D/I_G)_{Graphene} = 0.11$ . Inkjet printing of this few-layer graphene ink onto Kapton polyimide (PI) followed by characterization via scanning electron microscopy (SEM) showed an average width of  $\approx 868 \mu\text{m}$  with a normal thickness of  $\approx 5.20 \mu\text{m}$ . Neuronal cells were placed on a thermally annealed 3D printed graphene chip. A live–dead cell assay was performed to prove the biosensor biocompatibility. A cell viability of approximately 80% was observed over 96 h, which indicates that annealed graphene on Kapton PI substrate could be used as a neuronal cell biosensor. This research will help us move forward with the study of N27 cell electrophysiology and electrical signaling.

### 3.1 Introduction

Parkinson's disease (PD) is a neuronal disease that is caused by the death of dopaminergic neurons in the substantia nigra pars compacta region of the brain [1]. It is currently the second most common neurodegenerative disease in the United States after Alzheimer's disease (AD) [1,2]. Because

of their dopaminergic properties [1], rat dopaminergic N27 cells have been widely used in in vitro models for PD studies [1,3]. They have also been used in studies seeking to understand problems such as neurotoxicity, oxidative stress, and histone deacetylase (HDAC) and other molecular pathways [4–6]. While there have been studies on synaptophysin signaling in N27 cells, the electrophysiological effects of graphene on N27 cells are currently unknown. Since a study on the electrophysiology of N27 cells is necessary to further understand PD and other neurodegenerative diseases, graphene may be helpful to better understand neurodegenerative diseases when employed as a biosensor.

Graphene is among the most widely used materials in the field of material science [7,8].

Graphene has a two-dimensional honeycomb nanostructure with a one-atom-thick planar sheet of  $sp^2$ -bonded carbon atoms [8–10]. Graphene has a large theoretical specific surface area of  $2630 \text{ m}^2 \text{ g}^{-1}$  [11,12], intrinsic mobility of  $200,000 \text{ cm}^2 \text{ v}^{-1} \text{ s}^{-1}$  [13], and a superior thermal conductivity of approximately  $5000 \text{ W m}^{-1} \text{ K}^{-1}$  [14]. Since it also has excellent electrical conductivity, it lends itself to many real-world applications and provides an ideal foundation for bioelectronics and biosensing [15,16].

Although there are currently many methods used to produce graphene, the end products are not biocompatible [17–19]. For example, popular graphene solutions such as dimethylformamide (DMF) and N-methylpyrrolidone (NMP) solutions are toxic and often result in low-concentration graphene solutions [20,21]. Therefore, it is necessary to develop a cell-friendly approach for large-scale production of biocompatible graphene. To address this problem, research was conducted on the synthesis of graphene-based solutions via oxidation and chemical vapor deposition (CVD) with the intent of improving these graphene fabrication methods [22–25]. However, there is evidence showing that the Hummer's method creates single carbon atom defects along with nano-sized cracks [26]. CVD works well for producing large, continuous films of graphene, but this method has been shown to result in numerous surface voids and defects [27], and its application has been only partly successful [28]. As the research of biocompatible graphene and its implementation in practical applications such as printing

graphene have continued to grow, very few studies have been able to produce satisfying results [21]. Fortunately, the method of direct liquid-phase exfoliation (LPE) of graphite into graphene has been reported as an attractive approach for inkjet printing and cell-based studies.

There have been many previous studies on constructing biosensors using graphene-based materials [29]. One such example involved using graphene oxide (GO) to examine cellular DNA via the creation of graphene quantum dots (GQDs) [30]. The biosensors in another study primarily focused on the transfer of electrons and used CV to image cancer stem cells [31]. Also, while  $[\text{Fe}(\text{CN})_6]^{3-/4-}$  and  $[\text{Ru}(\text{NH}_3)_6]^{3+/2+}$  redox peaks have been measured, a study on the bioelectrical signaling of neuronal cells using graphene-based sensors is lacking [30–33]. One advantage of using graphene in a biosensor study is that this material has no effect on mitochondrial membrane potential (MMP), mitochondrial morphology, or cell stress status [34]. Since graphene appears to have a bright future in biochemical and biomedical applications, engineers are encouraged to continue research studies on this material [34–37].

In this study, we describe a prototype graphene biosensor to sense electrical signaling in N27 cells. The biosensor was produced with an inkjet printer to create conductive, biocompatible, and defect-free graphene. The graphene was exfoliated from graphite using the LPE method. This design presents a facile technique that can be used to manufacture biosensors for a variety of applications. In a previous study, bovine serum albumin (BSA) was used to exfoliate graphene in an aqueous state and resulted in graphene that exhibited strong biocompatibility. Since this technique was easily implemented, it resulted suitable for large-scale graphene production and, hence, was adopted in this study. The graphene and printed graphene chips were characterized using Raman spectroscopy, Atomic force microscopy (AFM), and scanning electron microscopy (SEM). To characterize cell viability within the biosensor, multiple live–dead cell assays were performed.

### **3.2 Materials and Experimental Section**

The materials and equipment used in this study were: graphite (Synthetic powder, <20  $\mu\text{m}$ , Sigma-Aldrich, St. Louis, MO, USA); Albumin, from bovine serum (bovine albumin\* BSA,  $\geq 98\%$

agarose gel electrophoresis, lyophilized powder, Sigma-Aldrich, St. Louis, MO, USA); poly(sodium 4-styrenesulfonate) (PSS, Mw ~1,000,000 powder, Sigma-Aldrich, St. Louis, MO, USA); poly(ethyleneimine), (PEI) solution (50% w/v, Sigma-Aldrich, St. Louis, MO, USA); sodium chloride (NaCl) purchased from Sigma-Aldrich, St. Louis, MO, USA; Kapton polyimide (PI) (thickness: 0.008 mm, 100 × 100 mm, Sigma-Aldrich, St. Louis, MO, USA). RPMI medium 1640 (1X) (Ref#: 11875-093, 500 mL), L-glutamine 200 mM(100X) (Ref#: 25030-081, 100 mL), pen/strep solution (penicillin 10,000 U mL<sup>-1</sup>/streptomycin 10,000 µg mL<sup>-1</sup>, Ref#: 15140-122, 100 mL) was purchased from Gibco Life Technologies. Fetal bovine serum (FBS) (Qualified One Shot™, Ref#: A31606-01, 50 mL) was purchased from ThermoFisher Scientific, Waltham, MA. Polyurethane ether tubes (I.D.:0.063", Wall:0.031", O.D.:0.125", Part Number: 2100070-100) were purchased from Superthane®, 3 mL Luer-Lok syringes were purchased from Allegro Medical. Inc. (Bolingbrook, IL, USA) Six-well cell culture clusters (Lot# 23314037) were purchased from Costar®. A GenieTouch™, syringe pump was purchased from Kent Scientific Corporation. A 4-axis CNC USB controller Mk3/4 for mini CNC mill was purchased and controlled by a PlanetCNC® (Ljubljana, Slovenia). A sinometer digital multimeter (MS8261) was used to measure print conductivity. A JEOL FESM JCM-6000 scanning electron microscope and a Zeiss Axio Observer Z1 inverted microscope were used for SEM imaging of the graphene prints and the live–dead cell assays, respectively. A Raman spectrometer (Voyage, B&W Tek, Inc., Newark, DE, USA) with a CW laser (Excelsior-532-150-CDRH, Spectra-Physics) was used for Raman spectroscopy measurements. A PerkinElmer UV–Vis spectrophotometer (Lambda 750) at  $\lambda = 660$  nm at room temperature was used to provide absorption spectra and consequently the concentration of graphene ink.

### 3.2.1 Preparation of Graphene

The graphene solution used in this study was produced using the liquid exfoliation method. Wet-ball milling was used with both the Vibrio-Energy shaker mill [38] and a kitchen blender for further exfoliation [8]. The preparation of graphene, ink formulation and finally inkjet printing of the produced

conductive ink is illustrated in Figure 1. The shear tension created by the steel balls helped further the exfoliation of graphene crystallites and led to the fabrication of high-quality FLG [38–40]. When using the Vibro-Energy (shaker) mill, 650 mg of graphite was mixed with 60 mg of BSA and was well dispersed in 35 mL of DI-H<sub>2</sub>O. The Vibro-Energy mill (shaker mill) was run for 90 h at 300 rpm (Figure 1B). Twenty steel balls with a diameter of 8.7 mm (11/32”) and 10 steel balls with a diameter of 4.5 mm (3/16”) were added to all 5 containers (Figure 2A). A standard kitchen blender was run for 1 h at a speed of 16,761 rpm. Twenty grams of graphite was mixed with 605 mg of BSA well dispersed in 100 mL of DI-H<sub>2</sub>O. Both graphene solutions were kept at rest for 24 h, allowing any remnant of non-dispersed graphite particles to sink to the bottom of the containers. Finally, in order to ensure repeatability of the formulated ink, the samples were collected from the top 80% of the solution, and the concentration of graphene was measured through UV–Vis spectroscopy. The resultant concentration resulted to be  $C \approx 5.1 \text{ mg mL}^{-1}$ .

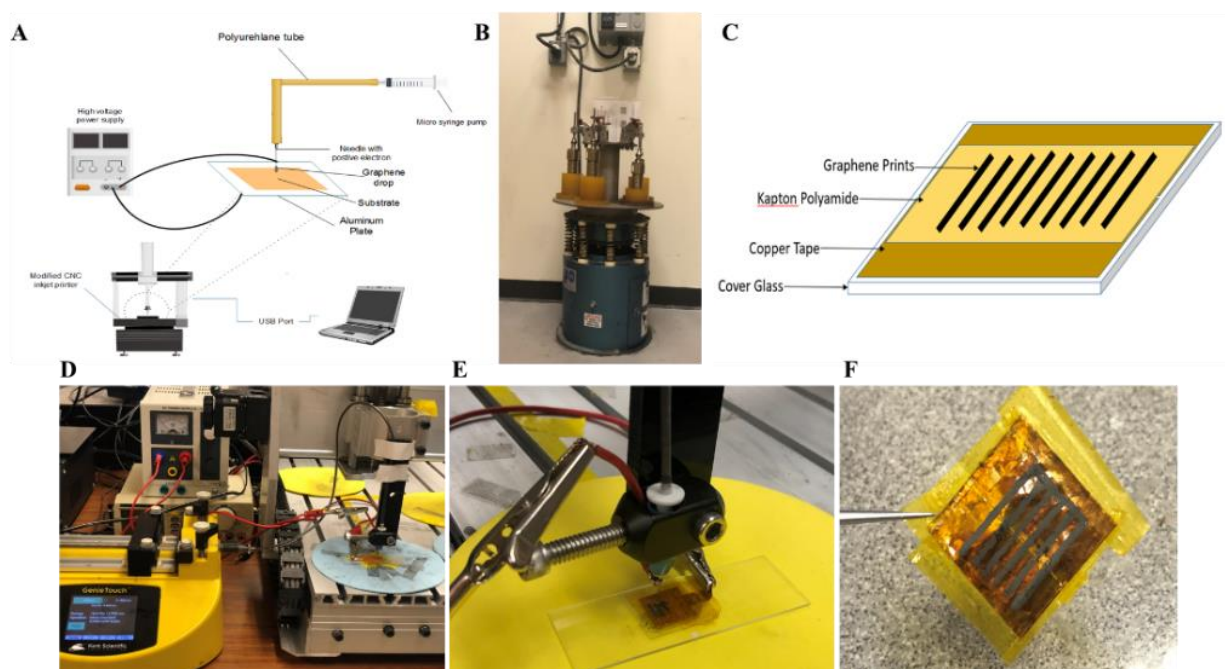


*Figure 0.1 Schematic of the drop-on-demand graphene printing method. (A) An abridged general view of the printer setup. (B) A graphene solution was mixed using a Vibro-Energy mill (shaker mill) for 90 h at 300 rpm. (C) Schematic of chip setup. (D) Equipment setup during printing. A syringe pump was used along with an inkjet printer to deposit ink at a rate of  $7 \mu\text{L/s}$  to ensure a constant flow rate throughout the syringe. (E) Needle and substrate setup. A 3 kV potential difference was introduced between the substrate and needle for the purpose of affixing ink onto the substrate. A cover glass was placed on a regular microscope slide for stability and support. (F). Printed chip end result of 3D printed graphene.*

Because of its great thermal resistance, Kapton PI was chosen as the polymer substrate. It can withstand temperatures from  $-269$  to  $400$  °C. Due to the hydrophilicity and negative charge of the FLG ink, it was necessary to perform a hydrophilicity treatment on the Kapton PI substrate. To treat Kapton PI, PI was first washed in acetone. The substrate was next washed with PSS (3.5 mg/mL), submerged in a solution of 50 mL DI-H<sub>2</sub>O and NaCl ( $0.5 \text{ mol L}^{-1}$ ), and finally submerged into a PEI solution (30 mg/mL) of DI-H<sub>2</sub>O and an NaCl solution ( $0.5 \text{ mol L}^{-1}$ ) for additional 20 min. The substrate was then allowed to air-dry for 12 h.

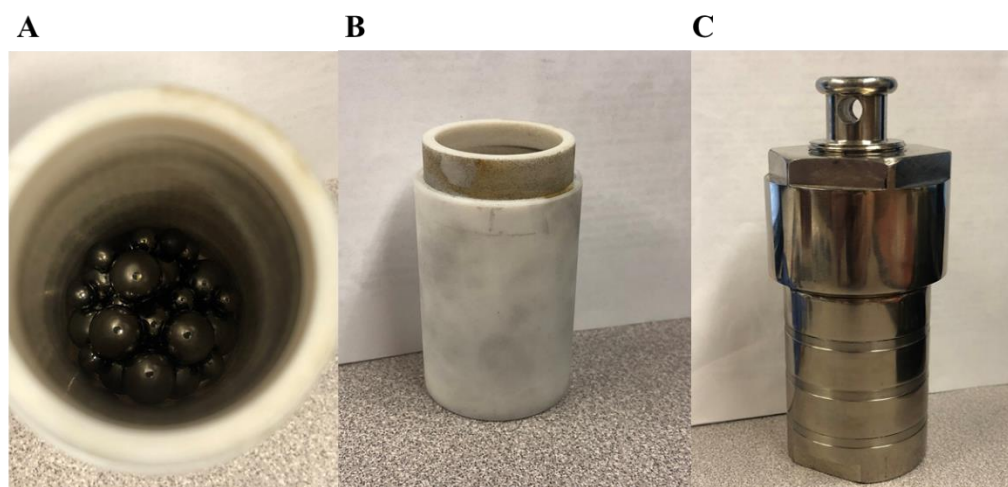


*Figure 0.2 Graphene wet-ball milling container setup. (A) Twenty steel balls with a diameter of 8.7 mm (11/32”) and 10 steel balls with a diameter of 4.5 mm (3/16”) were added. (B,C) Container assembly for shaker mill.*

### 3.2.2 Substrate Preparation

Because of its great thermal resistance, Kapton PI was chosen as the polymer substrate. It can withstand temperatures from  $-269$  to  $400$  °C. Due to the hydrophilicity and negative charge of the FLG ink, it was necessary to perform a hydrophilicity treatment on the Kapton PI substrate. To treat Kapton PI, PI was first washed in acetone. The substrate was next washed with PSS (3.5 mg/mL), submerged in a solution of 50 mL DI-H<sub>2</sub>O and NaCl ( $0.5 \text{ mol L}^{-1}$ ), and finally submerged into a PEI solution (30 mg/mL) of DI-H<sub>2</sub>O and an NaCl solution ( $0.5 \text{ mol L}^{-1}$ ) for additional 20 min. The substrate was then allowed to air-dry for 12 h.

### 3.2.3 Inkjet Printing Procedure

The graphene ink was placed in a 5 mL syringe, and a 10 cm-long polyurethane ether tube was attached to this syringe. The graphene ink was injected through a hypodermic needle with an inner diameter of 300  $\mu\text{m}$ . The syringe was fixed, and the graphene ink was injected via the syringe pump at a rate of 3  $\mu\text{L s}^{-1}$ . The ink was injected onto the PI substrate, which was fixed on a 22  $\times$  22 mm glass cover chip. The chip was covered with two pieces of copper tape, with a 0.50 mm gap between the two pieces (Figure 1C). A 3 kV potential difference was applied between the needle and the substrate, with the needle position being controlled by the CNC mini mill and its associated software. Prints were manufactured with a space of 800  $\mu\text{m}$  between each print, and a total of five graphene lines were printed on one chip. Figure 1F shows the final printing result after annealing. A total of six graphene chips were made during each printing session.

### 3.2.4 Post-Processing and Conductivity Testing

Post-processing was performed for the purpose of improving the electrical conductivity and the stability of the printed graphene [41,42]. A set temperature of 280  $^{\circ}\text{C}$  was used to anneal the inkjet-printed graphene. After 30 min of annealing, the graphene chips were gently placed in a clear six-well plate. All chips required sterilization before introducing the cells. This allowed the cells to grow and increased the chances of their survival. A digital multimeter was used for conductivity testing, and the resistance of each line was measured every 3 mm across the gap created on the chip. The width of each line was then measured using a SEM and found to be  $868 \pm 20 \mu\text{m}$ ; the height of each line measured by SEM was  $4 \pm 1 \mu\text{m}$ . The conductivity of each line could then be calculated from Equation (1), where  $R$  is the resistance of a printed line,  $l$  is its measured length,  $w$  is its width, and  $\sigma$  is the conductivity [43,44].

$$R = \frac{l}{wt\sigma} \quad (1)$$

Based on Equation (1), the conductivity measurements were performed by several trials with different annealing temperatures and different time periods. Figure 3 shows the conductivity changes along annealing time and temperature change.

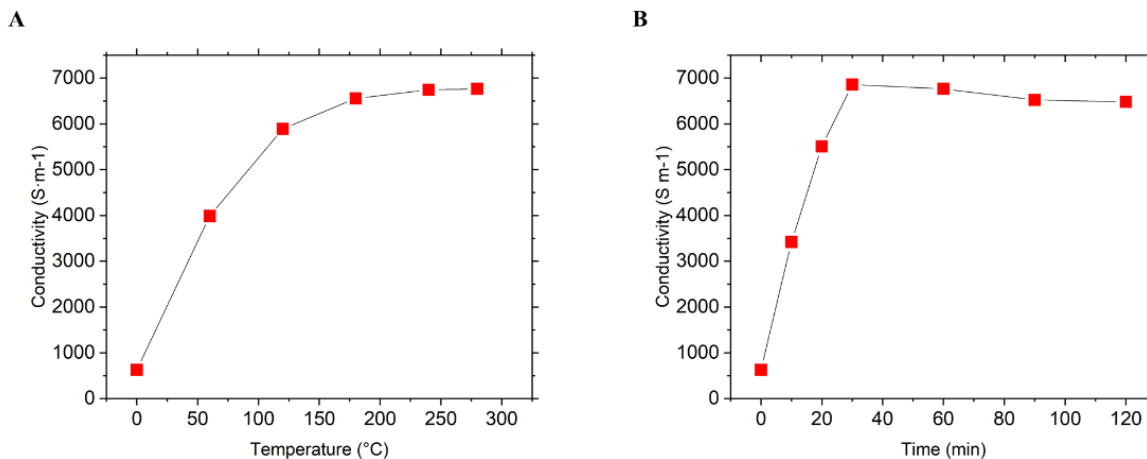


Figure 0.3 Conductivity measurements of printed graphene prints after treatment. (A) Conductivity changes dependent on the temperature, checked every 30 min. (B) Conductivity changes dependent on time at the same temperature of 280 °C.

### 3.2.5 Raman Spectroscopy

The samples obtained from the shaker mill and kitchen blender had similar cartelization when Raman spectroscopy was performed (Figure 4A). A thin film of graphene sample was prepared to determine the Raman spectra. A drop of the graphene sample with a diameter of approximately 10 mm was placed on top of a Si/SiO<sub>2</sub> substrate and air-dried. A Raman spectrometer with a CW laser provided a laser beam at wavelength 532 nm to the graphene on the Si/SiO<sub>2</sub> sample. Figure 4A depicts the Raman results for the graphene sample, on which five points were acquired by the Raman spectra. Figure 4B depicts the Raman results for the printed graphene lines on the Kapton substrate with comparisons of annealed graphene prints and non-annealed graphene prints.

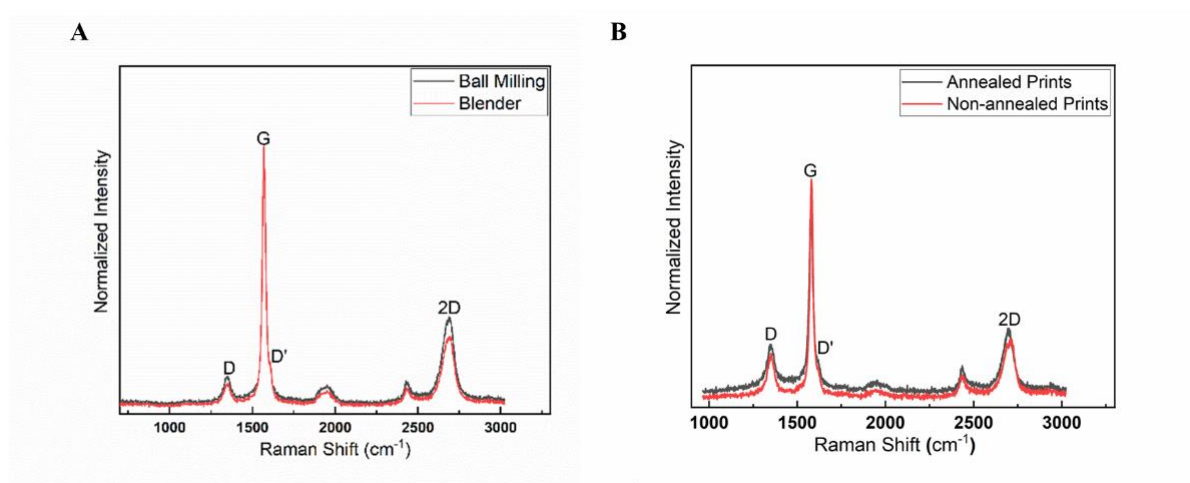


Figure 0.4 Raman spectra plot of both ball milling and blundered graphene under 532 nm laser. (A) Raman results for both ball milling and blender graphene samples on a Si/SiO<sub>2</sub> substrate. (B) Raman results for after annealed prints and non-annealed prints on Kapton tape.

### 3.2.6 Scanning Electron Microscopy and Atomic Force Microscopy

Imaging of the printed graphene patterns on PI was performed using a SEM with a 2–5 kV accelerating voltage. The thickness is shown in Figure 5 that displays images of prints after annealing. AFM was applied to the graphene samples to characterize their thickness (Figure 6). A drop of graphene ink was positioned on a silicon slide and was dried on a warm plate in vacuum chamber to ensure the precision of experiments,

### 3.2.7 Chip Biocompatibility Tests

A flask of eight-time-passaged N27 cells was chosen for testing the biocompatibility of the graphene sensor. The graphene chips were placed in six-well cell culture plates. The chips were then placed under a biological safety cabinet and exposed to UV radiation for 12 h. The UV exposure ensured that the chips were sterile and biocompatibility would be maximized. In this study, N27s cells were cultured in 3 mL of maintenance medium (MM) that included RPMI medium 1640 (1X), 10% FBS, 1% penicillin, and 1% L-glutamine. Then, 3 mL medium was introduced in each well which was covered with the graphene chip. N27 cells with a cell density  $\geq 1 \times 10^6$  cells/vial were added to the chips using a micro pipette; 10  $\mu$ L of cell suspension was introduced in each of the prints. The cells were left

to grow in an incubator maintained at 37 °C with 5% CO<sub>2</sub>. The cells were checked under an inverted microscope at 72 h, as shown in Figure 7.

### 3.2.8 Live–Dead Cell Assay

Live–dead cell assays were performed using a 70 μM CellTracker™ CMFDA solution combined with an 8 μM propidium iodide (PI) solution in FBS-free RPMI medium. The CellTracker™ CMFDA solution was prepared by dissolving 50 μg of CellTracker™ in 10.8 μL of dimethyl sulfoxide (DMSO). The PI was diluted from a stock provided by Invitrogen. The 70 μM CellTracker™ CMFDA solution and 80 μM PI solution were dissolved in FBS-free RPMI medium to reach the correct concentrations. Then, 1 mL of solution was prepared to facilitate the calculations and minimize the error. MM was carefully removed from the desired well of the 6-well plate. After removal, the well was rinsed with FBS-free RPMI medium (500 μL), 500 μL of dye was added to the well, and the cells were then incubated for 30 min at 37 °C in a 5% CO<sub>2</sub> atmosphere. The dye was then removed, and FBS-free RPMI medium was added to maintain moisture for sample imaging. N27 cells were imaged after 72 h of incubation. As shown in the control well (Figure 7A), live cells were colored in green, and dead cells were colored in red. Live and dead cells were also visible on the graphene chips. The chips were removed from the MM after incubation to ensure the cells were indeed growing on the chips and not on the well-plate surface, since the cells might have grown underneath the chips rather than on the chips. The chips were removed from the wells and transferred to clean wells with no MM.

A Zeiss Axio Observer Z1 inverted microscope was used to gather the live–dead cell assay results. The cells were carefully shielded from light after performing the live–dead cell assay so as to not affect the results. CellTracker™ CMFDA has an excitation of 492 nm and an emission of 517 nm. Propidium iodide has an excitation of 535 nm and an emission of 617 nm. The microscope was set to capture these wavelengths and image the fluorescence resulting from the live–dead cell assay. The results can be seen in Figure 7.

### 3.3 Results and Discussion

Traditional graphene-based biosensors are expensive and are still in a conceptual stage. One fabrication method consists in synthesizing graphene on a glass slip and etching SiO<sub>2</sub> with a Si/285 nm laser (34). Another fabrication method uses surface plasmon resonance to fabricate graphene on a gold sensor to achieve higher sensitivity than that of a traditional gold thin film SPR sensor [45].

#### 3.3.1 Chip Design

In our design, the graphene biosensor chip included three components: a glass coverslip, a copper tape, and a polyimide (Kapton) polymer substrate (Figure 1). The copper tape was fixed on both sides of the chip with a 0.5 mm gap and fully covered by Kapton PI (Figure 1B) to prevent any cellular exposure to copper. The chip may cause cytotoxic effects, and the goal was to minimize these effects [46]. Since the gap between the two pieces of copper tape was  $\leq 0.5$  mm, the Kapton PI substrate was used to connect the two pieces of tape with a flat surface. The effect of this gap on the 3D prints was negligible (Figure 1E) [47–49]. This design ensured that light could penetrate through the gap between the copper tape layers and reduced damage to the prints, offering an inexpensive physical method that is ready to use.

#### 3.3.2 Printing Processes and Microscopy Studies

Aqueous graphene was pre-prepared using the wet-ball milling technology as described previously [50]. This paper focuses on graphene printing and sensor preparation. Graphene ink was applied to Kapton PI, using the custom-designed electronic inkjet printer represented in Figure 1. Because the FLG ink is hydrophilic and negatively charged [51], the PI substrate required some surface modification before successful printing could take place. The substrate was separately submerged into two different wetting agents, PSS and PEI, producing a hydrophilic layer on PI. This process created a hydrophilic buffer layer and changed the substrate from hydrophobic to hydrophilic [52]. A review of the literature disclosed that traditional inkjet printing uses a commercial printer that does not support high-viscosity ink. This negatively affects the print quality [24,53]. In this setup, graphene ink was

directly injected using a needle and printed on a PI substrate. An electric field (Figure 1E) helped the ink fuse to the Kapton PI substrate. We found that printing at a flow rate of 3  $\mu\text{L}/\text{min}$ , using a needle with an inner diameter of 300  $\mu\text{m}$  and a 3 kV voltage, produced stable, continuous graphene prints with equal width and thickness (Figure 5A). The rather high value of the electric field was necessary to fix the conductive ink on the substrate [54].

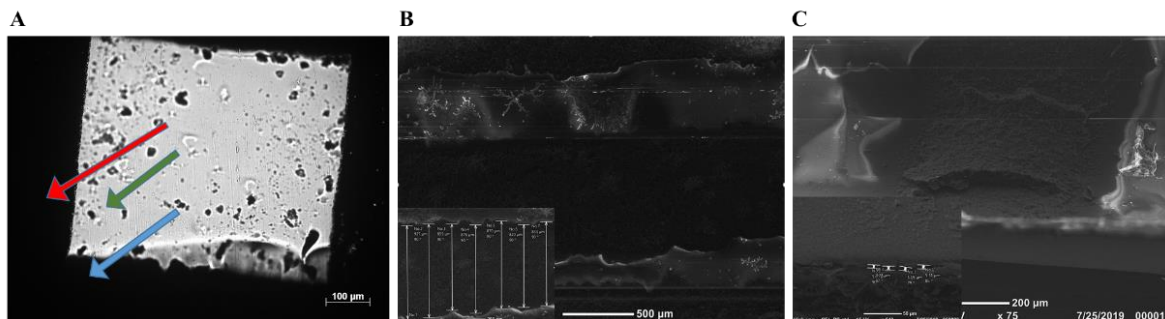


*Figure 0.5 Microscope image of printing results. (A) An area of prints under the microscope. The red, blue, and green arrows indicate graphene, copper tape, and polyimide (PI), respectively, after the annealing process. (B,C) SEM images of printed graphene on PI using 2–5 kV accelerated voltage. (B) is a top-view image taken using SEM after annealing the prints with an average width of  $\approx 868 \mu\text{m}$ . (C) shows an image of a cross section with an average depth of  $5.20 \mu\text{m}$ .*

To validate graphene quality, Raman spectroscopy of a graphene drop on  $\text{SiO}_2$  was performed using a laser with a wavelength of 532 nm (Figure 4). A couple of key points can be taken from the Raman characterization. The acquired spectrum experienced a sharp G peak at  $\sim 1569.19 \text{ cm}^{-1}$ , a symmetrical 2D peak at  $\sim 2689.55 \text{ cm}^{-1}$ , and a D peak at  $\sim 1348.33 \text{ cm}^{-1}$ , indicating that we had indeed achieved few-layer graphene [55]. Furthermore, the calculated  $(I_D/I_G)_{\text{Graphene}}$  of the blender-mixed graphene was 0.11, while that of the wet-ball milled graphene was found to be 0.16. To further characterize the printed graphene, a SEM was used to produce SEM images (Figure 5) that confirmed that the graphene prints had an average width of 868  $\mu\text{m}$  with no voids. This confirmed the purity of our graphene prints and that the graphene would be safe for biological use [56]. Additionally, The AFM results indicate a consistent thickness for the isolated graphene flake, which further confirms the Raman Spectra.

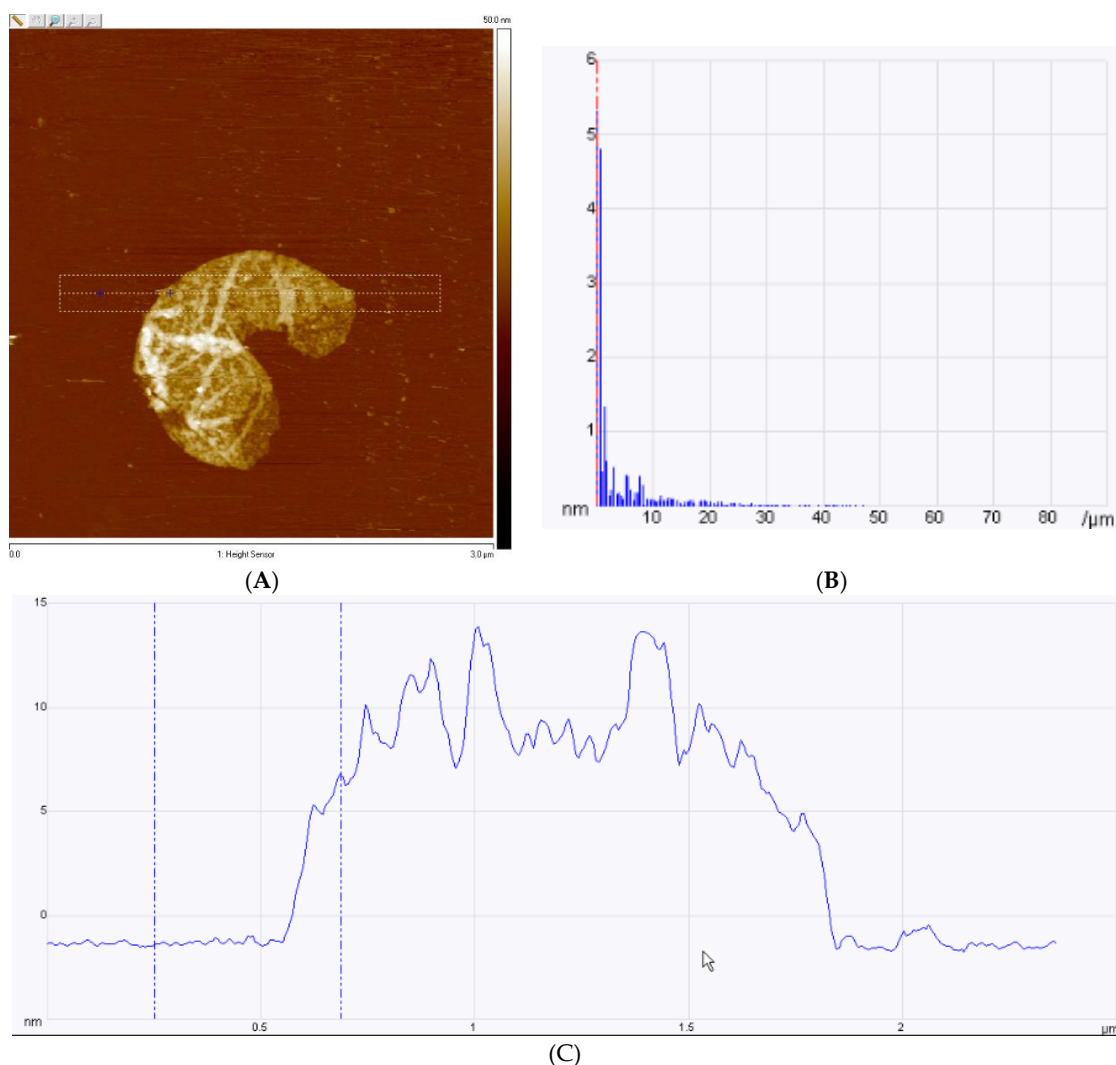


Figure 0.6 Atomic force microscopy (AFM) of graphene. (A) Graphene flake, (B) Spectral RMS amplitude was 5.33 nm. (C) AFM tapping frequency.

### 3.3.3 Post-Treatment of Graphene Prints

After undergoing the printing process, a thermal annealing process needed to be applied to complete the prints. This post-processing was necessary to prevent further disruption of the conductive network. The traditional solvents and surfactants used to perform graphite exfoliation can carry over into graphene production and may disrupt the conductive networks [21,44]. An oven was pre-heated to 280 °C to thermally treat the printed graphene. Graphene-printed chips were annealed for 30 min before being removed for conductivity measurements. Evidence shows that the properties of annealed graphene change as different annealing temperatures and times are applied [10,21,57–59]. The annealing process

helps minimize FLG flake-to-substrate defects, improves print resistance, and cleans off any polymer contaminants still present on the graphene surface [60–62].

Multiple conductivity measurements were taken using a multimeter. Resistance of all five printed lines was measured across the gap for every 1 mm. From measuring the line resistance, a conductivity measurement approximately at  $6800 \text{ S} \cdot \text{m}^{-1}$  was performed (Figure 3). By measuring in at different temperatures and different times, the changes in conductivity resulted negligible [63,64].

### **3.3.4 Biocompatibility Testing with N27 Cells**

First, 3 mL RPMI medium was added into each well, and a 50  $\mu\text{L}$  cell sample was added into the medium. N27 cells were observed under an inverted microscope after incubation for 24, 48, and 96 h. Figure 8 indicates the growth rate of the cells, demonstrating that after 72 h, the cells accounted for 85% of the live screen area. A live–dead cell assay was performed to confirm the survival rate of the cells grown on graphene [65,66]. It was expected that the cells would grow on top of the annealed Kapton and graphene. Polyimide materials are often used in biosensor research because of their strength and broad compatibility across research areas [67]. N27 cells fully expanded across the gap, connecting both sides of the graphene prints (Figure 7) [68,69]. From the live–dead cell assay results, it appeared that N27 cells successfully grew on the graphene and Kapton substrate, confirming our earlier hypothesis [69,70].

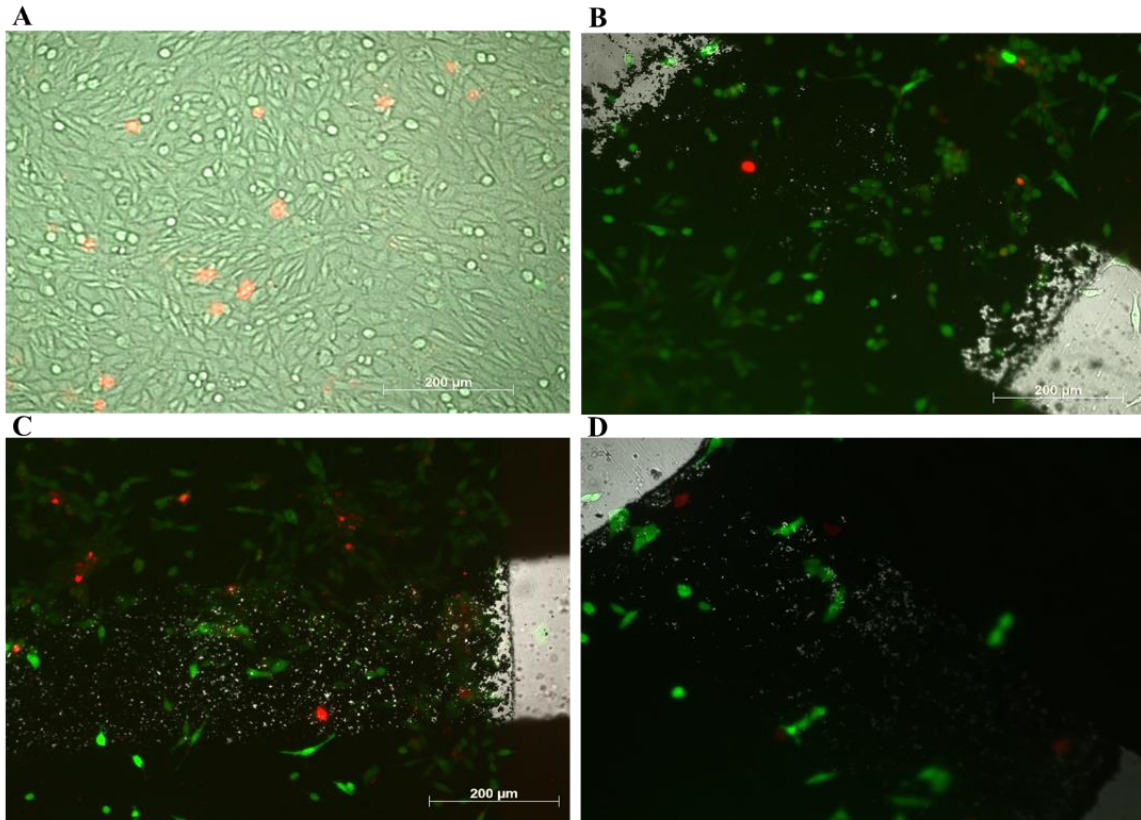


Figure 0.7 Cells cultured on graphene chips after 72 h of incubation. (A) Control well of N27 cells after 72 h at 37 °C in a 5% CO<sub>2</sub> atmosphere. (B–D) After 72 h of incubation, the cells expanded across a gap with a length of 290 μm.

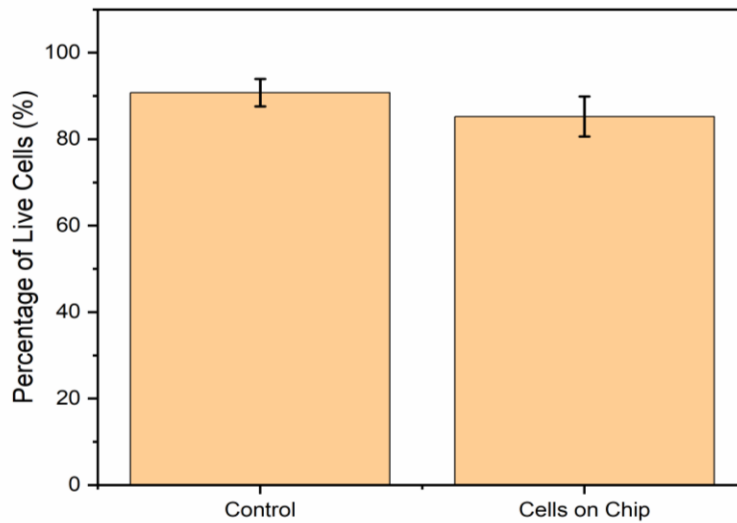


Figure 0.8 Percentage of live cells indicating that cell viability was approximately 85%.

It has been discussed in tissue-engineering literature that graphene may negatively affect the bimolecular mechanisms responsible for biological safety and toxicity [71–74]. Many reports have claimed that oxidative stress is one mechanism of cytotoxicity originating from carbon-based nanomaterials [75]. It is thought that graphene's sharp edges may cause cell membrane damage by physical interaction and lead to cytotoxicity [75–77]. Studies have also found evidence that graphene oxide is less toxic than graphene, while reduced graphene oxide and hydrogenated graphene solutions are much more toxic to neural cells. This may be due to the larger flake sizes present in these samples [72,78–81]. Such evidence provides support for our setup described above, in which there was no detectable cytotoxicity to the cells. Optical images also showed that only a small proportion of the cells were affected at the locations studied. These results could be beneficial for future N27 cell electrophysiology studies.

### 3.4 Conclusions

In conclusion, an easily applied and inexpensive biosensor design was presented characterized by a high percentage (85%) of live cells. This design could maximize printed FLG conductivity up to  $6800 \text{ S} \cdot \text{m}^{-1}$  after thermal annealing. On the basis of live–dead cell assays result, it also proved to be biocompatible and not to interfere with cell adhesion and neuronal cell proliferation. This design proved that pristine graphene after thermal treatment does not have a harmful effect on neuronal cells. In addition, graphene printed on Kapton PI exhibited no detectable adverse effects on cell multiplication, mitochondrial morphology, or cell stress (34). This highlights a promising future for graphene, including long-term and stable biomedical applications, especially in bioelectrical studies on N27 cell electrophysiology.

### References

1. Gao, L.; Zhou, W.; Symmes, B.; Freed, C.R. Re-Cloning the N27 Dopamine Cell Line to Improve a Cell Culture Model of Parkinson's Disease. *PLoS ONE* **2016**, *11*, e0160847.
2. Poewe, W.; Seppi, K.; Tanner, C.M.; Halliday, G.M.; Brundin, P.; Volkmann, J.; Schrag, A.E.; Lang, A.E.; Parkinson disease. *Nat. Rev. Dis. Primers* **2017**, *3*, 17013.

3. Jagatha, B.; Mythri, R.B.; Vali, S. Bharath MM. Curcumin treatment alleviates the effects of glutathione depletion in vitro and in vivo: therapeutic implications for Parkinson's disease explained via in silico studies. *Free Radic. Biol. Med.* **2008**, *44*, 907–917.
4. Harischandra, D.S.; Jin, H.; Anantharam, V.; Kanthasamy, A.; Kanthasamy, A.G.  $\alpha$ -Synuclein Protects Against Manganese Neurotoxic Insult During the Early Stages of Exposure in a Dopaminergic Cell Model of Parkinson's Disease. *Toxicol. Sci.* **2015**, *143*, 454–468.
5. Hammond, S.L.; Safe, S.; Tjalkens, R.B. A novel synthetic activator of Nurr1 induces dopaminergic gene expression and protects against 6-hydroxydopamine neurotoxicity in vitro. *Neurosci. Lett.* **2015**, *607*, 83–89.
6. Wang, Y.; Wang, X.; Liu, L.; Wang, X. HDAC inhibitor trichostatin A-inhibited survival of dopaminergic neuronal cells. *Neurosci. Lett.* **2009**, *467*, 212–216.
7. Geim, A.K.; Novoselov, K.S. The rise of graphene. In *Nanoscience and Technology*; Macmillan Publishers Ltd.: London, UK, 2009; p. 11–19.
8. Pattammattel, A.; Kumar CV. Kitchen Chemistry 101: Multigram Production of High Quality Biographene in a Blender with Edible Proteins. *Adv. Funct. Mater.* **2015**, *25*, 7088–7098.
9. Al-Sherbini AS, Bakr, M.; Ghoneim, I.; Saad, M. Exfoliation of graphene sheets via high energy wet milling of graphite in 2-ethylhexanol and kerosene. *J. Adv. Res.* **2017**, *8*, 209–215, doi:10.1016/j.jare.2017.01.004.
10. Gao, Y.; Shi, W.; Wang, W.; Leng, Y.; Zhao, Y. Inkjet printing patterns of highly conductive pristine graphene on flexible substrates. *Ind. Eng. Chem. Res.* **2014**, *53*, 16777–16784.
11. Du, J.; Cheng, H.-M. The Fabrication, Properties, and Uses of Graphene/Polymer Composites. *Macromol. Chem. Phys.* **2012**, *213*, 1060–1077, doi:10.1002/macp.201200029.
12. Bolotin, K.I.; Sikes, K.J.; Jiang, Z.; Klima, M.; Fudenberg, G.; Hone, J.; Kim, P.; Stormer, H.L. Ultrahigh electron mobility in suspended graphene. *Solid State Commun.* **2008**, *146*, 351–355.
13. Morozov, S.V.; Novoselov, K.S.; Katsnelson, M.I.; Schedin, F.; Elias, D.C.; Jaszczak, J.A.; Geim, A.K. Giant intrinsic carrier mobilities in graphene and its bilayer. *Phys. Rev. Lett.* **2008**, *100*, 11–14.
14. Teweldebrhan, D.; Lau, C.N.; Ghosh, S.; Balandin, A.A.; Bao, W.; Calizo, I.; Teweldebrhan, D.; Miao, F.; Lau, C.N. Superior Thermal Conductivity of Single-Layer Graphene. *Nano Lett.* **2008**, *8*, 902–907.
15. Cai, W.; Zhu, Y.; Li, X.; Piner, R.D.; Ruoff, R.S. Large area few-layer graphene/graphite films as transparent thin conducting electrodes. *Appl. Phys. Lett.* **2009**, *95*, 2007–2010.
16. Shao, Y.; Wang, J.; Wu, H.; Liu, J.; Aksay, I.A.; Lin, Y. Graphene based electrochemical sensors and biosensors: A review. *Electroanalysis* **2010**, *22*, 1027–1036.
17. Cheng, J.-S.; Du, J.; Zhu, W. Facile synthesis of three-dimensional chitosan–graphene mesostructures for reactive black 5 removal. *Carbohydr. Polym.* **2012**, *88*, 61–67.

18. Wang, L.; Wang, Y.; Xu, T.; Liao, H.; Yao, C.; Liu, Y.; Li, Z.; Chen, Z.; Pan, D.; Sun, L.; Wu, M. Gram-Scale Synthesis of Single-Crystalline Graphene Quantum Dots with Superior Optical Properties. **2014**, *5*, 5357.
19. Inamuddin, A.K.; Naushad, M. Optimization of glassy carbon electrode based graphene/ferritin/glucose oxidase bioanode for biofuel cell applications. *Int. J. Hydrogen Energy* **2014**, *39*, 7417–7421.
20. Zhao, W.; Fang, M.; Wu, F.; Wu, H.; Wang, L.; Chen, G. Preparation of graphene by exfoliation of graphite using wet ball milling. *J. Mater. Chem.* **2010**, *20*, 5817–5819.
21. Torrisi, F.; Hasan, T.; Wu, W.; Sun, Z.; Lombardo, A.; Kulmala, T.S.; Hsieh, G.W.; Jung, S.; Bonaccorso, F.; Paul, P.J. Inkjet-printed graphene electronics. *ACS Nano* **2012**, *6*, 2992–3006.
22. Hummers, W.S.; Offeman, R.E. *Preparation of Graphitic Oxide*; ACS Publications: Washington, DC, USA, 1958.
23. Zhang, L.; Li, X.; Huang, Y.; Ma, Y.; Wan, X.; Chen, Y. Controlled synthesis of few-layered graphene sheets on a large scale using chemical exfoliation. *Carbon N. Y.* **2010**, *48*, 2367–2371.
24. Huang, L.; Huang, Y.; Liang, J.; Wan, X.; Chen, Y. Graphene-based conducting inks for direct inkjet printing of flexible conductive patterns and their applications in electric circuits and chemical sensors. *Nano Res.* **2011**, *4*, 675–684.
25. Liang, Y.T.; Hersam, M.C. Highly Concentrated Graphene Solutions via Polymer Enhanced Solvent Exfoliation and Iterative Solvent Exchange. *J. Am. Chem. Soc.* **2010**, *132*, 17661–17663.
26. Dimiev, A.; Kosynkin, D.V.; Alemany, L.B.; Chaguine, P.; Tour, J.M. Pristine Graphite Oxide. *J. Am. Chem. Soc.* **2012**, *134*, 2815–2822.
27. Suk, J.W.; Kitt, A.; Magnuson, C.W.; Hao, Y.; Ahmed, S.; An, J.; Swan, A.K.; Goldberg, B.B.; Ruoff, R.S. Transfer of CVD-Grown Monolayer Graphene onto Arbitrary Substrates. *ACS Nano* **2011**, *5*, 6916–6924.
28. Kauling, A.P.; Seefeldt, A.T.; Pisoni, D.P.; Pradeep, R.C.; Bentini, R.; Oliveira, R.V.B.; Novoselov, K.S.; Castro Neto, A.H. The Worldwide Graphene Flake Production. *Adv. Mater.* **2018**, *30*, 1–6.
29. Kuila, T.; Bose, S.; Khanra, P.; Mishra, A.K.; Kim, N.H.; Lee, J.H. Recent advances in graphene-based biosensors. *Biosens. Bioelectron.* **2011**, *26*, pp. 4637–4648.
30. Zhou, M.; Zhai, Y.; Dong, S. Electrochemical Sensing and Biosensing Platform Based on Chemically Reduced Graphene Oxide. *Anal. Chem.* **2009**, *81*, 5603–5613, doi:10.1021/ac900136z.
31. Yang, S.; Guo, D.; Su, L.; Yu, P.; Li, D.; Ye, J.; Mao, L. A facile method for preparation of graphene film electrodes with tailor-made dimensions with Vaseline as the insulating binder. *Electrochem. Commun.* **2009**, *11*, 1912–1915.
32. Lin, W.-J.; Liao, C.-S.; Jhang, J.-H.; Tsai Y.-C. Graphene modified basal and edge plane pyrolytic graphite electrodes for electrocatalytic oxidation of hydrogen peroxide and  $\beta$ -nicotinamide adenine dinucleotide. *Electrochem. Commun.* **2009**, *11*, 2153–2156.

33. Tang, L.; Wang, Y.; Li, Y.; Feng, H.; Lu, J.; Li, J.; Preparation, Structure, and Electrochemical Properties of Reduced Graphene Sheet Films. *Adv. Funct. Mater.* **2009**, *19*, 2782–2789, doi:10.1002/adfm.200900377.
34. Rastogi, S.K.; Raghavan, G.; Yang, G.; Cohen-Karni, T. Effect of Graphene on Nonneuronal and Neuronal Cell Viability and Stress. *Nano Lett.* **2017**, *17*, 3297–3301.
35. Wang, R.; Shi, M.; Brewer, B.; Yang, L.; Zhang, Y.; Webb, D.J.; Li, D.; Xu, Y.Q. Ultrasensitive Graphene Optoelectronic Probes for Recording Electrical Activities of Individual Synapses. *Nano Lett.* **2018**, *18*, 5702–5708.
36. Aziz, A.; Asif, M.; Azeem, M.; Ashraf, G.; Wang, Z.; Xiao, F.; Liu, H. Self-stacking of exfoliated charged nanosheets of LDHs and graphene as biosensor with real-time tracking of dopamine from live cells. *Anal. Chim. Acta* **2019**, *1047*, 197–207.
37. Ryu, S.; Kim BS. Culture of neural cells and stem cells on graphene. *Tissue Eng. Regen. Med.* **2013**, *10*, 39–46.
38. Thomas, D.-G.; Kavak, E.; Hashemi, N.; Montazami, R.; Hashemi, N. Synthesis of Graphene Nanosheets through Spontaneous Sodiation Process. *J. Carbon Res.* **2018**, *4*, 42.
39. Yi, M.; Shen, Z. A review on mechanical exfoliation for the scalable production of graphene. *J. Mater. Chem. A* **2015**, *3*, 11700–11815, doi:10.1039/C5TA00252D.
40. Sechi, D.; Greer, B.; Johnson, J.; Hashemi, N. Three-dimensional paper-based microfluidic device for assays of protein and glucose in urine. *Anal Chem.* **2013**, *85*, 10733–10747.
41. Arapov, K.; Bex, G.; Hendriks, R.; Rubingh, E.; Abbel, R.; de With, G.; Friedrich, H. Conductivity Enhancement of Binder-Based Graphene Inks by Photonic Annealing and Subsequent Compression Rolling. *Adv. Eng. Mater.* **2016**, *18*, 1234–1239.
42. Chen, H.; Müller, M.B.; Gilmore, K.J.; Wallace, G.G.; Li, D. Mechanically strong, electrically conductive, and biocompatible graphene paper. *Adv. Mater.* **2008**, *20*, 3557–3561.
43. Das, S.R.; Nian, Q.; Cargill, A.A.; Hondred, J.A.; Ding, S.; Saei, M.; Cheng, G.J.; Claussen, J.C. 3D nanostructured inkjet printed graphene: Via UV-pulsed laser irradiation enables paper-based electronics and electrochemical devices. *Nanoscale* **2016**, *8*, 15870–15879, doi:10.1039/c6nr04310k.
44. Secor, E.B.; Prabhumirashi, P.L.; Puntambekar, K.; Geier, M.L.; Hersam, M.C. Inkjet printing of high conductivity, flexible graphene patterns. *J. Phys. Chem. Lett.* **2013**, *4*, 1347–1351.
45. Wu, L.; Chu, H.S.; Koh, W.S.; Li, E.P. Highly sensitive graphene biosensors based on surface plasmon resonance. *Opt. Express* **2010**, *18*, 14395.
46. Studer, A.M.; Limbach, L.K.; Van Duc, L.; Krumeich, F.; Athanassiou, E.K.; Gerber, L.C.; Moch, H.; Stark, W.J. Nanoparticle cytotoxicity depends on intracellular solubility: Comparison of stabilized copper metal and degradable copper oxide nanoparticles. *Toxicol. Lett.* **2010**, *197*, 169–174.
47. Caironi, M.; Gili, E.; Sakanoue, T.; Cheng, X.; Siringhaus, H. High Yield, Single Droplet Electrode Arrays for Nanoscale Printed Electronics. *ACS Nano* **2010**, *4*, 1451–1456, doi:10.1021/nn9014664.

48. Wang, S.; Ang, P.K.; Wang, Z.; Ling, A.; Tang, L.; Thong, J.T.L.; Loh, K.P. High Mobility, Printable, and Solution-Processed Graphene Electronics.
49. Xie, Y.; Yuan, P.; Wang, T.; Hashemi, N.; Wang, X. Switch on the high thermal conductivity of graphene paper. *Nanoscale* **2016**, *8*, 17581–17597.
50. Aparna, R.; Sivakumar, N.; Balakrishnan, A.; Sreekumar Nair, A.; Nair, S.V.; Subramanian, K.R.V. An effective route to produce few-layer graphene using combinatorial ball milling and strong aqueous exfoliants. *J. Renew. Sustain. Energy* **2011**, *5*, 033123.
51. Kim, Y.-K.; Min D-H. Durable Large-Area Thin Films of Graphene/Carbon Nanotube Double Layers as a Transparent Electrode. *Langmuir* **2009**, *25*, 11302–11306.
52. Yoo, D., Shiratori, S. S., & Rubner, M. F. Controlling bilayer composition and surface wettability of sequentially adsorbed multilayers of weak polyelectrolytes. *Macromolecules*, **1998**, *31*(13), 4309–4318.
53. Nur, H.M.; Song, J.H.; Evans, J.R.G.; Edirisinghe, M.J. Ink-jet printing of gold conductive tracks. *J. Mater. Sci. Mater. Electron.* **2002**, *13*, 213–219, doi:10.1023/A:1014827900606
54. Yudistira, H.T.; Nguyen, V.D.; Dutta, P.; Byun, D. Flight Behavior of Charged Droplets in Electrohydrodynamic Inkjet Printing. 2010.
55. Saito, R.; Hofmann, M.; Dresselhaus, G.; Jorio, A.; Dresselhaus, M.S. Raman spectroscopy of graphene and carbon nanotubes. *Adv. Phys.* **2011**, *60*, 413–550, doi:10.1080/00018732.2011.582251.
56. Sanchez, V.C.; Jachak, A.; Hurt, R.H.; Kane, A.B. Biological Interactions of Graphene-Family Nanomaterials: An Interdisciplinary Review. *Chem. Res. Toxicol.* **2012**, *25*, 15–34.
57. Majee, S.; Liu, C.; Wu, B.; Zhang, S.L.; Zhang, Z.B. Ink-jet printed highly conductive pristine graphene patterns achieved with water-based ink and aqueous doping processing. *Carbon N. Y.* **2017**, *114*, 77–83.
58. Overgaard, M.H.; Kühnel, M.; Hvidsten, R.; Petersen, S.V.; Vosch, T.; Nørgaard, K.; Laursen, B.W. Highly Conductive Semitransparent Graphene Circuits Screen-Printed from Water-Based Graphene Oxide Ink. *Adv. Mater. Technol.* **2017**, *2*, 1–7.
59. Tan, R.K.L.; Reeves, S.P.; Hashemi, N.; Thomas, D.G.; Kavak, E.; Montazami, R.; Hashemi, N.N. Graphene as a flexible electrode: Review of fabrication approaches. *J. Mater. Chem. A* **2017**, *5*, 17777–17803.
60. Vasilieva, F.D.; Kapitonov, A.N.; Yakimchuk, E.A.; Smagulova, S.A.; Antonova, I.V.; Kotin, I.A. Mildly oxidized graphene oxide suspension for printing technologies. *Mater. Res. Express* **2018**, *5*, 65608, doi:10.1088/2053-1591/aacb58.
61. Lin, Y.-C.; Lu, C.-C.; Yeh, C.-H.; Jin, C.; Suenaga, K.; Chiu, P.-W. Graphene Annealing: How Clean Can It Be? *Nano Lett.* **2011**, *12*, 414–419.
62. Xie, Y.; Xu, Z.; Xu, S.; Cheng, Z.; Hashemi, N.; Deng, C.; Wang, X. The defect level and ideal thermal conductivity of graphene uncovered by residual thermal reffusivity at the 0 K limit. *Nanoscale* **2015**, *7*, 10101–10110.

63. Xu, F.; Ge, B.; Chen, J.; Nathan, A.; Xin, L.L.; Ma, H.; Min, H.; Zhu, C.; Xia, W.; Li, Z.; et al. Scalable shear-exfoliation of high-quality phosphorene nanoflakes with reliable electrochemical cycleability in nano batteries. *2D Mater.* **2016**, *3*, 025005.
64. Hernandez, Y.; Nicolosi, V.; Lotya, M.; Blighe, F.M.; Sun, Z.; De, S.; McGovern, I.T.; Holland, B.; Byrne, M.; Gun'Ko, Y.K.; et al. High-yield production of graphene by liquid-phase exfoliation of graphite. *Nat. Nanotechnol.* **2008**, *3*, 563–568.
65. Pemathilaka, R.L.; Caplin, J.D.; Aykar, S.S.; Montazami, R.; Hashemi, N.N. Placenta-on-a-Chip: Placenta-on-a-Chip: In Vitro Study of Caffeine Transport across Placental Barrier Using Liquid Chromatography Mass Spectrometry (Global Challenges 3/2019). *Glob. Chall.* **2019**, *3*, 1970031.
66. Hashemi, N.; Lackore, J.M.; Sharifi, F.; Goodrich, P.J.; Winchell, M.L.; Hashemi, N. A paper-based microbial fuel cell operating under continuous flow condition. *Technology* **2016**, *4*, 98–103, doi:10.1142/S2339547816400124.
67. Sun, Y.; Lacour, S.P.; Brooks, R.A.; Rushton, N.; Fawcett, J.; Cameron, R.E. Assessment of the biocompatibility of photosensitive polyimide for implantable medical device use. *J. Biomed. Mater. Res. Part A* **2009**, *90A*, 648–655, doi:10.1002/jbm.a.32125.
68. Bai, Z.; Mendoza Reyes, J.M.; Montazami, R.; Hashemi, N. On-chip development of hydrogel microfibers from round to square/ribbon shape. *J. Mater. Chem. A* **2014**, *2*, 4878–4884.
69. McNamara, M.C.; Sharifi, F.; Okuzono, J.; Montazami, R.; Hashemi, N.N. Microfluidic Manufacturing of Alginate Fibers with Encapsulated Astrocyte Cells. *ACS Appl. Bio Mater.* **2019**, *2*, 1603–1613.
70. Acar, H.; Çinar, S.; Thunga, M.; Kessler, M.R.; Hashemi, N.; Montazami, R. Study of physically transient insulating materials as a potential platform for transient electronics and bioelectronics. *Adv. Funct. Mater.* **2014**, *24*, 4135–4143.
71. Ruiz, O.N.; Fernando, K.S.; Wang, B.; Brown, N.A.; Luo, P.G.; McNamara, N.D.; Vangsness, M.; Sun, Y.P.; Bunker, C.E. Graphene oxide: a nonspecific enhancer of cellular growth. *ACS Nano* **2011**, *5*, 8100–8107.
72. Bramini, M.; Alberini, G.; Colombo, E.; Chiacchiarretta, M.; DiFrancesco, M.L.; Maya-Vetencourt, J.F.; Maragliano, L.; Benfenati, F.; Cesca, F. Interfacing Graphene-Based Materials with Neural Cells. *Front. Syst. Neurosci.* **2018**, *12*, 12, doi:10.3389/fnsys.2018.00012/full.
73. Caplin, J.D.; Granados, N.G.; James, M.R.; Montazami, R.; Hashemi, N. Microfluidic Organ-on-a-Chip Technology for Advancement of Drug Development and Toxicology. *Adv Healthc Mater.* **2015**, *4*, 1426–1450.
74. Sharifi, F.; Patel, B.B.; Dzuilko, A.K.; Montazami, R.; Sakaguchi, D.S.; Hashemi, N. Polycaprolactone Microfibrous Scaffolds to Navigate Neural Stem Cells. *Biomacromolecules* **2016**, *17*, 3287–3297.
75. Seabra, A.B.; Paula, A.J.; De Lima, R.; Alves, O.L.; Durán, N.D. Nanotoxicity of Graphene and Graphene Oxide. **2014**, *4*(7), 4317–4323.

76. Akhavan, O.; Ghaderi, E. Toxicity of Graphene and Graphene Oxide Nanowalls Against Bacteria. 2010.
77. Hu, W.; Peng, C.; Luo, W.; Lv, M.; Li, X.; Li, D.; Huang, Q.; Fan, C. Graphene-Based Antibacterial Paper. **2010**.
78. Donaldson, K.; Aitken, R.; Tran, L.; Stone, V.; Duffin, R.; Forrest, G.; Alexander, A. Carbon Nanotubes: A Review of Their Properties in Relation to Pulmonary Toxicology and Workplace Safety. *Toxicol. Sci.* **2006**, *92*, 5–22.
79. Akhavan, O.; Ghaderi, E.; Akhavan, A. Size-dependent genotoxicity of graphene nanoplatelets in human stem cells. *Biomaterials* **2012**, *33*, 8017–8025.
80. Ou, L.; Song, B.; Liang, H.; Liu, J.; Feng, X.; Deng, B.; Sun, T.; Shao, L. Toxicity of graphene-family nanoparticles: A general review of the origins and mechanisms. *Part Fibre Toxicol.* **2016**, *13*, 57
81. Kurapati, R.; Backes, C.; Ménard-Moyon, C.; Coleman, J.N.; Bianco, A. White Graphene undergoes Peroxidase Degradation. *Angew. Chem. Int. Ed.* **2016**, *55*, 5506–5511, doi:10.1002/anie.201601238.

## CHAPTER 4. ELECTROJET PRINTED GRAPHENE MICROELECTRODES FOR REAL-TIME IMPEDANCE SPECTROSCOPY OF DOPAMINERGIC NEURONAL CELLS

Modified from a manuscript with the same name submitted to Biosensors and Bioelectronics.

Amir Ehsan Niaraki Asli <sup>1</sup>, Marilyn C. McNamara <sup>1</sup>, Reza Montazami <sup>1</sup>, Nicole N. Hashemi <sup>1,2\*</sup>

<sup>1</sup> Department of Mechanical Engineering, Iowa State University, Ames, IA 50011, USA

<sup>2</sup> Department of Biomedical Sciences, Iowa State University, Ames, IA 50011, USA

\* Corresponding author.

### Abstract

Investigation of the change in the electrochemical properties of neuronal cells upon exposure to stress factors imparts vital information about the stages prior to their death. This study presents a graphene-based biosensor for real-time monitoring of N27 rat dopaminergic cells which characterizes cell adhesion and cytotoxicity factors through impedance spectroscopy. The aim was to monitor the growth of the entire cell network via a non-metallic flexible electrode. Therefore, a water-based graphene solution was formulized as a conductive ink, 3D printed into a flexible substrate through a novel electrohydrodynamic approach, resulting in electrodes with a conductivity of  $6750\text{ s/m}$ . The presented high-throughput method enabled micro-scale monitoring of the entire cell network via the design of a PDMS-based growth channels. The electrical resistance of the cell network was measured continually along with their network density, constituting a mean density of  $1890\text{ cell/mm}^2$  at full cell confluency. The results demonstrate the applicability of the impedance-based sensing of the cell network for rapid screening of the cytotoxic elements, and the real-time effect of UV exposure on dopaminergic neurons was reported as an immediate application of the device.

## 4.1 Introduction

The behavior of neuronal cells is dependent on the growth environment that they experience. Thus, manipulating the micrometer and nanometer scale attachment cues for these cells can assist the investigation of their electrical and optical properties in-vitro.[1] Traditional patch clamp techniques provide high temporal resolution when obtaining single cell electrical recordings. However, they have proven to be ineffective for monitoring the activity of large neuronal networks.[2] Therefore, electrical recording and stimulation of neuronal networks through non-pervasive extracellular microelectrodes has been the topic of extensive research.[3] Microfabrication of extracellular electrodes enables multiplexed detection of large cellular activities on a scale that is not achievable by micropipette technology.[4]

A major challenge however, is to maintain a long-term connection between the soft cell tissue and the electrodes' conductive material, mainly due to the mechanical mismatch in the interface.[5], [6] It is particularly valuable to determine whether the impedance change of a model cell culture under stress is reflected in the kinematic of cell death. Gold electrodes have been employed to detect the change in local ionic environment caused by the cells' biological alterations.[7] For example, Diemert et al. studied the effect of impedance change in immortalized hippocampal neurons during the stages prior to their death with a gold electrode array.[8] Nevertheless, rigid metal-based electrodes can alter the cell shape, organization, and function of the cells, often leading to cytotoxicity and low cell viability.[9] Therefore, bilayer nanomesh[10] and indium tin oxide (ITO)[11] electrodes are reported as popular non-metallic conductive materials, but these alternatives are naturally brittle. In order to create a flexible platform, Adly et al.[12] created a carbon-based microelectrode array on PDMS and hydrogel. They further demonstrated the stimulation of cardiomyocyte-like HL-1 cells and recorded the membrane potential using this interface. Among other carbon-based materials, graphene has received growing attention for bio-interfacing within drug delivery, bioassays, biosensors, and biological tissue scaffolding for applications such as stem cell growth.[13], [14] There are numerous studies detailing

neuronal attachment and the capability of graphene to mediate cell growth and proliferation.[15] Here in, it is desirable to create a layered microstructure through inkjet printing of the water-dispersed graphene to more effectively detect the induced damage in neuronal cells. The microfluidic deposition of graphene electrodes can provide texture cues that are favored by the cells. Thus, the detection of cell detachment upon lift-off can be studied with high precision through impedance spectroscopy technique, where the cell body is treated as a physical particle which impedes the transfer of ionic current between the electrodes in the growth media.

Cell impedance spectroscopy via such carbon-based materials are detailed in benchmark studies for cancer diagnosis.[16], [17] Accordingly, inflicting cellular damage leads to alteration in membrane morphology, cellular shrinkage, detachment, and lift-off which will affect the cellular impedance.[8] With the aim of creating a real-time and continual monitoring platform for dopaminergic neurons, here a novel yet facile microfluidic approach is presented to fabricate a flexible graphene electrode array. Moreover, a PDMS-based passivation design is introduced to control the proliferation of N27 cells in microscale and enable visual and electrical monitoring of the entire cell network by limiting the proliferation to a fully visible growth channel. This high-throughput design enables data acquisition in a larger scale, compared to the traditional end-point assays. Following our previous work,[18], [19] aqueous graphene was synthesized by direct mechanical exfoliation of graphite with bovine serum albumin (BSA) through wet ball milling. It is known that BSA, among other proteins, can most effectively stabilize graphene platelets in water for biomedical purposes.[20]–[22] High concentration of graphene was dispersed in water through low-speed wet ball milling, which enhances the resulting conductivity of the electrodes after patterning.[23] The pure graphene solution was inkjet printed on treated polyimide (PI) substrate without addition of metal nano-particles, which are popular in graphene ink formulations,[24] followed by thermal treatment. We have found that, employing a strong electrostatic field during the printing process can consolidate the graphene on the substrate. Therefore,

the resultant microelectrodes could maintain their conductivity upon flexure without the addition of common insulating polymer binders such as ethyl cellulose.[25]

The quality of the utilized graphene in this study, was characterized by its Raman spectrum, transmittance electrode microscopy (TEM) and the surface morphology of the thermally treated graphene electrodes were examined by scanning electron microscopy (SEM). To quantify the flexibility of the sensor, resilience of the electrodes after bending and folding was tested for potential *in-vivo* applications. The effect of stress factors (UV exposure here) on the electrical impedance and the viability of the N27 cell culture was monitored continually to demonstrate the dynamic applicability of the device as a sensitive alternative to dye-based techniques.

## 4.2 Materials and Methods

### 4.2.1 Graphene Synthesis

A suspension of 20 mg/ml graphite (powder, <20  $\mu\text{m}$ , synthetic, Sigma Aldrich, catalog no. 282863), 2 mg/ml BSA (lyophilized powder, Sigma Aldrich, catalog no. A9418) was created in water. The suspension was ball milled at low rotational speed (300 rpm) for 90 h with 11/32" stainless steel balls. The solution then rested for ~48h to allow sedimentation of large graphite particles. 85% of the volume from the top was pipetted off to ensure removal of Fe impurities. The resultant graphene concentration was controlled by UV-vis spectrometer (PerkinElmer, Lambda 750).[18], [22] In order to characterize the produced graphene, Raman spectra of the samples were acquired using a BWTEK Voyage confocal Raman system (B&W Tek, Newark, DE, USA), with a CW laser (Excelsior-532-150-CDRH Spectra-Physics) as the energy source operating at the wavelength of 532 nm. The aqueous graphene was drop casted on **Si/SiO<sub>2</sub>** wafers with drop diameter of  $\approx 10$  mm. The data was collected on 5 different laser spots across 5 independently printed electrodes and 5 untreated graphene samples (a total of n=30) at laser integration time of 10 s. The SEM Images of printed graphene patterns on PI were captured via a JEOL FESM 6335 using 2–5 kV accelerating voltage. In order to prepare the graphene samples for TEM, they were diluted to 20  $\mu\text{g mL}^{-1}$  and were drop casted on a Cu-grid. The TEM

images were recorded using a JEOL JSM2100 STEM (Japan Electron Optics Laboratories, Mitaka, Tokyo, Japan) at 200 kV accelerating voltage. The impedance measurements were carried by a VersaSTAT 4 Potentiostat Galvanostat. All electrical measurements were performed inside a grounded aluminum Faraday cage. For more details on graphene characterization, ink flow properties, and surface morphology tests (AFM, TEM, UV-vis spectroscopy, profilometry) please refer to our previous work.[18], [19]

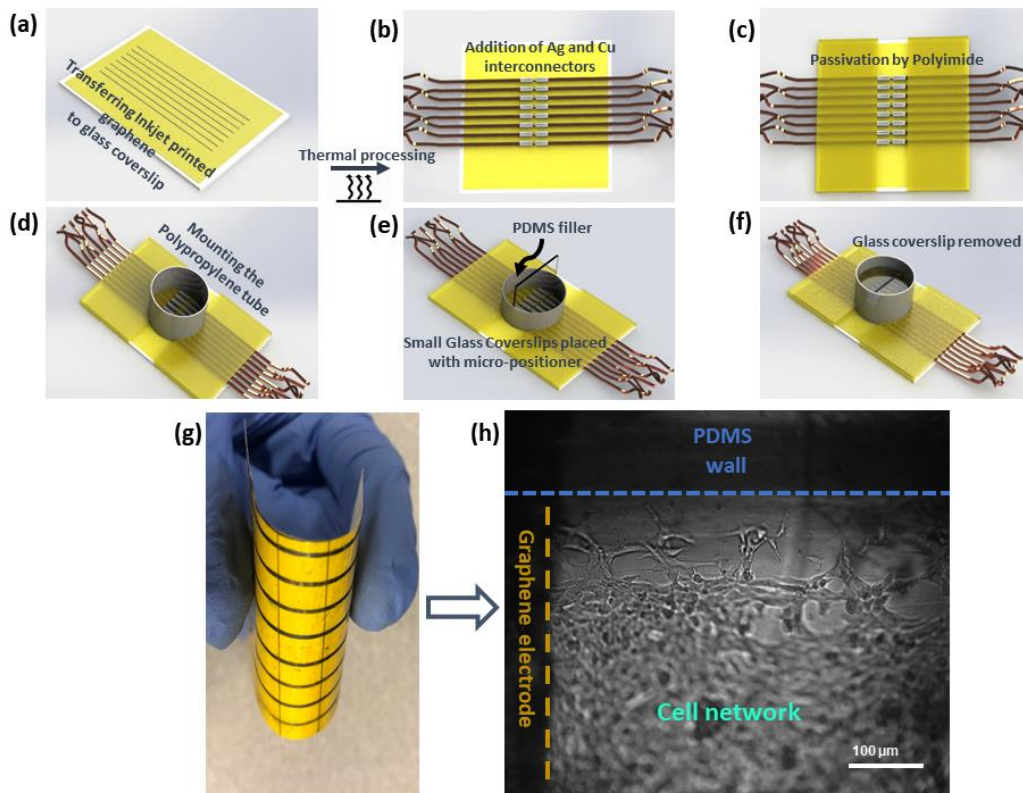


*Figure 0.1 Fabrication of graphene biosensors for real time monitoring of neuronal cells. (a) Transferring to glass coverslip. (b) Addition of silver and copper for connection to the potentiostat. (c) Stabilizing the interconnectors with PI tape. (d) Mounting the cell container (e) Creating the growth channel gap by micro-positioning a glass slide (f) Glass coverslip removal after PDMS hardening. (g) The flexible inkjet-printed Graphene pattern prior to biosensor fabrication. (h) Proliferation of neuronal cells in the growth gap 5 days after interfacing with graphene microelectrodes.*

#### 4.2.2 Device Fabrication

A PI film 70×50×1 mm (length×width×thickness) was washed with acetone and isopropyl alcohol (IPA) in a ultrasonic bath and blow dried by compressed Nitrogen. The PI film was initially submerged in a 12 mg/ml of Poly (4-styrenesulfonic acid) sodium salt (PSS) in deionized water for 20

min, followed by a submergence of 30 mg/ml Polyethyleneimine (PEI) in water. PSS and PEI were purchased from Sigma Aldrich (catalog no. 561959 and 408727 respectively). The water solvent contained a 0.5 M solution of NaCl prior to the addition of PEI and PSS. The substrate was rinsed with deionized water and thoroughly dried with compressed nitrogen before and after each submergence. The prepared graphene solution was then inkjet printed on PI (0.06 mm thickness) using an electrohydrodynamic inkjet printer. Briefly, the graphene ink was deposited on the treated PI in a single pass with a syringe pump in a constant flow regime (9  $\mu\text{L/s}$ ) with a 300  $\mu\text{m}$  needle, resulting in a finger thickness of 4  $\mu\text{m}$  width of 450  $\mu\text{m}$  and a spacing of 900  $\mu\text{m}$ . In order to ensure the binding of the graphene to the substrate, a constant electrostatic field was applied between the nozzle and the PI film. The consolidation of graphene patterns eliminated the need for binders like ethyl cellulose[26] and lead to stability at the time of flexure. The distance between the tip of the nozzle and the PI was set to 1 mm, while the electrical potential applied via a function generator was 3.5 kV. The fluid and properties of the electrohydrodynamic process is detailed in the supplementary information.

Fabrication process of the biosensor from graphene patterns is depicted in Fig. 1. First, the flexible substrate with printed graphene electrodes was transferred to 2"×3" glass coverslips and was thermally annealed at 280 °C for 30 min. Consequently, copper conductive tapes were attached to the graphene lines using Ag interconnectors and was fixed with PI film to prevent detachment upon connection to the data acquisition system. In order to create the growth channel, and ensure reliable cell growth, a 26 mm×100 mm Polypropylene tube (inner diameter × height) was mounted on the chip and sealed with Poly-dimethylsiloxane (PDMS). A glass cover slip was placed perpendicular to the graphene lines via a micro-positioner. The micro-positioning setup ensured a 4  $\mu\text{m}$  vertical distance, from the substrate's surface to the tip of the glass coverslip. Subsequently, 5 ml of PDMS was poured in with a 10:1 base-curing agent ratio for electrode passivation. The chip was thermally annealed in 85°C for 45 minutes in a convection oven and the glass slide was removed, leaving a channel width of 200  $\mu\text{m}$  (for 0.17 mm-thick slides) or 1 mm (for standard 1 mm-thick slides). Prior to seeding, all chips were

kept at room temperature overnight to ensure complete hardening of PDMS, followed by a wash-up with 70% ethanol and a 30 min long UV exposure in the culture hood.

#### **4.2.3 Electrochemical Characterization.**

Cyclic voltammetry (CV) was performed via a potentiostat in a three-electrode cell setup (PerkinElmer 4). A solution of 1 M KCl ( $\geq 99\%$  Sigma-Aldrich) was prepared in DI water as the electrolyte. Pt wire was employed as counter electrode and an Ag/AgCl electrode was submerged for reference electrode. The CV measurements were conducted to determine the faradaic peaks, in a potential range of -1 V to 1 V with respect to the Ag/AgCl electrode at the scan rate of 100 mV/S.

Electrical impedance spectroscopy (EIS) was performed in a three-electrode setup with the same potentiostat, with Phosphate Buffered Saline (PBS) as the electrolyte solution. Pt wire and Ag/AgCl electrode served as counter and reference electrode as well. The frequency was scanned from 10 kHz to 0.1 Hz with  $V_{DC} = 0$  and  $V_{AC} = 10$  mV. Both EIS and CV were performed in a grounded aluminum mesh, serving a faraday cage and were repeated for 5 electrodes on four separately fabricated chips ( $n=20$ ). In order to study the effect of cytotoxicity on the cell culture, the UV light was emitted via a Dymax BlueWave® 200 version 3.0 light-curing spot-lamp system in 20 s intervals with the intensity of  $40$  W/cm<sup>2</sup>. The resistance measurements were conducted via applying a linearly growing voltage between 0 V and 1 V across the electrode pairs with a scan rate of 50 mV/s.

#### **4.2.4 Cell Culture and Biocompatibility Analysis.**

The growth channels were designed to control the expansion of the cell network and facilitate the adhesion of neurons to the topological features of the graphene lines.[27] Therefore, a concentrated suspension of N27s in the growth medium (GM) was initially introduced to the growth channel to ensure the deposition of the neurons only on the electrode area. The GM contained RPMI medium 1640 (1X), 10% fetal bovine serum (FBS), 1% penicillin, and 1% L-glutamine. For all trials, cells were cultured in T-25 flasks at 70% confluency and were passaged at least three and no more than ten times prior to their introduction to the chips. In two day intervals, half of the volume of cultured cells were

replaced by fresh GM. The N27 cells were detached for passage using **0.025%** trypsin-EDTA. Cell suspension was centrifuged at 1500 rpm for 5 min and after the removal of trypsin-containing medium, was resuspended in fresh GM. A Trypan blue (Gibco BRL) viable cell count was performed before the cell passage to the chips with a medium to dye ratio of 1:9.

50 $\mu$ l of cell suspension was added to the growth channels with the size of 0.2mm  $\times$  26mm  $\times$  5mm (for *width*  $\times$  *length*  $\times$  *depth*). Six hours after the cell passage, an additional 2 ml of GM was added and the chip was incubated at 37°C in a 5% CO<sub>2</sub>/95% humidified air atmosphere for 5 days.

The biocompatibility of the chips was analyzed via a standard live-dead cell assay using a 70  $\mu$ M CellTracker™ CMFDA solution and an 80  $\mu$ m propidium iodide solution in FBS-free RPMI medium. 50  $\mu$ g of CellTracker™ was dissolved in 10.8  $\mu$ L of dimethyl sulfoxide (DMSO) to prepare the 70  $\mu$ M CellTracker™ CMFDA solution, prepared using FBS-free RPMI medium. 500  $\mu$ L of the prepared dye was added to the chip before incubating for 30 min. Subsequently, the dye was replaced by FBS-free RPMI medium after incubation to maintain the samples' moisture during the imaging. For the introduction to chips and viability test, all cell detachments were performed with 0.05% trypsinEDTA (Ginco BRL). The live-dead cell assay results were gathered by a Zeiss Axio Observer Z1 inverted microscope. During all the experiments, the dyes were covered to prevent their exposure to light. The microscope was set to capture Green excitation/emission spectra (492/517 nm maxima) for CellTracker™ CMFDA and red excitation/emission spectra (532/617 nm maxima) for propidium iodide. The viability was calculated with eq 1, where green refers to the live cells stained by CellTracker™ CMFDA and red refers to the dead cell stained by propidium iodide. The statistical analysis was performed using a two-sided student's test.

$$viability = \frac{Live\ cells\ (green)}{Live\ cells(green) + Dead\ cells(red)} \times 100 \quad (1)$$

### 4.3 Results and Discussion

The change in mechanical and electrical properties of graphene, from an aqueous ink to a post-processed conductive pattern requires vigilant examinations (Fig. 2). Raman spectroscopy is the best source of information for investigating the structural integrity of the graphene samples.[28] The presence of lattice defects directly affect the vibrational frequencies of the carbon atoms and are detectable via Raman spectroscopy. Raman spectra of the aqueous graphene (drop-casted on  $Si/SiO_2$  chips) and the thermally treated graphene electrodes are shown in Fig. 2a. The comparison between the Raman spectra of aqueous graphene and the treated patterned graphene shows no significant dislocation of the peaks (Table 1). The presence of a short D band at  $1357 \pm 2 \text{ cm}^{-1}$ , a sharp G band at  $1587 \pm 1 \text{ cm}^{-1}$ , and a symmetric 2D band at  $2700 \pm 2 \text{ cm}^{-1}$  with FWHM of  $52 \pm 7 \text{ cm}^{-1}$  are indicative of defect-free few layer graphene with  $\frac{I_D}{I'_D} = 1.2 \pm 0.2$ . [29] Notably, the ratio of the intensity of D band to the D' shoulder peak characterizes boundary defects ( $I_D/I'_D > 3.5$ ), vacancy basal plane point defects ( $I_D/I'_D > 7$ ), and  $sp^3$  defects ( $I_D/I'_D > 13$ ). [22] Prior to patterning, the suspension of graphene nano-sheets in water was also examined via TEM imaging. Fig. 2b demonstrates a single graphene platelet among BSA nano particles that enable its suspension in water. Owing to its few-nanometer thickness the graphene nano sheets appears to be almost transparent.

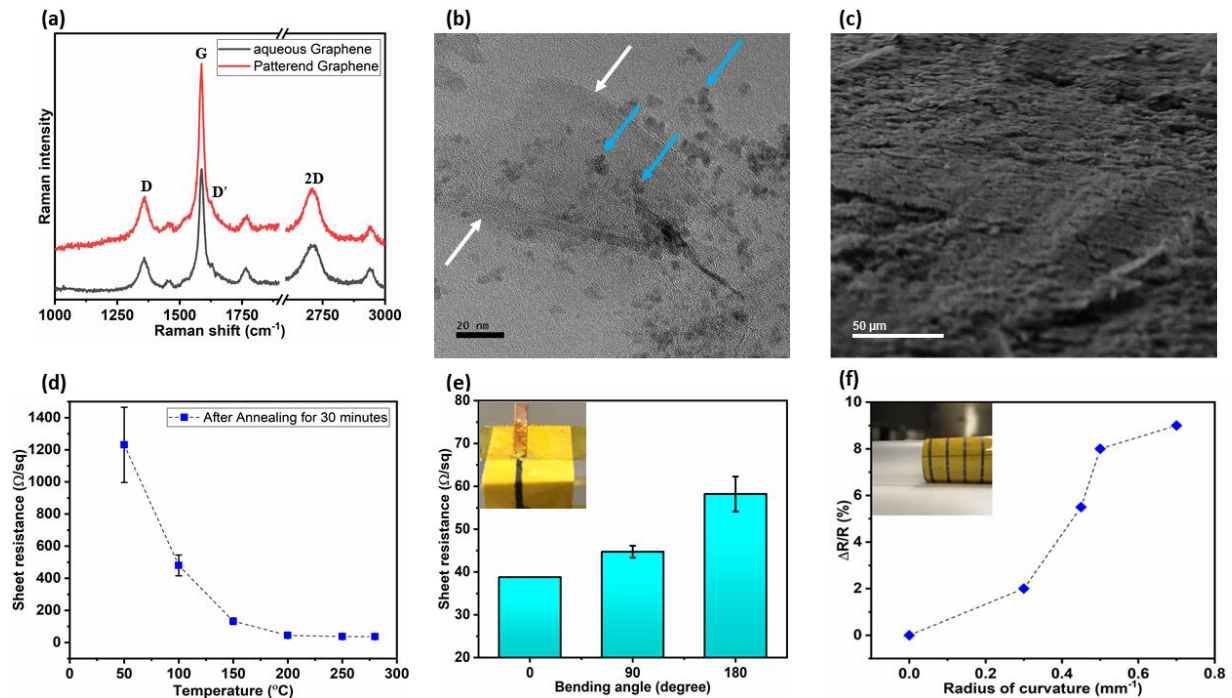


Figure 0.2 Characterization of aqueous graphene ink before and after patterning. (a) Raman spectra of aqueous graphene and treated graphene electrodes acquired at  $\lambda = 532$  nm. (b) TEM imaging of graphene platelets in water. The graphene nanosheets are shown with white arrows and BSA nano particles are shown with blue arrows. Scale bar: 20 nm (c) SEM imaging of annealed graphene electrodes. Scale bar: 50 microns. (d) Reduction in sheet resistance of the shear exfoliated graphene after 30 minutes of annealing in temperatures varying from 50°C to 300°C. (e) The change in the sheet resistance of 10 mm long graphene lines after attachment to glass cover slips with respect to 90° and 180° folding angles (f) The relative change in resistance of 20 mm long graphene lines with respect to various radii of curvature.

Since the produced graphene solution is ionically charged, surface modifications on the PI tape deemed vital to ensure the wettability of the substrate prior to inkjet printing process. Contact angle of the graphene ink decreased from 64° to 24° when dropped on the hydrophilic surface of treated PI substrate, compared to the untreated tape (Fig. S1).

Table 0.1. Raman analysis of shear-exfoliated graphene before and after inkjet printing and thermal processing. Results are presented as mean  $\pm$  SD, across 5 independently fabricated electrodes and drop casted aqueous graphene for 5 laser spots each (n=30).

Graphene	D position (cm <sup>-1</sup> )	G position (cm <sup>-1</sup> )	G fwhm (cm <sup>-1</sup> )	2D position (cm <sup>-1</sup> )	2D fwhm (cm <sup>-1</sup> )	I <sub>D</sub> /I <sub>G</sub>
<b>Pre-treatment</b>	1358 $\pm$ 0	1587 $\pm$ 1	17 $\pm$ 1	2700 $\pm$ 7	52 $\pm$ 7	0.25 $\pm$ 0.03
<b>Post-treatment</b>	1357 $\pm$ 3	1587 $\pm$ 1	17 $\pm$ 3	2703 $\pm$ 2	52 $\pm$ 5	0.32 $\pm$ 0.04

Traditionally, graphene ink formulations contain polymers such as ethyl cellulose to ensure their binding to the substrate during the thermal processing. It should be noted that, the overall conductivity of graphene patterns are hindered with the appearance of microscale cracks during the thermal processing or flexure, more so than the size of the nanosheets. Polymer binders though naturally insulating, are typically essential to maintain the microscale integrity of the printed lines. In order to bypass the need for the stabilizing binders and avoid numerous printing passes, here an electrostatic field was applied during the jetting processes to consolidate the graphene patterns on the PI substrate.

The fluid dynamic of the jetting process is modeled through the benchmark work of Fromm et al. where a dimensionless grouping of the Reynolds and Weber was used to solve the Navier-Stokes equation set. [30] Briefly, Eq. 2 defines the Ohnesorge number  $Z$ , where if it is too small the velocity is the dominant parameter and thus a large positive pressure is required for

droplet ejection leading to low velocity and short fluid column extension. In contrast, a high value of Ohnesorge number constitutes a long fluid column leading to the satellite drop formation behind the main drop. [31] Typically the  $Z$  value for Highly Loaded Particulate Suspensions should be between  $0.1 < Z < 1$ , and was shown to be equal to 0.23 for the inkjet printing method that was used in this study. Fluid properties are also important for determining the resultant resolution of the patterns upon droplet impact. Similar to the Ohnesorge number a generally accepted parameter for describing the splashing of droplets is given by Eq. 3 where high  $K$  value should be set to lower values than 100. When this dimensionless grouping of Reynolds and Weber number exceed this critical threshold, splashing may be observed depending on the temperature and substrate conditions. Parametric modeling of the graphene ink and the electrojet setup constitute an Ohnesorge value of  $Z=0.23$  and drop impact of  $K=12.99$  as detailed in supplementary information.

$$Z = \frac{(We)^{0.5}}{Re}; \quad 0 < Z^{-1} < 10 \quad (2)$$

$$K = We^{0.5} Re^{0.25}; \quad K < 100 \quad (3)$$

Thermal processing promotes the adhesion of graphene ink to the substrate while enhancing the electrochemical properties of the electrode through release of possible oxide compounds that may have been introduced during the ink formulation and printing process.[4] Moreover the SEM imaging can show that the surface morphology of thermally annealed electrodes with layered stack of carbon films can provide a desirable texture for neuronal adhesion.[32] The reduction on disorientation of the annealed patterns also hinders the probability of micro-scale junctions. As demonstrated in Fig. 2d, sheet resistance of the printed lines dropped from  $1200 \Omega/sqr$  to  $37 \Omega/sqr$  upon 30 minutes of annealing in  $280^\circ C$ . Therefore,

the equivalent conductivity of an electrode with cross-section size of  $450 \times 4 (\mu\text{m})^2$  reached to  $6750 \text{ S/m}$ .

In order to investigate the limits on the flexibility of the electrodes, the change in their resistance upon bending was studied, together with silver conductive ink and copper tape as interconnection setup. While curvature of the substrate affects the resistance of the lines minimally, sharp folding of the electrodes can introduce micro-scale cracks (Fig. 2e and f). In the trials on 20 electrodes, no case of absolute line disconnection was observed, but the average sheet resistance increased from  $37 \Omega/\text{sqr}$  to  $58 \Omega/\text{sqr}$  after sharp  $180^\circ$  folding.

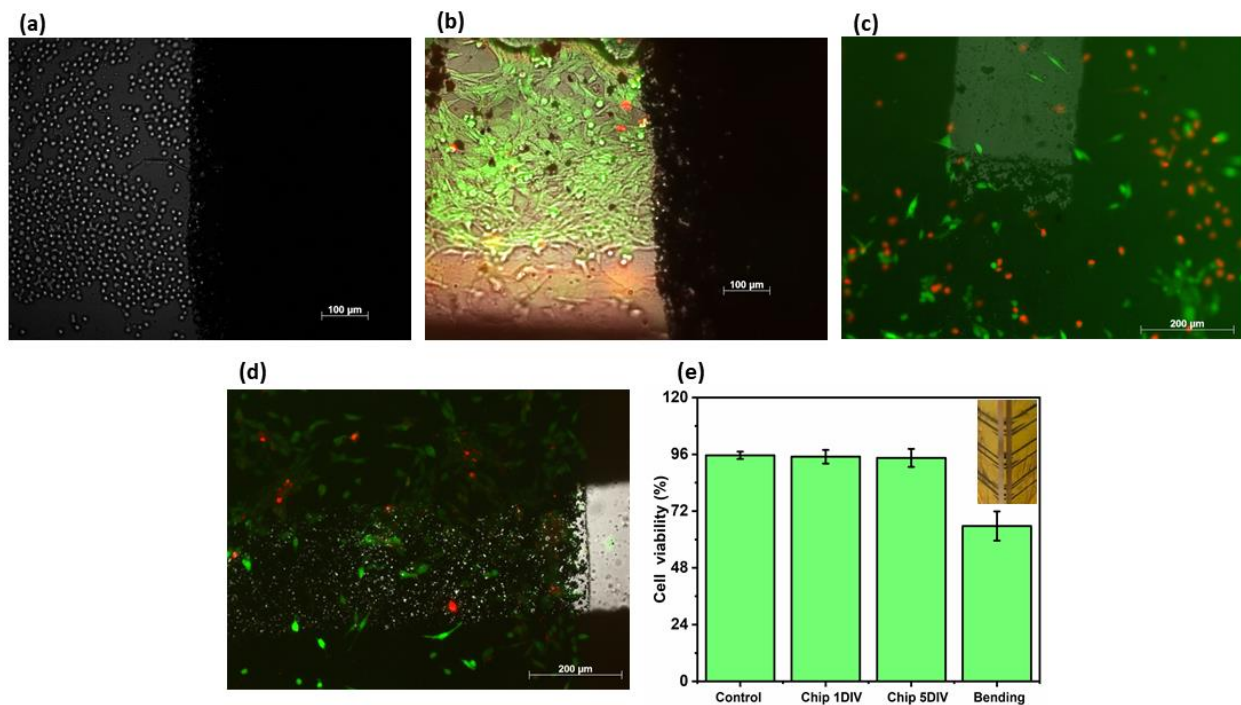


*Figure 0.3 Cell adaptability on the biosensor. (a) The N27 cells immediately after passage to the growth channel. (b) Cell viability after 5 days in-vitro. (c) Live-dead cell assay after the cell growth in conjunction with the bending of the electrodes with folding angle of  $90^\circ$ . (d) Live-dead cell assay after the removal of the PI substrate with the microchannel from the glass substrate. The electrodes in the growth channel were washed up with media and are turned upside down for 5 minutes. The N27 cells surprisingly remained attached to the graphene lines but left the rest of the substrate area during the wash up. (e) A thorough cell viability test for the biochip, the control and the a bent electrode array with folding angle of  $90^\circ$ , reported as mean  $\pm$  standard deviation over one control, four independent chips ( $n=15$ ). One-way ANOVA  $p < 0.005$ .*

With flexible electrodes in-hand, we are interested in the level of adhesion of neuronal cells to the graphene interface. Fig. 3 shows the density of N27 cells in the biochip throughout the experiments. Controlling the growth area of the cells is a major need for monitoring the entire cell network.[1] Hence, the six-hour gap between the initial passage of the cells (Fig. 3a) and the final addition of GM was observed to be crucial for limiting the cells' mobility prior to their attachment. A concentration of  $2.55 \times 10^6$  cells/ml was cultured on the chips and the resulting cell densities were monitored for 5 days in vitro (DIV) with the resultant cell viability demonstrated in Fig. 3. It observed that, flexure of the electrodes after cell growth with a folding angle of  $90^\circ$  can result in a significant drop in cell viability to 66% (Fig. 3c and 3e). However, the cells in the control and in the growth enabled a cell viability of  $> 95\%$ . Thus, it can be concluded that the shear exfoliated graphene microelectrodes and the created growth channel induced no detectable cytotoxicity.

Impedance spectroscopy has been widely used to assess the growth of neurons, cancer cells and microbial biofilms, to characterize the physical processes at the electrode-biometrial interface, because it is a fast, sensitive and label-free technique.[33] When an electrostatic field is created between two electrodes submerged in ionic media, the cell body acts as insulating particles that impede the flow of the electric current at the cell-electrode interface, resulting in a measurable increase in the impedance. Therefore, the adhesion degree of the biological tissue to the interface material plays a key role in translating the damage intensity to the impedance as the sensing parameter. Fig. 3d demonstrates that, the N27 cells favor the surface morphology of the graphene pattern and show significant detachment degree. We have peeled off the PI substrate and washed the growth channel with media after cell staining, and surprisingly observed that

although the cells were fully washed on the clear substrate spots, many N27 cells remained attached to the graphene pattern.

In order to successfully examine the effect of damage on cell attachment, the electrical impedance of the electrodes both prior to and immediately after cell passage was tracked, as well as 1 to 5 times in each DIV thereafter until the cell network reached to its maturity. Here we define the network maturity by a cell density of  $> 1500 \text{ cells/mm}^2$ . In most of the trials, the cell network reached the desired density after three DIV. Real-time optical and electrical monitoring of the cell behavior was enabled throughout the entire growth channel. Since, the system could not be integrated in the incubator, repetitive rotation of the biochip in and out of the incubator appeared to be inevitable. See Fig. S3 for annotated components of the real-time monitoring of the cell network and Fig. S4 for CV and EIS characterization of the cell free electrodes in KCl and PBS.

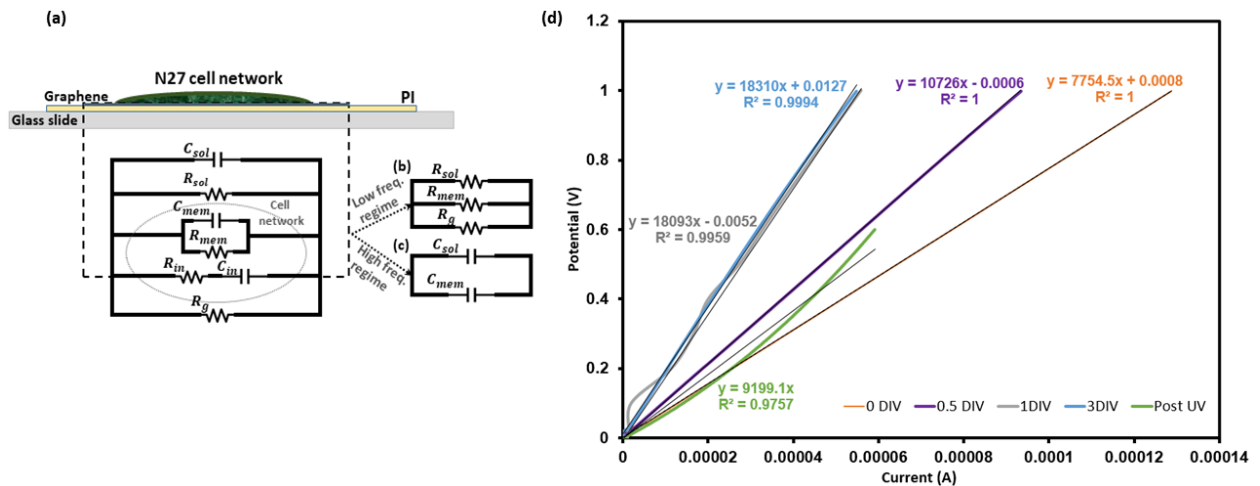
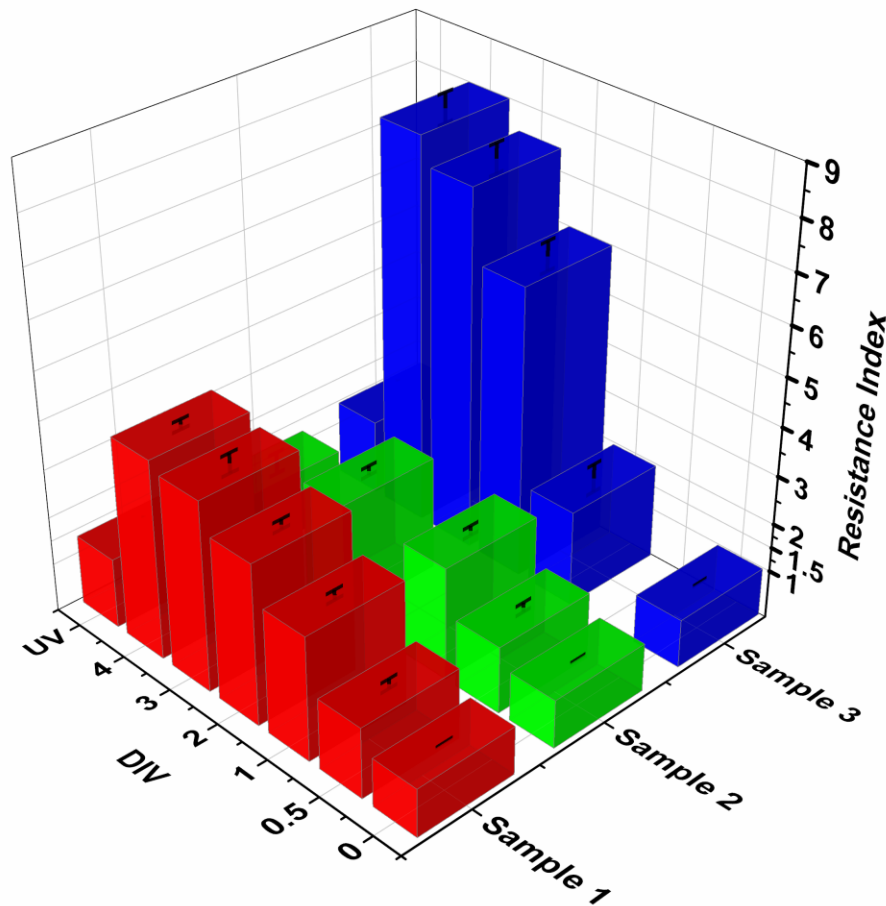


Figure 0.4 Equivalent circuit model of N27 cell electrical spectroscopy. (a) Overview. The equivalent circuit in (b) low and (c) high frequency regimes. (d) A sample impedance measurement in low frequency regime that constitutes the resistance of the cell network from seeding (0 DIV) to 3 DIV and after UV exposure scanned with 10 mV/s. The equation for the linear regression fitting line is also shown on the graph with the slope as the resistance value given by the Ohm law and  $R^2$  goodness-of-fit measure for the regression fitting.

To induce the stressor, the cells were exposed to a high-intensity light-curing spot-UV-lamp system for 20 s. The exposure of N27 cells to  $40 \text{ W/cm}^2$  of UV light leads to almost immediate cell shrinkage and lift-off. We are interested in measuring the change in electrical impedance of each electrode right before and after the UV exposure. The equivalent circuit is presented in Fig. 4, adapted from the benchmark studies for cancer diagnosis via impedance measurements,[16] where the capacitance and resistance of the inner parts of the cell (cytoplasm and conductive regions) are given as  $C_{in}$  and  $R_{in}$  respectively. The  $C_{mem}$  refers to the lipid bilayer and  $R_{mem}$  represents the ion channels in the cell network.[16] The capacitance and resistance of the ionic growth medium is shown by,  $C_{sol}$  and  $R_{sol}$  respectively. At frequency of  $\omega$ , the cell impedance measurement on graphene electrodes can be described by Eq. 4:

$$Z_{cell} = \frac{R_{mem} + j\omega R_{mem} R_{in} C_{in}}{1 + R_{in} R_{mem} + j\omega(R_{mem} C_{mem} + R_{in} C_{in}) - \omega^2(R_{mem} R_{in} C_{in})} \quad (4)$$



*Figure 0.5 The resistance of the graphene electrodes, during the cell network maturity ( $> 1500 \text{ cells/mm}^2$ ) and Post UV exposure were normalized with respect to the resistance of the electrodes right after cell passage to give the resistance index. The growth rate of the cell network and their resultant confluence determines the resistance index across the electrodes deposited in the growth channels. The rapid growth of the index deaccelerates upon the network's maturity. Upon exposure to UV the cell impedance of samples 1-3 respectively drops to 1.44, 1.32 and 1.55 of the initial electrode impedance which represents cell shrinkage and lift-off due to cytotoxicity. The cell density on each electrode determines the value of the index on the particular electrode-cell interface.*

Generally, within an individual cell, the cytoplasm is the conductive region with conductance of one million times more than the cells' membrane.[16] Thus, the cell membrane lipid bilayer constitutes to the dominant capacitive component of the cell culture in the high frequency regime ( $C_{mem}$  in Fig. 4c). Likewise, the dielectric constant of the growth media is

significantly lower than the cell membrane as the solution is ionically charged. Therefore, in the low frequency regime where the resistive components are dominant the lowest resistor,  $R_{mem}$ , would play the main role in the parallel setup as is the case in this study (Fig. 4b). Fig. 4d demonstrates a sample reading of the microelectrode setup, for 0 to 3 DIV and after exposure of the cells to the stressor. The impedance measurement was conducted through staircase voltammetry with a low scan rate of 10mV/s.  $R^2$ , The goodness-of-fit measure of each regression line was almost always above 99% which confirms the linearity of the V-I curve and consequently shows the fully resistor behavior of the membranes which simplifies the Eq. 4 to the equivalence circuit shown in Fig. 4b.

It should be noted that, despite the availability of electrodes' impedance at any moment after seeding, the resistance of the cells prior to the maturity of the network may not be reliably calculable. Nevertheless, owing to the layered surface morphology of graphene electrodes, we observed that the N27 cell network fully adheres to the lines, and 100% confluence is achievable even after 1 DIV and consistently after 3 DIV. For instance, the behavior curve in 1 DIV demonstrates only a minimal difference when compared to the curve for 3 DIV. Overall, the microscale biological status of the cell-graphene interaction affects the measured impedance as a consequence of constant modification of the ionic environment around the electrodes. Thereby, in addition to cell viability which is observable through optical methods, the cell number, morphology and adhesion degree can be determined by real-time monitoring of the electrode impedance. In order to enable repeatable monitoring of the cell network, the impedance is normalized as a dimensionless parameter, Resistance Index (RI), given in Eq 5:

$$RI_i = R_{cell}(t_i)/R_{init} \quad (5)$$

Where, at any measurement time instance  $t_i$ , the end to end time-dependent measured impedance of the cells  $R_{cell}(t_i)$ , is divided to the initial impedance of the electrodes with media before cell adhesion  $R_{init}$ . Fig. 5 demonstrates the change in RI across multiple samples for instances immediately after seeding to day 4 where the networks were exposed to UV light. Although in every trial RI reaches to a relatively constant value upon full confluence, the resultant RI is highly dependent on the cell density and the particular cell formation around the electrodes. Nevertheless, exposure to UV results in cell shrinkage and lift-off which in turn results in a reduction of the electrode-membrane interface area and extreme reduction of RI as the electrodes can be exposed to the ionically charged medium.

In order to generalize the analysis, the cell density was visually monitored at the time of impedance measurement to give the normalized resistance index of the cell network (NRI) given in Eq. 6. Where,  $\sigma_i$  gives the lateral cell density in  $cell/mm^2$  at any measurement instance.

$$NRI_i = RI_i/\sigma_i \quad (6)$$

The idea is to enable the dynamic monitoring of real-time neuronal responses to the stress factors without the dye assays. Although the exact time frame in which the cell network reaches through confluence may vary from chip to chip, optical measurement of cell density along with electrical spectroscopy can result in NRI which can represent cell adhesion degree and networks' real-time viability without the need for repetitive fluorescence assays. Fig. 6 demonstrates that upon maturity of the cell network ( $\sigma_i > 1500 \text{ cell}/mm^2$ ) the NRI remains stable around 4.5 times of its initial value across all covered electrodes. This value drops to an average of 1.45 when the introduction of cytotoxic factor leads to cell shrinkage and contraction of the network (Fig. 6f). It is worth noting that, defining a measure for cell density after complete death of the network did not seemed possible as the cells slowly start to raise in medium while a small

portion of them appear to be entrapped by the body of the electrode. This partial entrapment along can be the cause of the remaining discrepancy in the NRI before the seeding and eventual impedance upon the lift-off. The effect can also be observed in Fig. 4d where the V-I curve of the cell network after the UV exposure does not completely follow the Ohm law. The preference of the cell network for adhering to the electrodes as opposed to the PDMS-substrate corners could be a result of utilizing few layer aqueous graphene as the working material. Throughout the in-vitro studies on neuronal cells it is commonly reported that, [34]–[36] cultured cells often aggregate in the corners or the trenches of the microchannel systems due to the presence of textural cues.[37] Accordingly, the layered structure of the inkjet-printed graphene electrodes can be suitable for cell attachment which is vital for establishing a stable communication pathway in the cell-electrode interface (Fig. 3d). The accuracy of the presented method is highly reliant on the fact that the entire body of the network could be monitored owing to the narrow growth channels. Nevertheless, vertical aggregation of the cells appears to be inevitable which was shown to have minimal effect on the NRI but can hinder the cell density measurement and can be considered as a source of error for the monitoring system. This was one motive for conducting the experiments on the effect of stress factors no later than 5 DIV.

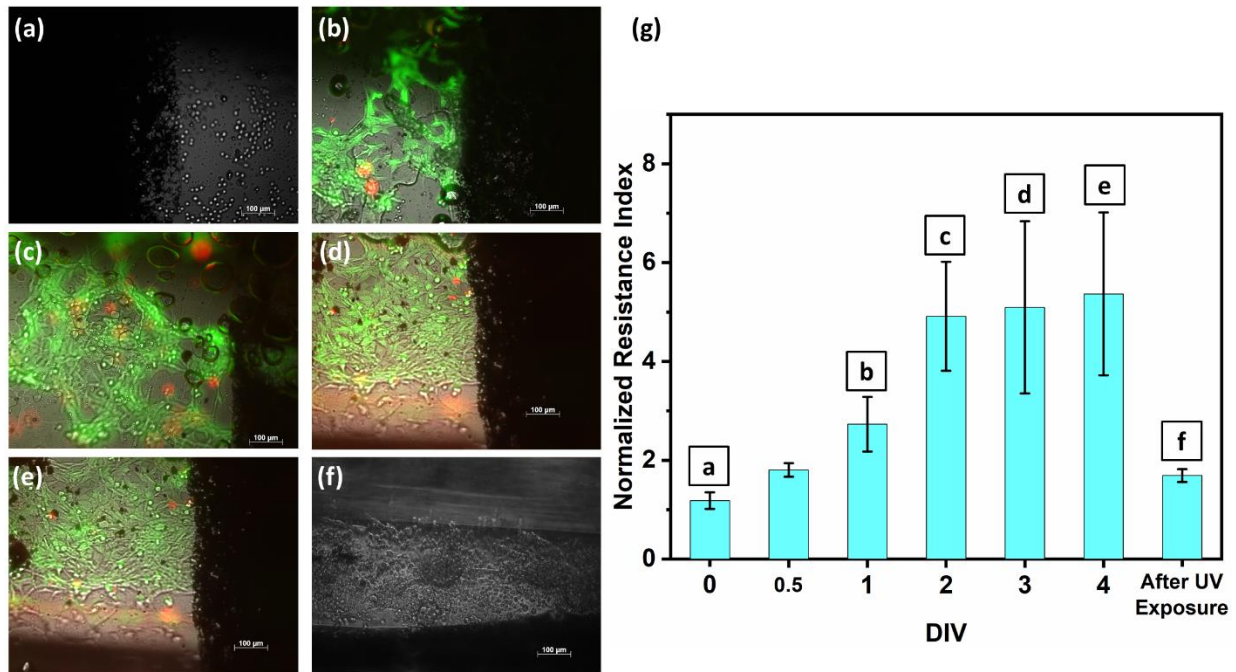


*Figure 0.6 The optical microscopy images of the N27 cell network (left) along with the normalized cell index the corresponding density at each measurement instance (right). (a) The freshly passaged cells. Sample image of the cell network after (a) 1 DIV (b) 2 DIV (c) 3DIV (4) 4 DIV and (f) after 20 second exposure to UV light; scale bar 100 micron. Upon normalizing the resistance index with respect to the cell density the NRI can enable real-time monitoring of the cell network prior to UV exposure. The graph is presented in terms of mean  $\pm$  standard deviation of NRI across 5 independent chips monitored 1-5 times per day for 4 DIV followed by UV exposure ( $n = 60$ ). Upon the network maturity (by 3DIV), the cell density across all experiment can be given as  $1890 \pm 230$  cells/mm<sup>2</sup>.*

Overall, the effect of stress factors on the NRI of the dopaminergic cells can be considered as an immediate application of the proposed system. In particular the N27 cell line is a common model for Parkinson's disease and has been a subject of investigation for understanding neurotoxicity and oxidative stress factors in numerous of studies. The flexibility of the electrode array can suggest further applicability of the framework for future in-vivo studies.

#### 4.4 Conclusion

Presented here, is a graphene-based biosensor that is easily-made and capable of in-vitro monitoring the electrical impedance of cell network in real time. The abundantly available cell assays are normally pervasive can provide information only for defined endpoint measurement. Therefore, the inkjet-printed electrodes were equipped with microfluidic design of growth channels to control the growth of the cell network. Doing so, enabled real-time optical monitoring of the entire cell network along with electrical spectroscopy. As a proof of concept, the N27 cells were passaged in the microchannel, grew till network maturity, exposed to UV as the cytotoxic element and the change in their resistance index and density was reported at every stage of during this period. The water-based graphene electrodes can show resilience from bending and folding without addition of polymer binders and could maintain its high conductivity with presence of no metal nano-particles. This can suggest the potential use of the presented method for future in-vivo studies. Moreover, adhesion of the cell network to the graphene electrodes was demonstrated and an average cell density of  $1890 \text{ cells/mm}^2$  was resulted along with a rapid 100% cell confluency on the presented microelectrode interface.

#### References

- [1] J. N. Hanson, M. J. Motala, M. L. Heien, M. Gillette, J. Sweedler, and R. G. Nuzzo, "Textural guidance cues for controlling process outgrowth of mammalian neurons," *Lab Chip*, vol. 9, no. 1, pp. 122–131, 2009.
- [2] M. E. Spira and A. Hai, "Multi-electrode array technologies for neuroscience and cardiology," *Nat. Nanotechnol.*, vol. 8, no. 2, pp. 83–94, Feb. 2013.
- [3] K. D. Wise, J. B. Angell, and A. Starr, "An Integrated-Circuit Approach to Extracellular Microelectrodes," *IEEE Trans. Biomed. Eng.*, vol. BME-17, no. 3, pp. 238–247, 1970.

- [4] S. K. Rastogi, J. Bliley, D. J. Shiwarski, G. Raghavan, A. W. Feinberg, and T. Cohen-Karni, "Graphene Microelectrode Arrays for Electrical and Optical Measurements of Human Stem Cell-Derived Cardiomyocytes," *Cell. Mol. Bioeng.*, vol. 11, no. 5, pp. 407–418, 2018.
- [5] J. H. Lee, H. Kim, J. H. Kim, and S. H. Lee, "Soft implantable microelectrodes for future medicine: Prosthetics, neural signal recording and neuromodulation," *Lab on a Chip*, vol. 16, no. 6. Royal Society of Chemistry, pp. 959–976, 21-Mar-2016.
- [6] H. Acar, S. Çınar, M. Thunga, M. R. Kessler, N. Hashemi, and R. Montazami, "Study of Physically Transient Insulating Materials as a Potential Platform for Transient Electronics and Bioelectronics," *Adv. Funct. Mater.*, vol. 24, no. 26, pp. 4135–4143, Jul. 2014.
- [7] E. Liang Lim, C. Chin Yap, M. Hafizuddin Hj Jumali, M. Asri Mat Teridi, and C. Hoong Teh, "A Mini Review: Can Graphene Be a Novel Material for Perovskite Solar Cell Applications?," 2015.
- [8] S. Diemert *et al.*, "Impedance measurement for real time detection of neuronal cell death," *J. Neurosci. Methods*, vol. 203, no. 1, pp. 69–77, Jan. 2012.
- [9] S. Ali, I. B. Wall, C. Mason, A. E. Pelling, and F. S. Veraitch, "The effect of Young's modulus on the neuronal differentiation of mouse embryonic stem cells," *Acta Biomater.*, vol. 25, pp. 253–267, Oct. 2015.
- [10] Y. Qiang *et al.*, "Bilayer Nanomesh Structures for Transparent Recording and Stimulating Microelectrodes," *Adv. Funct. Mater.*, vol. 27, no. 48, p. 1704117, Dec. 2017.
- [11] G. W. Gross, W. Y. Wen, and J. W. Lin, "Transparent indium-tin oxide electrode patterns for extracellular, multisite recording in neuronal cultures," *J. Neurosci. Methods*, vol. 15, no. 3, pp. 243–252, Nov. 1985.
- [12] N. Adly *et al.*, "Printed microelectrode arrays on soft materials: from PDMS to hydrogels," *npj Flex. Electron.*, vol. 2, no. 1, pp. 1–9, 2018.

- [13] X. Ding, H. Liu, and Y. Fan, “Graphene-Based Materials in Regenerative Medicine,” *Adv. Healthc. Mater.*, vol. 4, no. 10, pp. 1451–1468, Jul. 2015.
- [14] W. C. Lee *et al.*, “Origin of enhanced stem cell growth and differentiation on graphene and graphene oxide,” *ACS Nano*, vol. 5, no. 9, pp. 7334–7341, Sep. 2011.
- [15] S. R. Das *et al.*, “Electrical Differentiation of Mesenchymal Stem Cells into Schwann-Cell-Like Phenotypes Using Inkjet-Printed Graphene Circuits,” *Adv. Healthc. Mater.*, vol. 6, no. 7, pp. 1–8, 2017.
- [16] M. Abdollahad, M. Janmaleki, M. Taghinejad, H. Taghnejad, F. Salehi, and S. Mohajezadeh, “Single-cell resolution diagnosis of cancer cells by carbon nanotube electrical spectroscopy,” *Nanoscale*, vol. 5, no. 8, pp. 3421–3427, Apr. 2013.
- [17] Y. A. Glickman *et al.*, “Electrical impedance scanning: a new approach to skin cancer diagnosis,” *Ski. Res. Technol.*, vol. 9, no. 3, pp. 262–268, Aug. 2003.
- [18] A. E. Niaraki Asli, J. Guo, P. L. Lai, R. Montazami, and N. N. Hashemi, “High-yield production of aqueous graphene for electrohydrodynamic drop-on-demand printing of biocompatible conductive patterns,” *Biosensors*, vol. 10, no. 1, 2020.
- [19] J. Guo *et al.*, “Viability of neural cells on 3D printed graphene bioelectronics,” *Biosensors*, vol. 9, no. 4, p. 112, Sep. 2019.
- [20] S. Ahadian *et al.*, “Facile and green production of aqueous graphene dispersions for biomedical applications,” *Nanoscale*, vol. 7, no. 15, pp. 6436–6443, Apr. 2015.
- [21] A. Pattammattel and C. V. Kumar, “Kitchen Chemistry 101: Multigram Production of High Quality Biographene in a Blender with Edible Proteins,” *Adv. Funct. Mater.*, vol. 25, no. 45, pp. 7088–7098, 2015.
- [22] K. R. Paton *et al.*, “Scalable production of large quantities of defect-free few-layer graphene by shear exfoliation in liquids,” *Nat. Mater.*, vol. 13, no. 6, pp. 624–630, 2014.

- [23] L. Huang, Y. Huang, J. Liang, X. Wan, and Y. Chen, "Graphene-based conducting inks for direct inkjet printing of flexible conductive patterns and their applications in electric circuits and chemical sensors," *Nano Res.*, vol. 4, no. 7, pp. 675–684, Jul. 2011.
- [24] J. A. Hondred *et al.*, "Printed Graphene Electrochemical Biosensors Fabricated by Inkjet Maskless Lithography for Rapid and Sensitive Detection of Organophosphates," *ACS Appl. Mater. Interfaces*, vol. 10, no. 13, pp. 11125–11134, 2018.
- [25] S. Majee, M. Song, S.-L. Zhang, and Z.-B. Zhang, "Scalable inkjet printing of shear-exfoliated graphene transparent conductive films," *Carbon N. Y.*, vol. 102, pp. 51–57, Jun. 2016.
- [26] E. B. Secor, B. Y. Ahn, T. Z. Gao, J. A. Lewis, and M. C. Hersam, "Rapid and Versatile Photonic Annealing of Graphene Inks for Flexible Printed Electronics," *Adv. Mater.*, vol. 27, no. 42, pp. 6683–6688, Nov. 2015.
- [27] N. Hashemi, J. M. Lackore, F. Sharifi, P. J. Goodrich, M. L. Winchell, and N. Hashemi, "A paper-based microbial fuel cell operating under continuous flow condition," *TECHNOLOGY*, vol. 04, no. 02, pp. 98–103, Jun. 2016.
- [28] A. P. Kauling *et al.*, "The Worldwide Graphene Flake Production," *Adv. Mater.*, vol. 30, no. 44, pp. 1–6, 2018.
- [29] Z. S. Wang *et al.*, "Raman spectroscopy of few-layer graphene prepared by C<sub>2</sub>-C<sub>6</sub> cluster ion implantation," *Nucl. Instruments Methods Phys. Res. Sect. B Beam Interact. with Mater. Atoms*, vol. 307, pp. 40–42, Jul. 2013.
- [30] J. E. Fromm, "NUMERICAL CALCULATION OF THE FLUID DYNAMICS OF DROP-ON-DEMAND JETS," *IBM J. Res. Dev.*, vol. 28, no. 3, pp. 322–333, 1984.
- [31] B. Derby and N. Reis, "Inkjet Printing of Highly Loaded Particulate Suspensions," *MRS Bull.*, vol. 28, no. 11, pp. 815–818, Nov. 2003.
- [32] D. W. Park *et al.*, "Graphene-based carbon-layered electrode array technology for neural imaging and optogenetic applications," *Nat. Commun.*, vol. 5, pp. 1–11, 2014.

- [33] J. Song *et al.*, “Enhanced Electrochemical Impedance Spectroscopy Analysis of Microbial Biofilms on an Electrochemically in Situ Generated Graphene Interface,” *ACS Sensors*, vol. 5, no. 6, pp. 1795–1803, Jun. 2020.
- [34] K. Gao *et al.*, “Design of a Microchannel-Nanochannel-Microchannel Array Based Nanoelectroporation System for Precise Gene Transfection,” *Small*, vol. 10, no. 5, pp. 1015–1023, Mar. 2014.
- [35] S. C. Gifford *et al.*, “Parallel microchannel-based measurements of individual erythrocyte areas and volumes,” *Biophys. J.*, vol. 84, no. 1, pp. 623–633, Jan. 2003.
- [36] Z. Bai, J. M. Mendoza Reyes, R. Montazami, and N. Hashemi, “On-chip development of hydrogel microfibers from round to square/ribbon shape,” *J. Mater. Chem. A*, vol. 2, no. 14, pp. 4878–4884, Apr. 2014.
- [37] F. Sharifi, B. B. Patel, A. K. Dzuilko, R. Montazami, D. S. Sakaguchi, and N. Hashemi, “Polycaprolactone Microfibrous Scaffolds to Navigate Neural Stem Cells,” *Biomacromolecules*, vol. 17, no. 10, pp. 3287–3297, Oct. 2016.

## CHAPTER 5. MINUTE-SENSITIVE EXTRA-CELLULAR DETECTION OF NEURONAL CELLS THROUGH FLEXIBLE ELECTROJET PRINTED GRAPHENE

Based on a manuscript in progress.

*Amir Ehsan Niaraki Asli<sup>1</sup>, Mehrnoosh Taghavimehr<sup>1</sup>, Reza Montazami<sup>1</sup>, Nicole N. Hashemi<sup>1,2</sup>*

<sup>1</sup> Department of Mechanical Engineering, Iowa State University, Ames, IA 50011, USA;

<sup>2</sup> Department of Biomedical Engineering, Iowa State University, Ames, IA 50011, USA

### 5.1 Introduction

Real-time measurement of the neuronal cells' electrochemical response to damage is a broadly sought goal. Fluorescent or colorimetric cell staining is the conventional method for the investigation of cytotoxicity. However, they are invasive and only provide the ability to monitor the behavior of cellular networks at the end-point. An alternative approach is to assess the potential cytotoxicity factors through extracellular measurements via microelectrode arrays.. The impedance measured is affected by the biological status of the cells interacting with the well surface. Cells that interact with the electrode modify the local ionic environment and lead to an increase in the impedance measured within the tissue culture well. Thus, the electrode impedance can be used to monitor cell number, viability, morphology, and adhesion degree.

Metals and some other well-known conductive materials (i.e. ITO) can alter cell shape, organization and function of the cell culture. Consequently, establishing a reliable communication between soft tissues and these brittle materials remains a challenge due to this mechanical mismatch. Fortunately, it is shown in numerous electrophysiological studies that, excitable cells grow compatibly in presence of graphene. Graphene is an one-atom-thick, two-dimensional, honey-combed arrangement of hybridized carbon atoms. As each carbon atom connects to its three neighbors through  $\sigma$ -bonds, the last electron will be left out-of-plane ( $\pi$  bond) resulting in the extraordinary conductivity of this material. Here, a novel method for

fabrication of a graphene microelectrode array is proposed that enables minute-sensitive temporal resolution at the time of the measurement.

Since most biological media and cell cultures are aqueous stable and biocompatible dispersion of graphene in water is much desired in biosensing applications. In this study, we combined the shear force of low speed wet ball milling with stabilizing characteristics of an edible protein to exfoliate graphene from pristine graphite in water. Next, the graphene solution was formulated as a conductive ink, 3D printed into a flexible substrate and consolidated via applying a strong electrostatic field. Finally, the N27 cells were cultured in the biosensor and their viability was measured along with the resistance of the lines.

The fabrication of graphene electrodes needs microscale patterning to obtain high resolution prints with the application in electronics. Laser patterning is among the methods that can create high quality patterns, however it costs a lot and has a difficult procedure. Other methods like chemical vapor deposition (CVD) and photolithography are complicated and time consuming and even need applying high temperatures and consuming solutions in several steps.

In this work, we used a simple, low cost and non-invasive method using a patterned vinyl mask that can be used to directly transfer the graphene on the substrate. In the E-jet printing process, optimizing the viscosity of ink is always a challenging parameter. Controlling the viscosity of ink is required since lower viscosity of inks will lead the ink to flow on the substrate and ruin the resolution of the prints, while higher ink viscosities cause clogging the ink in the tube and stops the ink jet printing process. Applying the proposed vinyl mask in the E-jet process can become a potential solution in using lower viscosity inks yet expecting high resolution from the final electrodes.

## 5.2 Materials and Methods

The first step in our method is designing the high resolution patterns using SolidWorks to achieve accurate dimensions of electrodes.

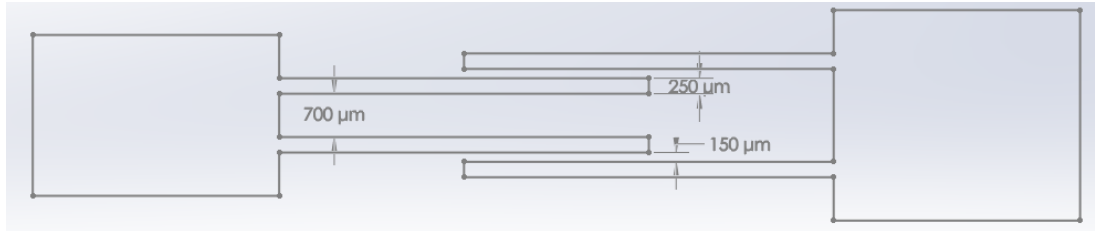


*Figure 0.1 Schematics and dimensions of the interdigitated electrode setup.*

According to the above figure, the design was performed in order to embed the electrodes in the cylindrical well (diameter of well can add here) that is considered to cover the cell media. Four sets of pairs of electrodes were cut into the vinyl mask using a vinyl cutter (US-Cutter, SC series) as can be seen from the below figure.



*Figure 0.2 Schematic of the designed pattern and the transfer method*

The design was optimized in a way to provide a straightforward transfer of the patterns to the substrate. After the cut, the pattern taped to the Kapton substrate and electrode patterns

removed to make a negative mask and the rest of the mask was not removed until the graphene dried at room temperature for 7 minutes. The electrodes were then E-jet printed in the designated areas and we could print back and forth to ensure a connected and high quality prints. Then, the mask was peeled off carefully leaving the precisely formed graphene electrodes on the substrate. In this stage, graphene electrodes are perfectly formed and are ready for the annealing step.

### 5.3 Results and Discussion

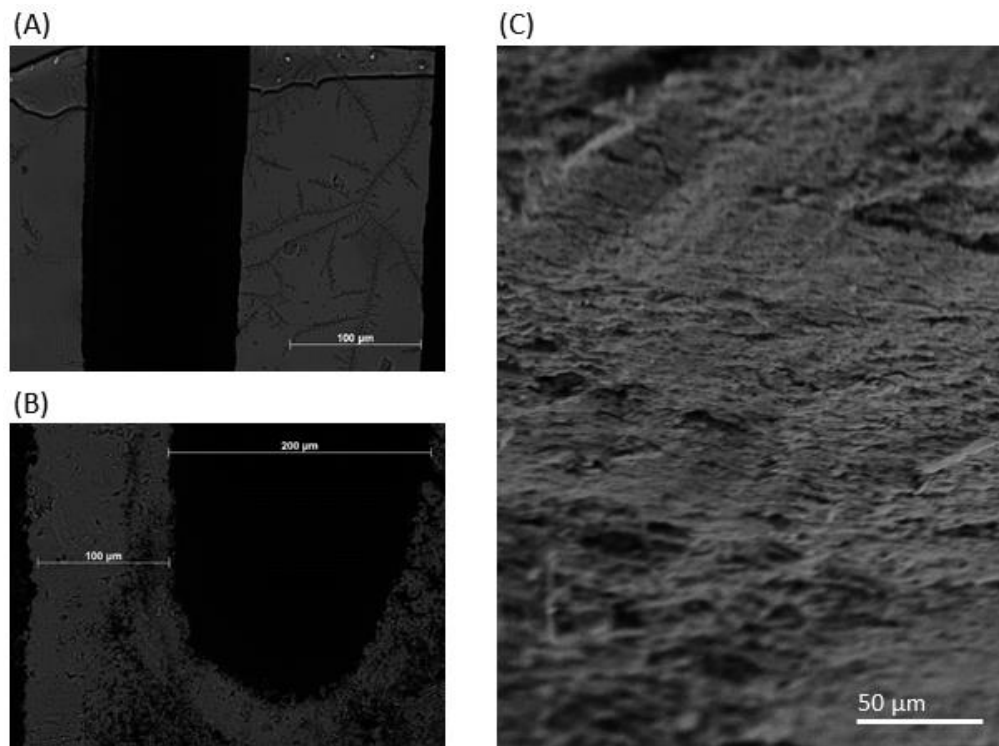


*Figure 0.3 Microscale characteristics and surface morphology of patterned graphene microelectrodes (A-B) Microscopic images of the electrodes in  $\times 10$  magnification; Scale bar=100  $\mu\text{m}$ . (C) SEM imaging of the electrodes with  $\times 400$  magnification; scale bar =50  $\mu\text{m}$ .*

The applied electrostatic field, resulted in high stability and a desirable surface morphology for cell adhesion as demonstrated in Figure 5.3. Additionally, thermal processing plays a vital role both in the improvement of the conductivity of the lines and in the resultant stability of the printed FLG.

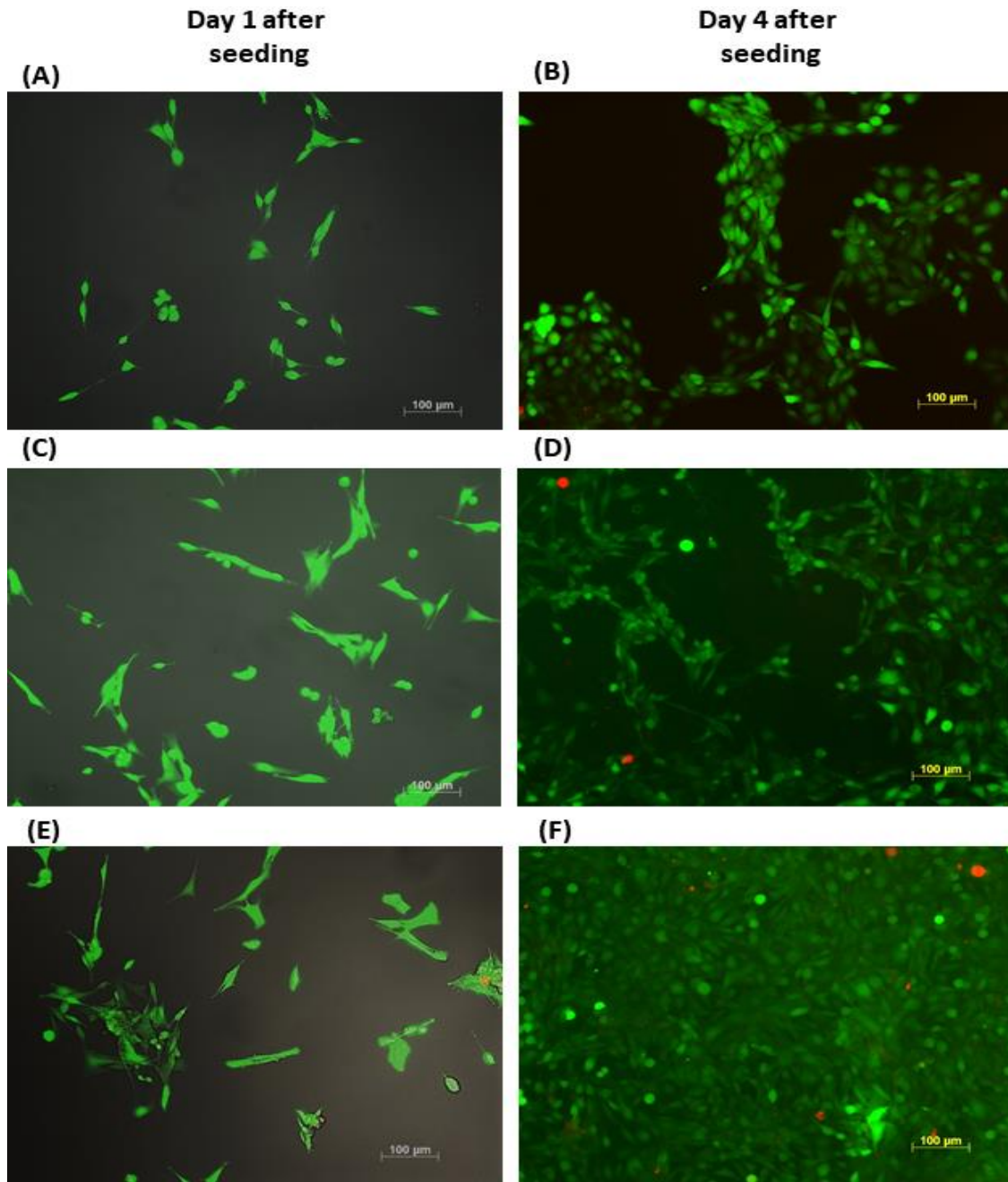


*Figure 0.4 Live-dead cell assay of the cell density on the chip. Each row demonstrates the initial seeding concentration of low, medium high (top to bottom) while left column demonstrates the first day in vitro and the right column shows the 3 DIV. Low concentration (66500 cells) are seeded which adhered with the concentration shown in (A) for 1 DIV and proliferated to (B) for 4 DIV. Medium concentration (133000 cells) are seeded which adhered with the concentration shown in (C) for 1 DIV and proliferated to (D) for 4 DIV. High concentration (266000 cells) are seeded which adhered with the concentration shown in (E) for 1 DIV and proliferated to (F) for 4 DIV.*

In order to normalize the measured impedance of the cell lines by their density, various cell seeding concentrations were experimented. Figure 5.4 demonstrates the live-dead assay images of the resultant cell density with respect to initial seeded cell count and days in vitro. After counting, the resulted cell density across all trials are given in Figure 5.5 for 5 instances per experiment (n=60). This data was used to provide real-time information to the measured impedance spectrum through offsetting the measured impedance by the cell density around the electrode at the time of experiment.

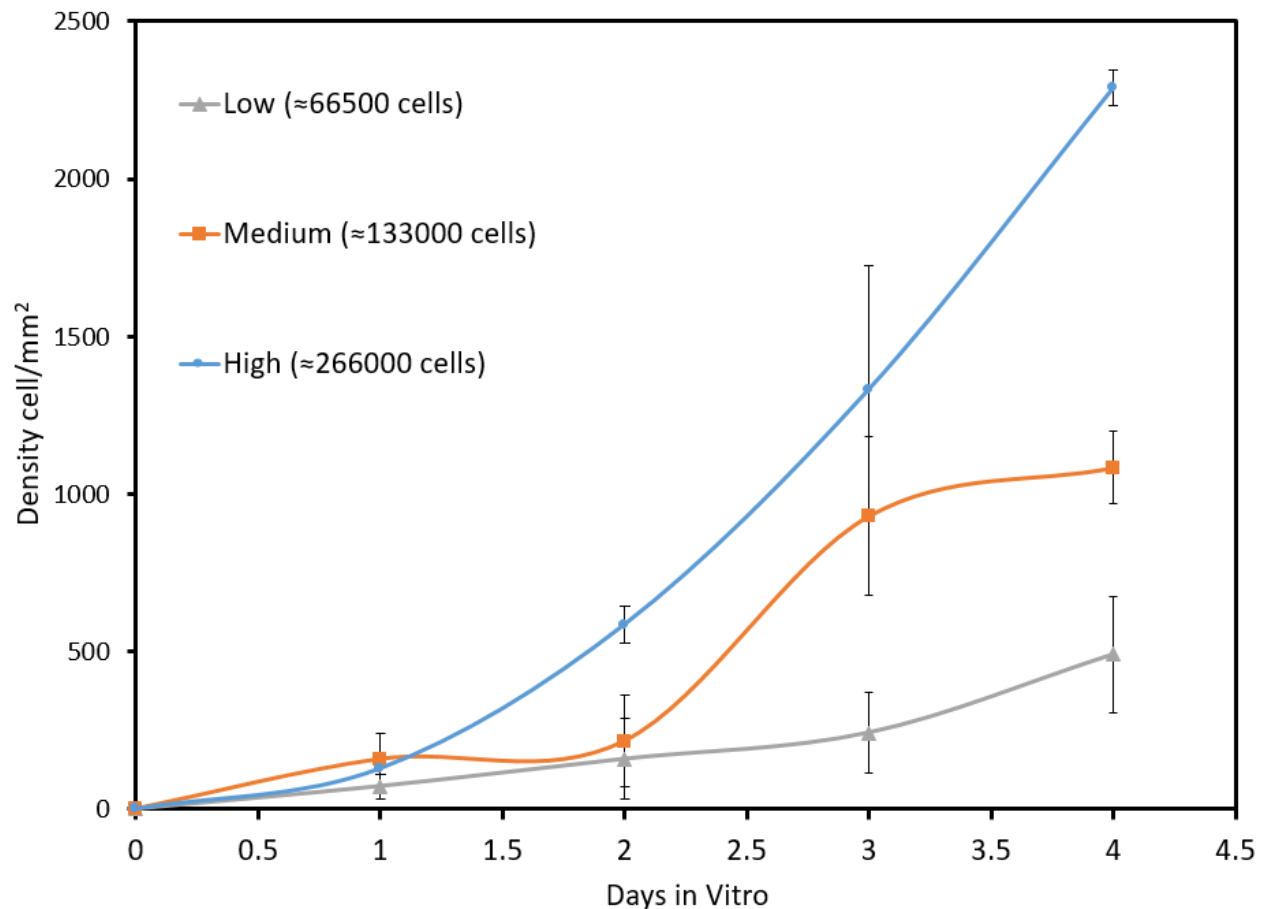
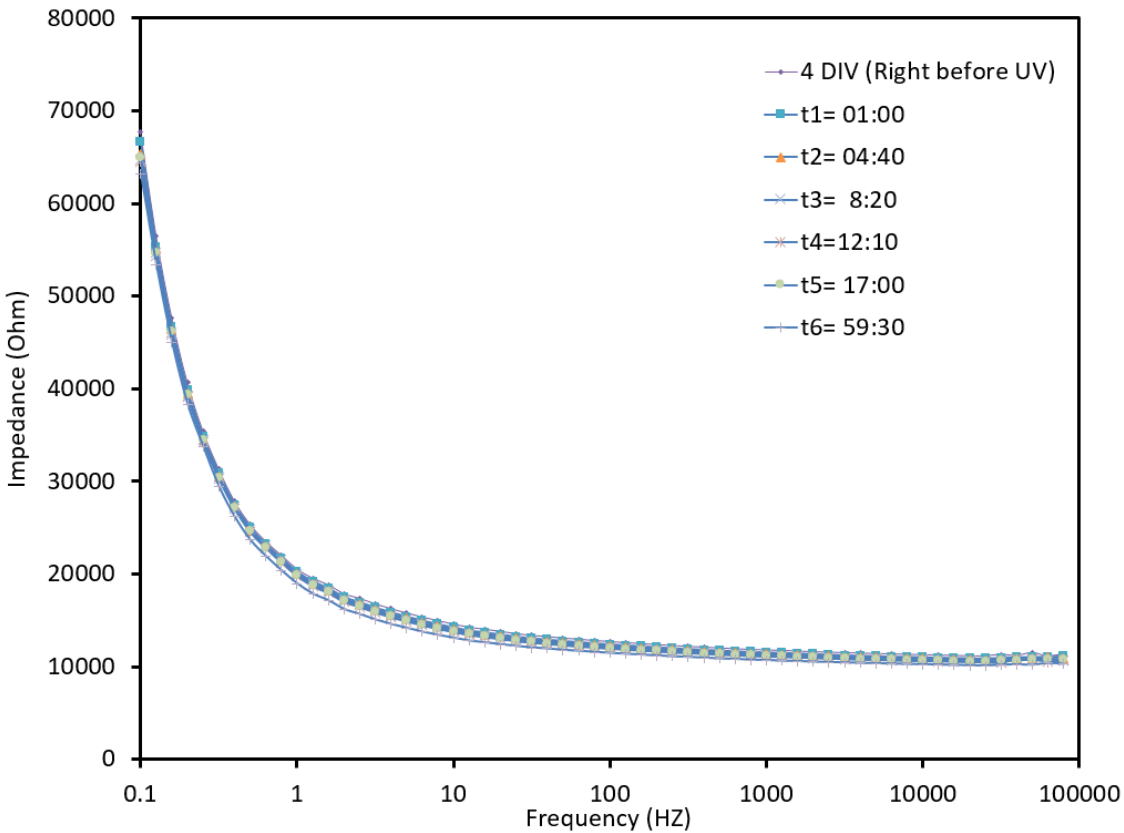
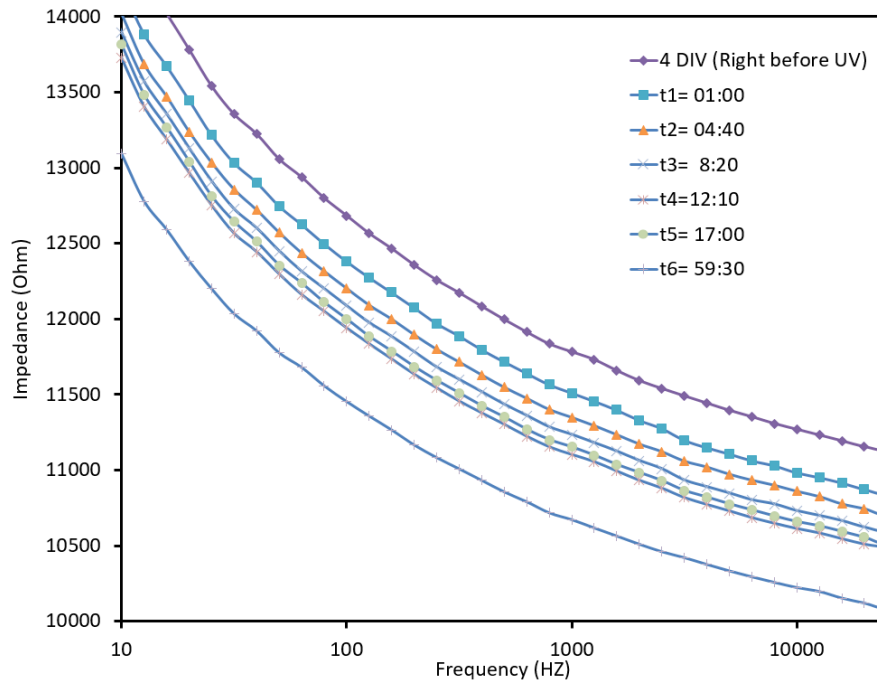


Figure 0.5 Cell density for various seeding cell concentrations in the first 4 days of cell growth.



*Figure 0.6 Electrical impedance measurement over the confluent N27 cells from 0.1 Hz to 100 kHz.*

The N27 cells were monitored for 4 days in vitro simultaneously through the microscopic setup and the potentiostat (Figure 1.9). The impedance measurements reached to a steady spectrum upon complete cell confluence usually after 3 DIV. In the 4<sup>th</sup> day, one EIS measurement was taken for the baseline, followed by UV exposure in 1 minute intervals. Figure 5.6 and 5.7 demonstrate the resultant spectrum. The results suggest that, the fabricated graphene microelectrode array is capable of detecting the change in cell body alteration neuronal cells with temporal resolution of a minute. This can be owed to the advantageous surface morphology of these electrode when compared to the silver or gold counterparts, which provide desirable attachment cues for the cell line.



*Figure 0.7 Magnified EIS measurement of confluent N27 cells under UV exposure in 1 minute intervals. The x axis is given in logarithmic scale for frequencies ranging from 10 Hz to 10 kHz.*

In order to demonstrate the applicability of the biochip for utilizing the introduction of impedance through the cell body as the sensing parameter, Figure 5.8 is presented. Identifying the exact frequency at which the change in impedance spectrum is identifiable is a cumbersome task as it may vary from one electrode-pair to another.

This study was initiated to discover a high-throughput methodology for sensing the inflicted damage to neuronal cells. Graphene was chosen as the interface material owing to its extraordinary conductivity and flexibility while the novel microfluidic approach for electrode patterning created a porous scaffold for neuronal growth. Figure 5.9 is the concluding piece that demonstrates a normalized Impedance Index based at each minute to demonstrate the hypersensitivity of the biosensor design.

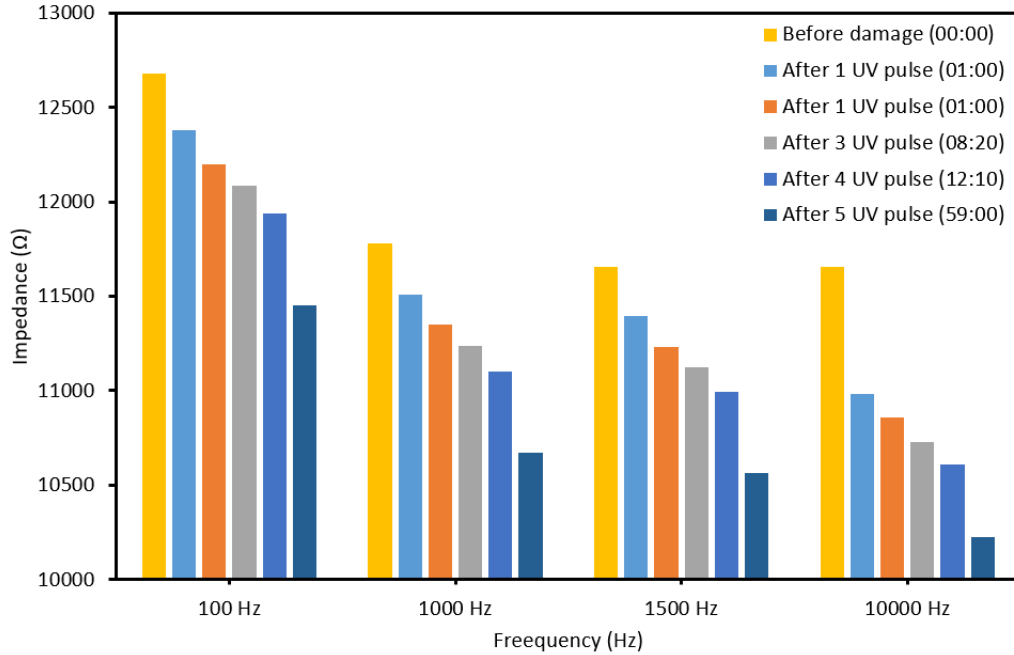


Figure 0.8 The change in impedance of a single electrode upon damage exposure in 0.1, 1, 1.5 and 10 kHz frequency resulted by cell shrinkage and lift-off.

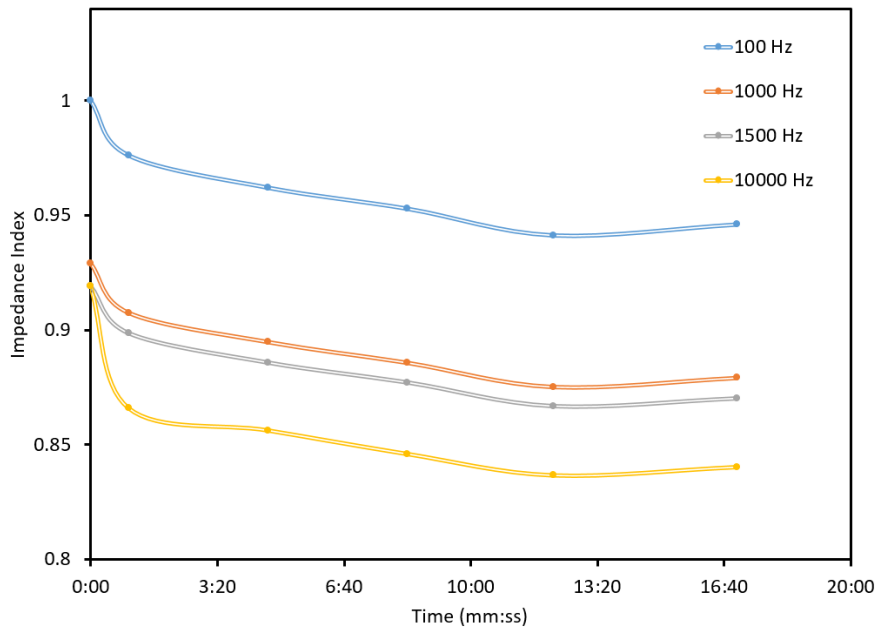
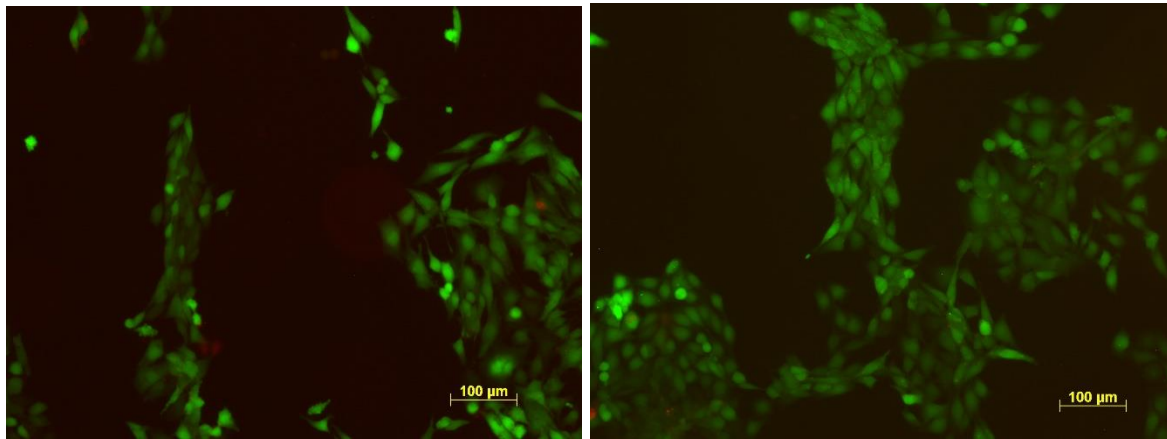


Figure 0.9 Minute-sensitive extra-cellular detection of neuronal cells through normalized impedance index.

## CHAPTER 6. FUTURE WORK: MACHINE LEARNING-GUIDED INKJET PRINTING OF HIGHLY CONDUCTIVE GRAPHENE PATTERNS

In order to advance the current findings, it is beneficial to improve the temporal sensitivity of the biochip from minute-accurate or even second-accurate level. Moreover, at this point, confluency and density of the cell network is calculated by capturing images before electrochemical data acquisition. This study can be a starting point for creation of a real-time object detection framework to provide a visual feedback for the electrochemical data acquisition platform. Figure 5.1 demonstrates the growth of the N27 cells in 2DIV (left) compared to 3DIV (Right). With the advancements of object detection and electrochemical frameworks, the current platform can enable second-sensitive measurements through the expansion of visual/optical sensing capabilities.



*Figure 0.1 Proliferation of N27 rat dopaminergic neuronal cells in (left) 2 days in vitro compared to (Right) 3 days in vitro.*

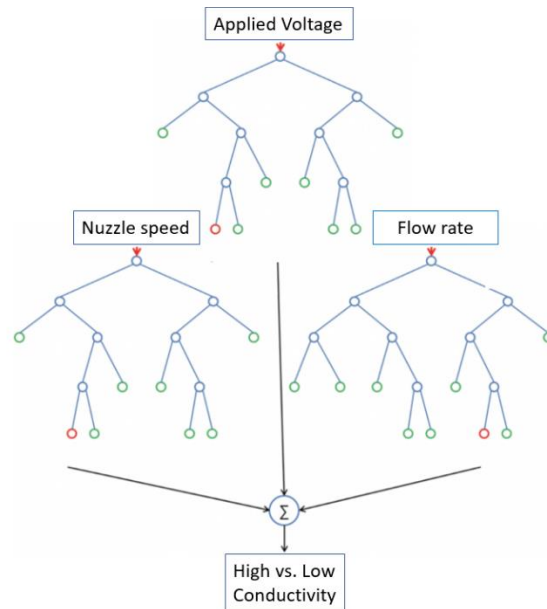
In order to improve the performance of the graphene electrodes prior to sensor fabrication, it is valuable to predict the conductivity of each graphene line right after the inkjet printing process. Therefore, the use of machine learning for distinguishing between printing parameters that are likely to result in low-conductivity prints and the parameters with higher importance, is investigated. To accomplish this goal, a large dataset was created from the conductivity of the printed lines along with the three major experimental parameters: Flow rate, electrostatic field intensity and nuzzle speed as demonstrated in Table 6.1.

Table 0.1 A sample subset of the created dataset.

<b>Nuzzle Speed (mm/min)</b>	<b>Flowrate (ul/min)</b>	<b>Applied voltage (kV)</b>	<b>Resistance (k<math>\Omega</math>)</b>
300	15	0	19.49
300	15	1	74.3
300	15	2	87.1
300	15	3	163.1
300	15	4	5.76

The role of the machine learning model is to take the above printing parameters as input and initially classify the quality of the resulting prints to two class of low and high conductivities. The model was trained and tested on a dataset with a flow rates ranging from 3 to 15  $\mu$ l in 3 $\mu$ l intervals, Nuzzle speeds ranging from 300 to 700 mm/min in 200 mm/min intervals

and applied voltages ranging from 0 to 5 kV in 1 kV intervals. Linear regression was chosen as the benchmark model for quality prediction which was expectedly shown to be impractical due to non-linearity of the fluid dynamic of the inkjet printing process. Therefore, two other classic learning algorithms, Random Forest and Adaboost, were employed which both can be categorized as ensemble learning models based on decision trees as demonstrated in Figure 6.2.



*Figure 0.2 A schematic representation of an ensemble learning model for predicting the quality of inkjet-printed graphene patterns based on experimental parameters.*

The models were initially trained on 105 data points (including non-functioning prints), with a 3-1 split for train-test dataset. Due to small size of the dataset we expect to observe extreme over-fitting behavior. Thus, the accuracy are the models are reported after 5-fold cross validation given in Figure 6.3, with the error bars representing the standard deviation after 5 repetitions.

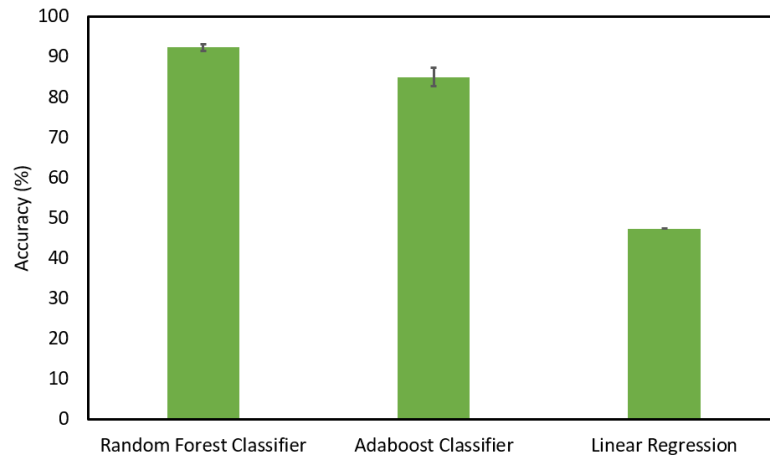


*Figure 0.3 Performance of Random Forest, Adaboost and Linear regression Models for Conductivity prediction on test dataset (n=11).*

Consequently, the models were employed for identifying the feature importance in the inkjet printing process. As Figure 6.4 depicts Flow rate was shown to be the main player in defining the resultant conductivity.

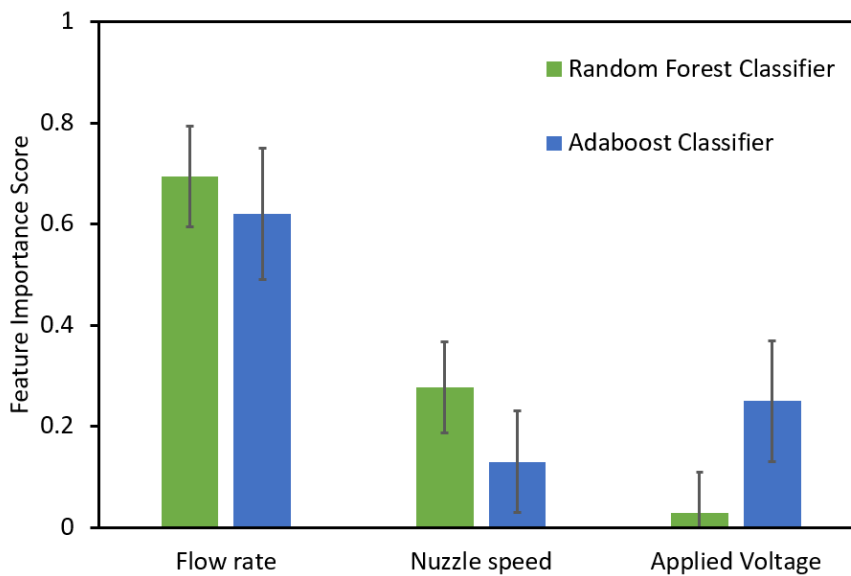


*Figure 0.4 Feature importance assessment by Random Forest and Adaboost classifiers for conductivity prediction of inkjet-printed graphene patterns.*

This will suggest the applicability of machine learning algorithms to determine the required experimental properties for creation of high-quality graphene patterns. Moreover, the

biosensor fabrication process typically entails various steps. Therefore, conductivity estimation right after patterning and thermal treatment is valuable to enhance the electrode performance conductivity at the end point, without the need for redundant trials. At the end of this thesis work, I can see broader applications of the as-prepared sensory system on real-time detection of neuronal damage. The N27 rat dopaminergic neuronal cell network that was used in this work, is the model cell line for the study of Parkinson's disease, and finding the cause of cell death suffering this disease and other neurodegenerative disorders imparts vital information. Therefore here we took one step further, to bring a broader understanding of micro-scale interactions of cell network in the underlying stages prior to their death.